University of Nottingham

UK | CHINA | MALAYSIA

Development and Improvement of the MoS_6 Cathode Material for Rechargeable All-Solid-State Lithium Batteries

Mingyuan Chang, BSc, MEng

Thesis submitted to the University of Nottingham

for the degree of Doctor of Philosophy

September, 2024

Abstract

All-solid-state lithium batteries without any liquid organic electrolytes can realize high energy density while eliminating flammability issues. The sulfide solid electrolytes with high ionic conductivity and attractive mechanical feature of plastic deformation, become the most promising solid electrolyte. Moreover, active materials such as transition metal sulfides with high specific capacity are essential to the realization of good electrochemical performance. However, the limited reversible specific capacity and large volume change of the sulfide cathodes upon cycling still hinder their application in the all-solid-state lithium batteries using sulfide electrolytes. Constructing electronic/ionic conductive networks in the cathode and realizing intimate interfacial contact at the electrolyte/cathode interface are prominent strategies to address the above issues.

Herein, MoS_6 is employed as the active material of the sulfide cathode, owing to its high specific capacity enabled by the multi-electron reactions of $S_2^{2-} + 2e^- \rightarrow 2S^{2-}$ proceeding during the charge-discharge process. Consequently, MoS_6 with high S_2^{2-} content possesses an ultra-high theoretical specific capacity of 1117 mAh g^{-1}, showing potential applications in constructing high energy

all-solid-state battery. Furthermore, two modified composites are designed, with aims of achieving high and stable reversible specific capacity for long-term cycling. By coating a thin layer of $Li_7P_3S_{11}$ solid sulfide electrolyte on the MoS_6 particles, the $Li/Li_6PS_5Cl/MoS_6@15\%Li_7P_3S_{11}$ all-solid-state lithium batteries show a high initial discharge capacity of 1083.8 mAh g^{-1} at 0.1 A g^{-1} and long cycle life of 1000 cycles under 1A g^{-1} at 25 °C. Furthermore, through ball milling of MoS_6 and LiI, the as-obtained $95MoS_6{\cdot}5LiI$ cathode exhibit a high initial capacity of 1016.3 mAh g^{-1} at 0.1 A g^{-1} within 1.0–3.0 V and capacity retention of 301.1 mAh g^{-1} at 1 A g^{-1} after 500 cycles.

This thesis provides a material preparation guidance of alternative cathodes of MoS_6 and its derivates such as $MoS_6@15\%Li_7P_3S_{11}$ and $95MoS_6{\cdot}5LiI$, with noticeable electrochemical performances, including high reversible capacity, long-term cycling stability, and good compatibility for all-solid-state lithium rechargeable batteries.

Achievements

Journal papers

1. **Mingyuan Chang**, Mengli Yang, Wenrui Xie, Fuli Tian, Gaozhan Liu, Ping Cui, Tao Wu*, Xiayin Yao*. Micro-sized MoS_6@ 15% $Li_7P_3S_{11}$ composite enables stable all-solid-state battery with high capacity. Batteries, **2023**, 9(11): 560.
2. **Mingyuan Chang**, Junjie Jia, Gaozhan Liu, Jianwen Zhang, Na Wang, Yangyang Zhou, Ping Cui, Tao Wu*, Xiayin Yao*. LiI doped MoS_6 composite for room temperature all-solid-state lithium batteries. Chemical Communications. (Accepted)
3. Fuli Tian, **Mingyuan Chang**, Mengli Yang, Wenrui Xie, Shaojie Chen*, Xiayin Yao*. Multi-electron reaction based molybdenum pentasulfide towards high-energy density all-solid-state lithium batteries. Chemical Engineering Journal, **2023**, 472: 144914.
4. Wenrui Xie, **Mingyuan Chang**, Wentong Fan, Mengli Yang, Fuli Tian, Xiaolin Xue, Xiaolei Zhao, Hao He*, Xiayin Yao*. An amorphous niobium polysulfide based nanocomposite enables ultrastable all-solid-state lithium batteries[J]. Materials Chemistry Frontiers, **2023**, 7: 2844–2850.
5. Na Wang, **Mingyuan Chang**, Wenrui Xie, Gaozhan Liu, Lu Zhang, Hao He*, Xiayin Yao*, Niobium sulfide nanocomposite as cathode materials for all-solid-state lithium batteries with

enhanced electrochemical performances, Nanoscale, 2024, 16(18):8915–8921.

6. Mengli Yang, Yu Yao, **Mingyuan Chang**, Fuli Tian, Wenrui Xie, Xiaolei Zhao, Yan Yu*, Xiayin Yao*. High energy density sulfur-rich MoS_6-based nanocomposite for room temperature all-solid-state lithium metal batteries. Advanced Energy Materials, **2023**, 13(28): 2300962.
7. Ruru Meng, Jinghua Wu, Mengting Zhu, **Mingyuan Chang**, Nini Zhang, Panlei Cao, Fuli Tian, Xiayin Yao*, A two-dimensional MoS_2 NS@$Li_7P_3S_{11}$ composite cathode for all-solid-state lithium batteries, ACS Applied Energy Materials, **2024,** 7(10), 4603–4608.
8. Xinshuang Chang, Gaozhan Liu, Ming Wu, **Mingyuan Chang**, Xiaolei Zhao, George Z. Chen, Kam Loon Fow*, Xiayin Yao*. Dual-functional ZnO/LiF layer protected lithium metal for stable $Li_{10}GeP_2S_{12}$-based all-solid-state lithium batteries. Battery Energy, **2023**, 2(3): 20220051.
9. Shujiao Yang, Zhihua Zhang, Lin Shen, Peng Chen, Zhi Gu, **Mingyuan Chang**, Yue Zhao, Hao He*, Xiayin Yao*, Gravity-driven poly(ethylene glycol)@$Li_{1.5}Al_{0.5}Ge_{1.5}(PO_4)_3$ asymmetric solid polymer electrolytes for all-solid-state lithium batteries, Journal of Power Sources, **2022**, 518:230756.

Patents

1. Xiayin Yao, **Mingyuan Chang**, Gaozhan Liu. Multi-sulfide materials preparing methods and relevant solid-state rechargeable battery. Chinese patent pending No.: 202210223722.8
2. Xiayin Yao, **Mingyuan Chang**, Gaozhan Liu. LiI/multi-sulfide materials preparing methods and relevant solid-state rechargeable battery. Chinese patent No.: 202210223710.5
3. Xiayin Yao, **Mingyuan Chang**, Gaozhan Liu. Solid-state electrolyte coated multi-sulfide materials preparing methods and relevant solid-state rechargeable battery. Chinese patent No.: 202210027315.X

Acknowledgements

As I stand at the culmination of this long and intellectually stimulating doctoral journey, I am overwhelmed with a sense of deep gratitude towards everyone who has been part of this expedition. This acknowledgment is a sincere effort to express my heartfelt thanks to all those who have been instrumental in supporting and guiding me through this rigorous academic endeavor.

First of all, I would like to thank my off-campus advisor, Dr. Xiayin Yao, who gave me this opportunity to focus on my research work, his guidance and suggestion help me to get my PhD degree. I am grateful for the numerous hours we spent discussing my research ideas, brainstorming solutions, and dissecting complex concepts. His immense knowledge and expertise have provided me a solid foundation which let me built my own academic pursuits. Meanwhile I would like to thank my advisor Dr. Tao Wu and Dr. Ping Cui for their patient and invaluable advices. Their knowledge, meticulous attention, and boundless enthusiasm have illuminated my path, fostering a deeper understanding and a genuine passion for my study.

I also would like to thank my colleagues for their support and assistance on my research work. For every staff of CNITECH testing center, I express my gratitude. They provided a lot of convenience for my analysis work.

Most importantly, I am very grateful to my parents, Mr. Jun Chang and Mrs. Shirong Liu for your continuous support in my work and life. I will attempt to articulate the depths of my appreciation for your unconditional love, support, and profound sacrifices. Throughout my life's journey, you have been the compass that steered me through rough seas, the beacon that lit my path in the darkest hours, and the anchor that kept me grounded amidst life's storms. During periods of intense pressure and fatigue, your understanding, patience, and inspiring words were my pillars of resilience. You taught me the importance of perseverance, discipline, and integrity – virtues that have been integral to my academic growth and professional development. I cannot carry on this difficult journey without your love and patient. You always encourage me, help me and understand me. you are the best mother and father in the world.

Finally, my sincere appreciation extends to my grandfather, an outstanding engineer, Mr. Shucheng Chang. Your unconditional support, love, and guidance have been instrumental in my journey towards achieving this significant milestone in my life. Your wisdom, encouragement, and the strength of your character have continuously inspired me to push the boundaries of knowledge and strive for excellence. From my childhood until the master study period, your belief in my abilities has never wavered. I am grateful for the

numerous years we spent together. Your insightful suggestions and critical thinking skills have helped me to handle various problems. Your patience, understanding, and love have been my anchor during moments of stress and self-doubt. You gave me a loving and confident childhood, this love transited to my brave heart to deal with all kinds of issues. I will always miss you and hope you can proud of me, even though you have been away from me for six years, your spirit will accompany me through my whole life.

There will be ups and downs in the future, but I would like to quote the speech content of my favorite singer: you will inevitably misspeak, trust the wrong person, underreact, overreact, hurt the people who did not deserve it, overthink, not think at all, self-sabotage, ruined perfectly good moments for yourself and others, deny any wrong doing, not take the steps to make it right, feel very guilty, let the guilt eat you, hit rock bottom, finally address the pain you caused, try to do better next time, rinse, repeat. These mistakes will cause you to lose things. I am trying to tell you, that losing things does not just mean losing. A lot of time when we lose things, we gain things too. And I know it is hard to know which path to take. There will be times in life where you need to stand up for yourself. Times when the right thing is actually to backdown and apologize. Times when the right thing is to fight. Times when the right thing is to turn

and run. Times to hold on with all you have. Times to let go with grace. Sometimes the right thing to do is to throw out the old school of thoughts. Sometimes the right thing to do is sit and listen to the wisdom of those who have come before us. We will learn from it. We will grow more resilient because of it. As long as we are fortunate enough to be breathing, we will breathe in, breath through, breath deep, and breath out.

Table of Contents

List of Figures

Figure 5-10 Galvanostatic discharge/charge profiles of (a) MoS_6 and (b) MoS_6@15%$Li_7P_3S_{11}$ composite cathodes at 0.1 A g^{-1}.

Figure 5-11 Cyclic performances of Li/Li_6PS_5Cl/MoS_6 and Li/Li_6PS_5Cl/MoS_6@15%$Li_7P_3S_{11}$ all-solid-state batteries under 0.1 A g^{-1}.

Figure 5-12 Cyclic performances of MoS_6@10%$Li_7P_3S_{11}$, MoS_6@15%$Li_7P_3S_{11}$ and MoS_6@20%$Li_7P_3S_{11}$ cathodes under 0.1 A g^{-1}.

Figure 5-13 Nyquist plots and the equivalent circuit diagram of MoS_6 and MoS_6@15%$Li_7P_3S_{11}$ composite cathodes over range of 1.0-3.0 V at 0.1 A g^{-1}after 1st and 20th cycles.

Figure 5-14 Rate performances of MoS_6 and MoS_6@15%$Li_7P_3S_{11}$ composite under different current densities.

Figure 5-15 Ragone plot deduced from the rate performances in Figure 5-14.

Figure 5-16 (a) Long-term cyclic performance of MoS_6@15%$Li_7P_3S_{11}$ composite under 1 A g^{-1}. (b) The EDS mapping of MoS_6@15%$Li_7P_3S_{11}$ composite after 1000 cycles.

Figure 5-17 CV curves at different scan rates of (a) MoS_6@15%$Li_7P_3S_{11}$ composite and (c) MoS_6. The log (peak current) *vs.* log (scan rate) fitted plots at reduction and oxidation peaks of (b) MoS_6@15%$Li_7P_3S_{11}$ composite and (d) MoS_6.

and $95MoS_6 \cdot 5LiI$ composite under 0.1 A g^{-1}.

Figure 6-12 Rate performances of MoS_6 and $95MoS_6 \cdot 5LiI$ composite under different current densities.

Figure 6-13 Ragone plot deduced from the rate performances in Figure 6-12.

Figure 6-14 Long-term cyclic performance of MoS_6 and $95MoS_6 \cdot 5LiI$ composite under 1 A g^{-1}.

Figure 6-15 Nyquist plots and the equivalent circuit diagram of MoS_6 and $95MoS_6 \cdot 5LiI$ composite cathodes after 1^{st} and 500^{th} cycles at 1 A g^{-1} within1.0–3.0 V.

Figure 6-16 CV curves of (a) $95MoS_6 \cdot 5LiI$ composite and (c) MoS_6 with various scan rates. The log (peak current) *vs.* log (scan rate) simulation plots at reduction and oxidation peaks of (b) $95MoS_6 \cdot 5LiI$ and (d) MoS_6.

Figure 6-17 (a) Measured diffusivities plot of $Li/Li_6PS_5Cl/95MoS_6 \cdot 5LiI$ and $Li/Li_6PS_5Cl/MoS_6$ all-solid-state lithium batteries. The plot is derived from GITT measurements. (b) GITT plot of $Li/Li_6PS_5Cl/95MoS_6 \cdot 5LiI$ and $Li/Li_6PS_5Cl/MoS_6$ all-solid-state lithium batteries.

List of Tables

List of Abbreviations

AB	Acetylene black
ALD	Atomic layer deposition
C	Charge rate
CFS	C-FeS_2-S composite
CMK-3	Ordered mesoporous carbon
CPE	Constant phase angle element
CV	Cyclic Voltammetry
DF-MD	Density functional-molecular dynamics
DFT	Density functional theory
EDS	Energy-dispersive X-ray spectroscopy
EIS	Electrochemical impedance spectroscopy
ESM	Eggshell membrance
FIB	Focused ion beam
GITT	Galvanostatic intermittent titration technique
HRTEM	High Resolution Transmission Electron Microscope
ICP-OES	Inductively coupled plasma optical emission spectrometer
LATP	$Li_{1.3}Al_{0.3}Ti_{1.7}(PO_4)_3$
LGPS	$Li_{10}GeP_2S_{12}$
LIB	Lithium-ion batteries
LNMO	$LiNi_{0.5}Mn_{1.5}O_4$

LPOS	$75Li_2S \cdot 24P_2S_5 \cdot 1P_2O_5$
LPS	Li_3PS_4
LTO	$Li_4Ti_5O_{12}$
MWCNT	Multi-walled carbon nanotubes
NCA	Ni-Co-Al composite
NHE	Normal hydrogen electrode
NS	Nanosheets
PAN	Polyacrylonitrile
PEO	Polyethylene oxide
PH	Pondus hydrogenii
PLD	Pulsed laser deposition
PMMA	Polymethyl methacrylate
PPO	Polyphenylene ethe
PVDC	Polyvinylidene chloride
PVDF	Polyvinylidene difluoride
PVP	Polyvinyl pyrrolidone
rGO	Reduced graphene oxide
SE	Solid electrolyte
SEI	Solid electrolyte interphase
SEM	Scanning electron microscope
SLMP	Synthesized lithium metal powder
TBAOH	Tetrabutylammonium hydroxide

XPS	X-ray photoelectron spectroscopy
XRD	X-ray diffraction
2D	Two dimension

List of Symbols

°C	Degree Celsius
wt.%	Weight percentage
Å	Angstrom
nm	Nanometer
µm	Micron
mm	Millimeter
cm	Centimeter
µg	Microgram
mg	Milligram
g	Gram
kg	Kilogram
min	Minute
h	Hour
W	Watt
kW	Kilowatt
m^2	Square meter
m^3	Cubic meter
ml	Milliliter
L	Liter
mol	Mole
V	Volt

kV	Kilovolt
eV	Electron volt
S cm^{-1}	Siemens per centimeter
μA cm^{-2}	Microampere per square meter
mA cm^{-2}	Milliampere per square meter
mAh g^{-1}	Milliampere hour per gram
Wh kg^{-1}	Watt hour per kilogram
W kg^{-1}	Watt per kilogram
Wh L^{-1}	Watt hour per liter
mA g^{-1}	Milliampere per gram
A g^{-1}	Ampere per gram
mg cm^{-2}	Milligram per square meter
mAh cm^{-3}	Milliampere hour per cubic meter
cm^3 mol^{-1}	Cubic meter per mole
rpm	Revolutions per minute
Mpa	Megapascal
cm^{-1}	Per centimeter
Ω	Ohm
Hz	Hertz
MHz	Millionhertz
R_e	Resistance of the electrolyte
R_{ct}	Interfacial charge transfer resistance

Z_w	Warburg resistance
i	Peak current
τ	Time duration of the pulse
n_m	Molar mass of the active material
v_m	Volume of the active material
S	Cell interfacial area
ΔE_s	Voltage drops of the pulse
ΔE_t	Voltage drops of discharge process
v	Scan rate
D	Diffusion

Chapter 1. Introduction

1.1 Research background

Lithium-ion batteries are used in many fields such as consumer electronic devices, electronic vehicle and other energy storage equipment. Using renewable energy sources to replace traditional sources can protect environment effectively due to the reduced consumption of fossil fuels. In 1799, Alessandro Volta realized the first demonstration of electrochemical device, Vlotaic Pile, and ~200 years later, the first commercial lithium-ion battery (LIB) was successfully launched by Sony Corporation, opening up the electrification period by the widespread uses of electrochemical energy storage devices with great impacts in economy and ecology. Consequently, the three founders of LIBs, John. B. Goodenough, M. Stanly Whittingham and Akira Yoshino won the Nobel Prize in Chemistry in 2019[1].

A LIB consists of anode materials, cathode materials, liquid electrolytes and separators[2]. Typically, in the system of LIBs, $LiNi_xCo_yMn_{1-x-y}O_2$ or $LiFePO_4$ are employed as the cathode materials, graphite is used as the anode material, and organic liquid electrolyte consisting of Li salt and solvents is infused into the polymer-based separator between the cathode and anode. During the

charge progress, lithium ions are extracted from the cathode materials, pass through the electrolyte, and intercalate into the graphite anode. The separator not only ensures the Li^+ transport, but also prevents the crossover of electrons that causes short circuit of the cell. During the discharge progress, the electrochemical reactions and transportations proceed inversely[3-6].

LIBs are the most employed devices in electrochemical energy storage fields, including portable electronic devices, electric vehicles, energy storage station, etc. They provide significant benefits in ecology, such as reducing air pollution and contributing to a cleaner environment, increasing efficiency of solar, wind, and other clean energy conversion into electrical energy, and alleviating the dependence of human's society on the fuel resources. However, the large-scale applications of LIBs are still challenged, owing to performance and safety concern. The risk of leakage, short-circuiting and even fire in extreme conditions are still frequent in electric vehicle because of the liquid electrolyte of lithium ion batteries. Finally, the energy density and capacity fading of the conventional LIBs are still below the desired levels of electrical vehicles.

To address the limitation issue of LIBs, a large number of researches are investigated. Due to the limited lithium ions diffusion coefficient, lithium ions often precipitated on the graphite anode

surface instead of inner intercalation, resulting in metallic Li deposition. Normally, metallic Li plating exhibits dendrite-like shape, and can pierce the separator, resulting in short circuit, finally caused thermal run away. The Li plating mainly occurs in conditions of low temperature and high charge rate. The low temperature would lead to a low diffusion coefficient, while high charge rate imposes a large Li^+ flux, all these issues can cause unmatched transport/reaction kinetics at the electrode/electrolyte interface, which is the origin of dendrite growth.

Compared with liquid lithium batteries, all-solid-state lithium batteries are expected to revolutionize the electric vehicle industry with their superior energy density and safety characteristics. Solid-state lithium batteries have potential to significantly increase the driving range of electric vehicles due to their high energy density based on the enlarged working voltage window. In addition, compared with liquid electrolyte used in traditional lithium-ion batteries, the solid state electrolyte can eliminate the risk of electrolyte leakage and reduce the thermal runaway probability, hence making the solid-state batteries become a safer option for electric vehicles. Among all solid-state electrolytes, sulfide-based electrolytes have broad application potential because of their high ionic conductivity and lower elastic modulus. Meanwhile, sulfide

electrolytes show superior compatibility with high-capacity transition metal sulfide cathodes due to the similar chemical potential, thus leading to higher energy density of the battery. However, all-solid-state lithium batteries with sulfide electrolyte and transition metal sulfide cathode still confront challenges of undesirable ionic transport kinetics and inferior interface contact within cathode layer. Furthermore, the specific capacity of transition metal sulfide cathode needs to be further improved to pursuit the increasing requirements of energy density.

1.2 Objectives and approaches

The all-solid-state lithium batteries studied in this thesis consist of lithium metal anode, sulfide solid electrolyte, and transition metal polysulfide. The main objective of this thesis is to design cathode material for all-solid-state lithium batteries with high theoretical capacity, intimate contact within cathode layer and good cyclic stability. Based on this context, three parts have been implemented:

(1) Selection of polysulfide cathode materials with excellent electrochemical performance, with following investigations:

a. Literature reviewing.

b. MoS_6 material synthesis.

c. Evaluating of electrochemical performance.

d. Mechanism analysis.

(2) Enhancement of MoS_6 by coupling with $Li_7P_3S_{11}$, which could improve the intimate contact between the cathode and electrolyte, so as to reach a high reversible capacity of the battery, with following investigations:

a. MoS_6@15%$Li_7P_3S_{11}$ composite synthesis.

b. Evaluating of electrochemical performance.

c. Mechanism analysis.

(3) Improvement of MoS_6 by ball milling with LiI, with aims of improving the lithium ion coefficient during the charge-discharge process, resulting in a long cycle life of the battery:

a. 95MoS_6·5LiI composite synthesis.

b. Evaluating of electrochemical performance.

c. Mechanism analysis.

These approaches will be divided into three works, which could correspond to two published papers. Every work will achieve at least one objective.

Thesis structure

Chapter 1 is the introduction part. It includes research background, objectives and approaches, and thesis structure.

Chapter 2 focuses on the literature review. It introduces cathode, anode, and solid state electrolyte materials reported in recent

literatures. This review gives reasons for the cathode materials selection and the designing of all-solid-state batteries.

Chapter 3 lists the methods of sample synthesis and characterizations in this thesis. It presents the detailed preparation methods of MoS_6, MoS_6@15%$Li_7P_3S_{11}$, 95MoS_6·5LiI and the fabrication of related batteries. Furthermore, the principles of various characterization techniques are introduced.

Chapter 4 studies the morphology and electrochemical performances of MoS_6, and the analysis of working principle of the investigated cathode materials during the initial charge-discharge process. This chapter provides a theoretical basis for further improvement in electrochemical performance of the MoS_6 materials in the following two chapters.

Chapter 5 studies the morphology and electrochemical performances of MoS_6@15%$Li_7P_3S_{11}$. By coupling with $Li_7P_3S_{11}$ sulfide electrolyte thin layer, the intimate contact between the cathode layer and electrolyte leads to a fast ionic transport kinetic, resulting in a high reversible specific capacity and stable cycle life.

Chapter 6 studies the morphology and electrochemical performances of 95MoS_6·5LiI. By doping LiI into the MoS_6 lattice via ball milling, the lithium ion diffusion coefficient is improved, resulting in fast electrochemical reaction kinetics. As a result,

$95MoS_6$·5LiI realizes a high reversible specific capacity and long cycle life.

Chapter 7 concludes the findings of MoS_6, MoS_6@15%$Li_7P_3S_{11}$ and $95MoS_6$·5LiI in the project.

Chapter 8 gives a perspective based on the achievements of this project. It mainly introduces the present situation of transit metal sulfides based all-solid-state batteries and some possible directions for future study.

The relevant flow chart is shown in Figure1-1, which displays the technical route of the whole doctoral research project. This thesis provides promising cathode materials, MoS_6, MoS_6@15%$Li_7P_3S_{11}$ and $95MoS_6$·5LiI, with high theoretical specific capacity, good compatibility with solid-state electrolytes, as well as prominent electrochemical reaction kinetics for all-solid-state lithium rechargeable batteries.

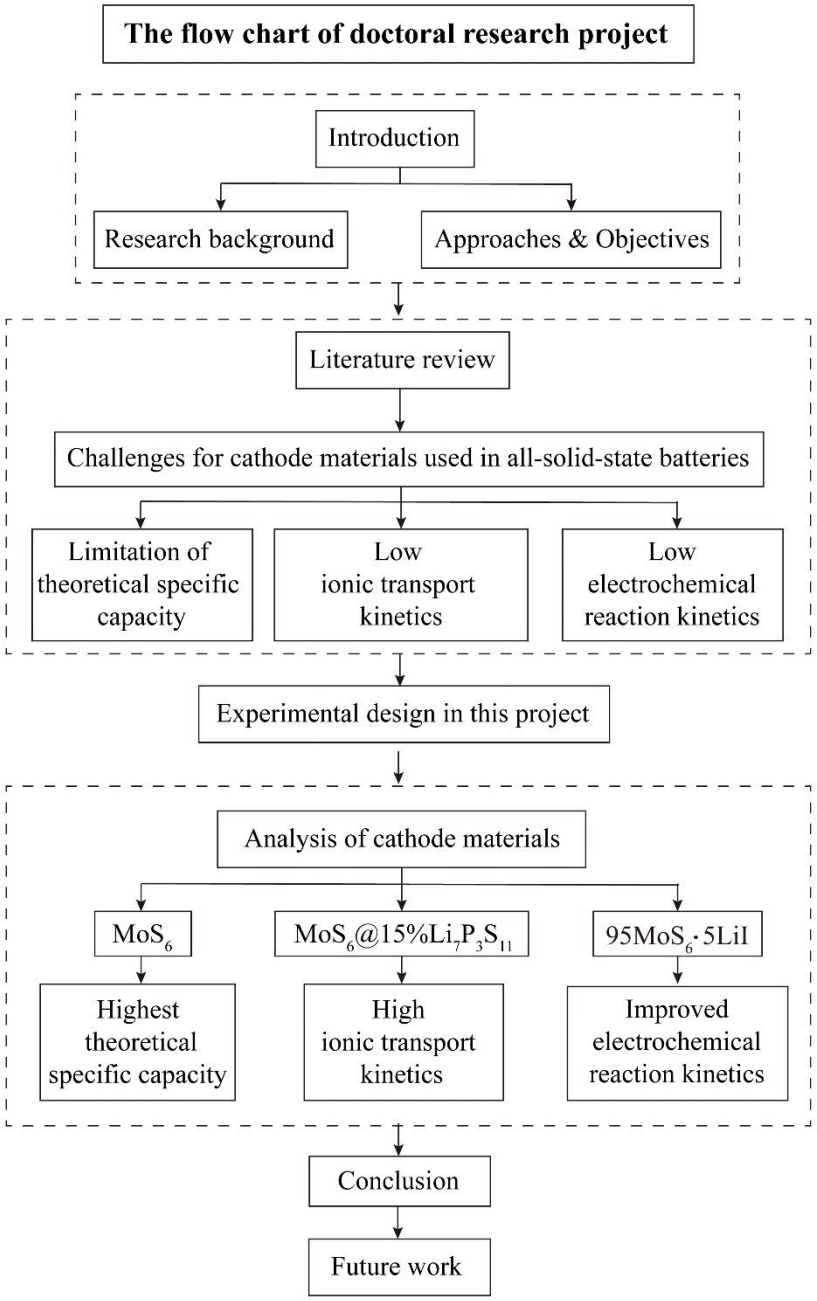

Figure 1-1 The flow chart of doctoral research project.

Chapter 2. Literature Review

2.1. Introduction

Energy storage is an essential issue for the sustainable development of human society. On the one hand, energy storage systems ensure the availability of power in occasional situation of shortage of primary energy source. Besides, energy storage systems can provide backup power in the event of grid failures or natural disasters, ensuring basic operation of critical services and infrastructure. From the perspective of economics, energy storage can lower energy costs by reducing the need for traditional power plant and allowing efficiently using of the electric grids. It also creates new economic opportunities through the development of new technologies and industries[7-10]. The overexploitation and utilization of non-renewable fossil fuels such as coal, petroleum and natural gas not only cause serious depletion of natural resources, but also has a huge impact on the environment and climate. In order to pursue the sustainable development of human society, energy structure optimization, clean energy development, energy transition efficiency improvement and energy storage technology innovation become global problems[11-15]. At present, the development of clean energy mainly focuses on hydro, solar, wind, geothermal, tidal,

and nuclear energy. However, these energy sources feature discontinuity and instability[16-19], and it is crucial to develop high-efficient energy storage devices to store these renewable energy for scheduled application.

Electrochemical power source, which can convert chemical energy into electrical energy, is widely used in various fields such as civil and military industries due to the portability and reliability[20-23]. According to the nature of uses, the electrochemical power source can be divided into three categories: primary batteries, secondary batteries and fuel cells.

As an important member of the secondary batteries (Figure 2-1), lithium-ion batteries have been utilized broadly in the field of plug-in hybrid/electric vehicles, smartphones, laptop computers and other portable electronic devices for the last decades, significantly reducing the environmental pollution and greenhouse gas emissions. The energy density of lithium-ion batteries is close to their limitation because of the low theoretical capacity of oxide cathodes (*i.e.* $LiFePO_4$, $LiCoO_2$, and $LiNi_xMn_yCo_zO_2$)[24-27] and graphite anode materials[28]. Lithium-sulfur batteries using lithium metal anode instead of graphite can realize high theoretical specific capacity value[29]. However, the organic liquid electrolyte based lithium-sulfur batteries have safety concerns such as leakage and explosion,

as well as poor rate capability and cycling stability due to the huge volume change of sulfur during the charge/discharge process. All-solid-state lithium batteries with nonflammable inorganic solid-state-electrolyte have attracted much attention in the field of energy storage[30-32].

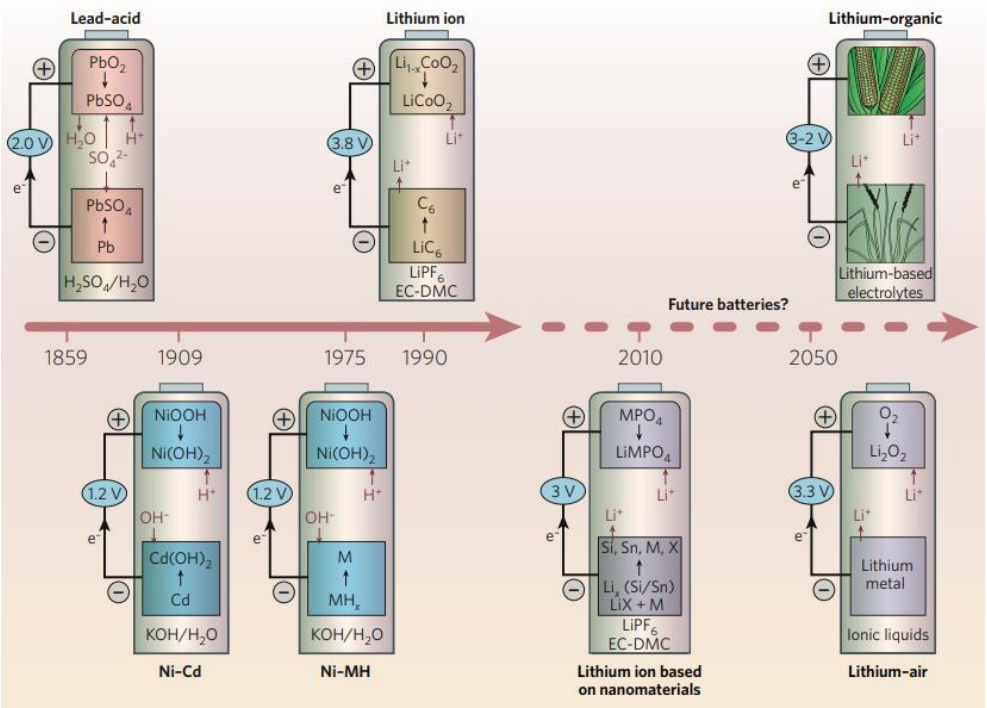

Figure 2-1 Chemistry of various batteries[1]

All-solid-state lithium batteries are mainly composed of three components: positive electrode, solid electrolyte and negative electrode. The working mechanism of all-solid-state lithium batteries are similar with lithium-ion batteries. During the charge process, lithium ions are de-intercalated from the active material of cathode and migrate to the anode through the solid electrolyte, while electrons flow from the positive electrode to the negative electrode

through the external circuit, finally lithium ions and electrons reencounter at the negative electrode, where alloying or intercalation reactions would occur[33-37]. These processes are inversed during discharge of the battery. In solid electrolytes, lithium ions migrate or diffuse through lithium ions transport channels, defects, or polymer segments in the crystal structure. The solid electrolyte can transport lithium ions while impeding electron transfers, the schematic illustration of all-solid-state lithium battery is shown in Figure 2-2, where the green, blue and grey balls present the lithium, active materials and solid electrolyte, respectively[38].

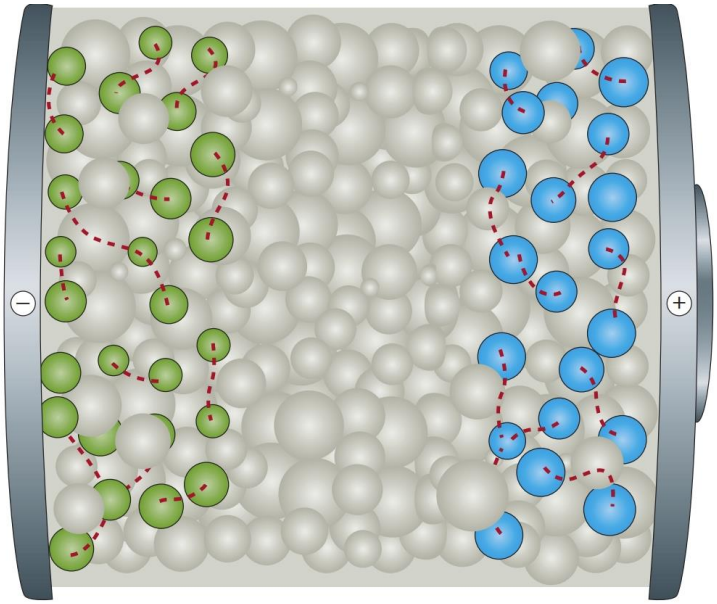

Figure 2-2 The structure of all-solid-state lithium battery[38].

2.2. Electrode and electrolyte materials

2.2.1. All solid state electrolyte materials

Solid electrolyte, also known as fast ionic conductor or superionic conductor, is the core component of all-solid-state lithium battery for achieving high safety, high energy density and long cycle life. These materials typically possess high ionic conductivity (10^{-1}–10^{-4} S cm^{-1}), low conductivity activation energy (< 0.5 eV) and high ion mobility number (t_{Li+}≈1) within a certain temperature range[37, 39-41]. Thus, the solid electrolyte is both a fast-ion conductor and an electronic insulator. Using solid electrolytes instead of flammable organic electrolytes and separators can completely eliminate the risks of leakage, combustion, and explosion associated with conventional lithium-ion batteries[42-50]. In addition, the all-solid-state battery can employ lithium metal as anode, which not only increases the operating voltage of the battery, but also provides higher specific capacity than that of graphite for achieving higher energy density of all-solid-state lithium batteries[51-58]. According to the different chemical composition, solid electrolytes are mainly divided into two categories: polymer and inorganic solid electrolytes. Polymer electrolyte based batteries have the advantages of high flexibility, viscoelasticity, and film-forming ability[59-62]. However, due to the

limited operating temperature range, low conductivity at room temperature, narrow electrochemical window, as well as poor mechanical strength, further works are still needed for improving the performance of polymer electrolyte based battery. Alternatively, inorganic solid electrolytes have broad application prospects in high-safety and large-capacity all-solid-state lithium batteries due to the high conductivity, high mechanical strength performances even at high temperature. The advantages and limitations of various solid electrolytes are shown in the Figure 2-3. The radar plots display the performances of oxide solid electrolytes, sulfide solid electrolytes, hydride solid electrolytes, halide solid electrolytes, thin-film electrolytes and polymer solid electrolytes[38].

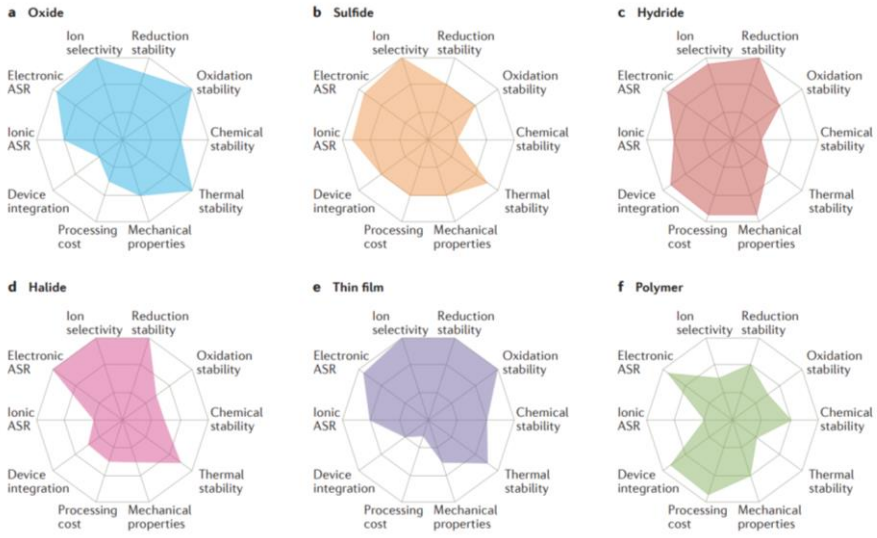

Figure 2-3 The advantages and limitations of different solid electrolytes[38].

2.2.1.1. Polymer solid electrolytes

Polymer solid electrolytes are composed of polymer matrices (polyamines, polyesters, and polyethers, among others) and lithium-based salts ($LiPF_6$, $LiClO_4$, and LiTFSI, etc.)[63-68], they exhibit a series of advantages such as light weight, easy film formation, outstanding viscoelasticity, and good processability[69, 70]. Polymer solid electrolytes mainly include polyvinyl oxide systems, polycarbonate systems, polysiloxane systems and single-ion conductor systems. The earliest polymer solid electrolyte is obtained by mixing PEO polymer matrix with lithium-based salts. In the amorphous matrix, the lithium ions are continuously complexed and dissociated with other lithium ions come from the ethylene oxide unit, resulting in the conduction of lithium ions through chain segment movement[59, 71-73]. Due to the high crystallinity of PEO at room temperature, the high ionic conductivity performance cannot be easily realized[74]. Some strategies such as blending, copolymerization, cross-linking, combing, grafting, hyperbranching and inorganic hybridization, can effectively reduce the crystallinity and transition temperature of the glass-phase in polymer matrix, resulting in improved kinetics of the chain segments and the dissociation of lithium salts, thereby increasing the ionic conductivity at room-temperature[75]. Furthermore, common

polymer matrices also include polyvinylidene fluoride (PVDF)[76], polypropylene oxide (PPO)[77], polymethyl methacrylate (PMMA)[78], polyacrylonitrile (PAN)[79] and polyvinylidene chloride (PVDC)[80], etc. Due to the low ionic conductivity at room temperature and the narrow operating temperature range, the practical application of the polymer electrolyte based solid-state batteries still confront challenges.

2.2.1.2. Inorganic solid electrolytes

Compared with polymer solid electrolytes, inorganic solid electrolytes possess numerous advantages like non-flammable property and wide operating temperature range. Some sulfide electrolytes can even achieve a similar ionic conductivity compared with that of liquid electrolyte at room temperature. The dense inorganic solid electrolyte can also impede the growth of lithium dendrites and prevent short circuit issue in the battery. Some electrolytes display high oxidation potential and stability when coupled with lithium metal. Finally, depending on the different requirements, various preparation methods are employed to synthesis the electrolytes, which can be molded into desired shape and size[81-87].

According to the crystallographic characteristics, inorganic

solid electrolytes could be divided into crystalline electrolytes, glass electrolytes and glass-ceramic electrolytes. Typically, crystalline solid electrolytes would be categorized in NASICON type[88], thio-LISICON type[89], Garnet type[90], (trans) perovskite type[91], and Li_3N type[92]. Glass type solid electrolytes normally include LiPON electrolytes and glass type sulfide electrolytes. Glass-ceramic solid electrolytes mainly composed of NASICON type and electrolytes of Li_2S-P_2S_5[93-99]. Inorganic solid electrolytes can be roughly divided into two categories of oxide solid electrolyte and sulfide solid electrolyte. Among them, NASICON, LISICON, Garnet, (trans)perovskite and LiPIN belong to oxide solid electrolytes, while sulfide solid electrolytes include thio-LISICON and Li_2S-P_2S_5 electrolytes[100, 101].

Oxide solid electrolytes possess high chemical stability and can be prepared in the air. Improving the ionic conductivity and interfacial compatibility at room temperature are the main challenges for all-solid-state batteries using oxide solid electrolytes. At present, some strategies like homovalent elements substitution to adjust the ion transport channel, doping heterovalent elements to increase the concentration of carriers, and improving the preparation process to reduce the grain boundary are mainly proposed. Besides, coupling a polymer solid electrolyte layer or amorphous electrolyte thin film is

an effectively method to achieve dense interfacial contact, and improve the compatibility between oxide solid electrolyte and electrode material, especially the lithium metal anode.

Owing to the larger ionic radius and stronger polarization of S^{2-} compared with those of O^{2-}, the sulfide solid electrolytes exhibit more suitable crystal structure for lithium-ion transport. On the other hand, the non-bridging S weakens the binding effect of the lattice backbone for lithium ions and increases the concentration of transiting lithium ions. As a result, sulfide solid electrolytes achieve a higher ionic conductivity than that of oxide solid electrolytes at room temperature. The sulfide solid electrolyte also shows a series of mechanical advantages such as soft texture, the dense sheet can be easily obtained by cold pressing. Nevertheless, the sulfide electrolytes can easily react with moisture in the air[102], resulting in the invalidation of the electrolyte. The high cost of raw materials for sulfide electrolyte preparation would be considered as a problem either[38].

(1) Crystalline sulfide solid electrolyte

In 2001, the group from Tokyo Institute of Technology revealed that thio-LISICON crystalline solid electrolyte exist in Li_2S-P_2S_5-GeS_2 solid solution[103]. Depending on different components ratio, the chemical composition of $Li_{4-x}Ge_{1-x}P_xS_4$ can be divided into three

parts. In the range of 0.6<x<0.8, the $Li_{4-x}Ge_{1-x}P_xS_4$ reveal a high ionic conductivity at room temperature. For the condition of x=0.75, the ionic conductivity reaches the highest value of 2.2×10^{-3} S cm^{-1}. In 2011, The reaseatch group of Dr. Kanno synthesized a ternary $Li_{10}GeP_2S_{12}$ with three-dimensional lithium ion transport channels[104]. It possesses a high ion conductivity value of 1.2×10^{-2} S cm^{-1}, which is comparable with that of liquid organic electrolytes, and display a wide electrochemical window of 5 V. In 2016, they developed a new ternary sulfide solid electrolyte, $Li_{9.54}Si_{1.74}P_{1.44}S_{11.7}Cl_{0.3}$, with a ionic conductivity of 2.5×10^{-2} S cm^{-1}, which is two fold higher han that of $Li_{10}GeP_2S_{12}$ at room temperature[30].

(2) Glass type sulfide solid electrolytes

Compared with crystalline materials, glass-type materials illustrate advantages of long-range disorder, short-range ordering and isotropy, which can further expand the lithium-ion transport channel and improve the room-temperature ionic conductivity of glass type sulfide solid electrolytes. Glass type sulfides are typically composed of network formers (SiS_2, P_2S_5, B_2S_3, etc.) and network modifiers (Li_2S), mainly including Li_2S-SiS_2, Li_2S-P_2S_5, and Li_2S-B_2S_3[105-107]. Introducing bridging O into the binary sulfide solid electrolyte by adding small amount of lithium-containing oxide Li_xMO_y can

effectively weaken the binding energy of bridging S for lithium ions[108, 109]. The additives of lithium halides (LiI, LiBr) can also enhance the ionic conductivity of the electrolyte at room temperature[110-112]. Glass type sulfide solid electrolytes exhibit advantages of high ionic conductivity, wide electrochemical window, wide composition controllability and good thermal stability, showing great application potential in the field of high safety and high energy density all-solid-state batteries.

(3) Glass ceramic sulfide solid electrolyte

In 2003, Dr. Tatsumisago of Osaka Prefecturel University reported that partial glass ceramics sulfide solid electrolyte can be obtained by recrystallization of Li_2S-P_2S_5 glass electrolyte through high temperature treatment after ball milling. The conductivity of 80%Li_2S-20%P_2S_5 can reach the value of 7.2×10^{-4} S cm^{-1}, which is five times higher than that of the glass based electrolyte[113]. Owing to the crystalline phase transition of $Li_7P_3S_{11}$by annealing treatment, the ionic conductivity of 70%Li_2S-30%P_2S_5 glass-ceramic electrolyte is higher than that of glass based electrolyte at room temperature[114]. At the same time, the glass particle of solid electrolytes becomes soft during the annealing process, which can reduce the grain boundaries and reduce the resistance. In 2012, Dr. Boulineau from Université de Picardie Jules Verne synthesized a new

sulfide based solid electrolyte, Li_6PS_5X (X: Cl, Br, I)[115]. Li_6PS_5Cl was synthesized with a high ion conductivity of 1.33×10^{-3} S cm^{-1}. By substituting halogens for S^{2-} in the electrolyte, the disordering of the sites is taken place and increasing the vacancy concentration of lithium ions, finally promote the diffusion of Li ions. Despite the lower ion conductivity than that of $Li_{10}GeP_2S_{12}$, the Li_6PS_5Cl electrolyte possesses advantages such as facile preparation process and wide electrochemical window (~7V).

Depending on the different preparation strategies, the common preparation methods of sulfide solid electrolytes mainly include[37, 61, 116-121]:

a. Mechanical ball milling. Typically, various raw materials are physically mixed together, the obtained mixture would proceed the solid-phase reaction by mechanical ball milling to obtain an amorphous sulfide solid electrolyte precursor, followed by annealing process to obtain a glass ceramic sulfide electrolyte.

b. Wet chemical method. Different raw materials are added into the organic solvent with the stoichiometric ratio followed by stirring and heat treatment, receive the precursor containing solvent molecules. The as-prepared precursor powders can be converted into sulfide solid electrolyte after appropriate annealing treatment.

c. Solution method. The sulfide solid electrolyte is completely

dissolved in an organic solvent to form a homogeneous solution firstly, and then the precursor powders can be obtained after removing the solvent. The glass ceramic sulfide solid electrolyte is then obtained after appropriate annealing treatment[122].

In conclusion, when integrating solid electrolyte into the all-solid-state batteries, the following advantages could be achieved:

a. Wide electrochemical window. Solid electrolytes with wide electrochemical window can broaden the selection range of electrode materials and realize the application of high-voltage cathode materials.

b. High packaging efficiency. Because of the all solid raw materials property, it supports serial superposition and bipolar structure, simplifying the battery assembly process and facilitating rapid packaging.

c. Film flexibility. Flexible thin-film batteries can be fabricated through PLD technology, which has broad development prospects in the fields of smart wearables and implantable medical devices in the future.

d. High output voltage. By connecting the cells through multi-layer stacking technology, the battery system with high output voltages can be produced.

e. High temperature tolerance. Solid materials are structurally stable over a wide temperature range while eliminate the risk of volatilization and combustion at high temperatures. With the increasing of temperature, the conductivity of the solid electrolyte increases as well.

2.2.2. All-solid-state lithium battery electrode materials

The selection of electrode material is also an important issue to affect the electrochemical performance of all-solid-state lithium batteries. On the one hand, the poor contact between the solid electrolyte and electrode material can cause a large interface contact resistance[123]. On the other hand, traditional electrode materials for lithium-ion batteries cannot meet the requirements of higher energy density of batteries. Therefore, the improvement of the compatibility and stability of the electrode/electrolyte interface and the development of new electrode materials with high specific capacity are the key issues to achieve high-performance all-solid-state lithium batteries.

According to the different electrochemical reaction mechanisms of active materials, there are seven types of active materials used in all-solid-state lithium batteries with sulfide solid electrolytes.

2.2.2.1. Transition metal oxide and phosphate cathodes based on de-intercalation reaction (3.5–5.0 V)

Cathode materials working at high voltage mainly include lithium intercalation transition metal oxides ($LiCoO_2$, $LiNiO_2$, $LiNi_{0.8}Co_{0.15}Al_{0.05}O_2$, $LiNi_{1/3}Co_{1/3}Mn_{1/3}O_2$, $LiMn_2O_4$, etc.) and phosphates ($LiFePO_4$, $LiCoPO_4$, $Li_3V_2(PO_4)_3$, etc.)[124-134]. The electrochemical reaction mechanism of them is based on the intercalation/de-intercalation reaction of lithium ions, resulting in good structural stability and long cycle life. When employing oxide cathode material as ionic conductor, the lithium ions transport from the electrolyte to the electrode side because of the chemical potential differences. At the same time, space charge layers will be formed in the electrode and the electrolyte, respectively. When introducing oxide cathode material as a hybrid conductor, the electrons can neutralize the concentration of lithium ion of the electrode layer, leading to the disappearance of space charge layers. In order to achieve chemical potential equilibrium, the lithium ions in the sulfide solid electrolyte migrate to the positive electrode side and enhance the space charge layer, resulting in the formation of lean Li layer between the electrolyte and electrode, which causes a large interfacial impedance[135]. In order to reduce the interface impedance and improve the rate performance of all-solid-state

lithium batteries, an oxide film with ionically conductive and electronically insulating between the cathode and the electrolyte would be introduced, which can inhibit the emergence of a space charge layer. The interfacial buffer layers are categorized in two types, space charge layers between oxide electrode and sulfide solid electrolyte and oxide buffer layer inserted into the electrode/electrolyte interfaces. Due to the similar chemical potentials of space charge layers and the electronic insulating properties of oxide buffer layer, the space charge layer cannot form at the interface between the electrolyte and cathode materials[123].

OHTA et al.[136] introduced a method by using a fluidized bed to spray a layer of $Li_4Ti_5O_{12}$ and $LiNbO_3$ nanofilms on the surface of $LiCoO_2$ separately. The oxide nanofilms were employed as an interface modification layer for ionic conductivity/electronic insulation, which can eliminate the effecting of space charge layer. As shown in Figure 2-4, the interfacial impedance shortly decrease followed by the gradually increasing with the thickness increasing of the interfacial modification layer. When the thickness of layer reach 5 nm, the assembled all-solid-state lithium batteries with electrolyte of $Li_{3.25}Ge_{0.25}P_{0.75}S_4$ and Li-In alloy exhibit the ideal electrochemical performance. $Li_4Ti_5O_{12}$-coated $LiCoO_2$ shows a capacity retention ratio of 64% at a current density of 5 mA cm^{-2}. The $LiNbO_3$ nano

buffer layer with higher ionic conductivity can further reduce the interfacial impedance. With the same coating thickness and current density, the discharge capacity retention ratio of all-solid-state lithium batteries is increased to 74%.

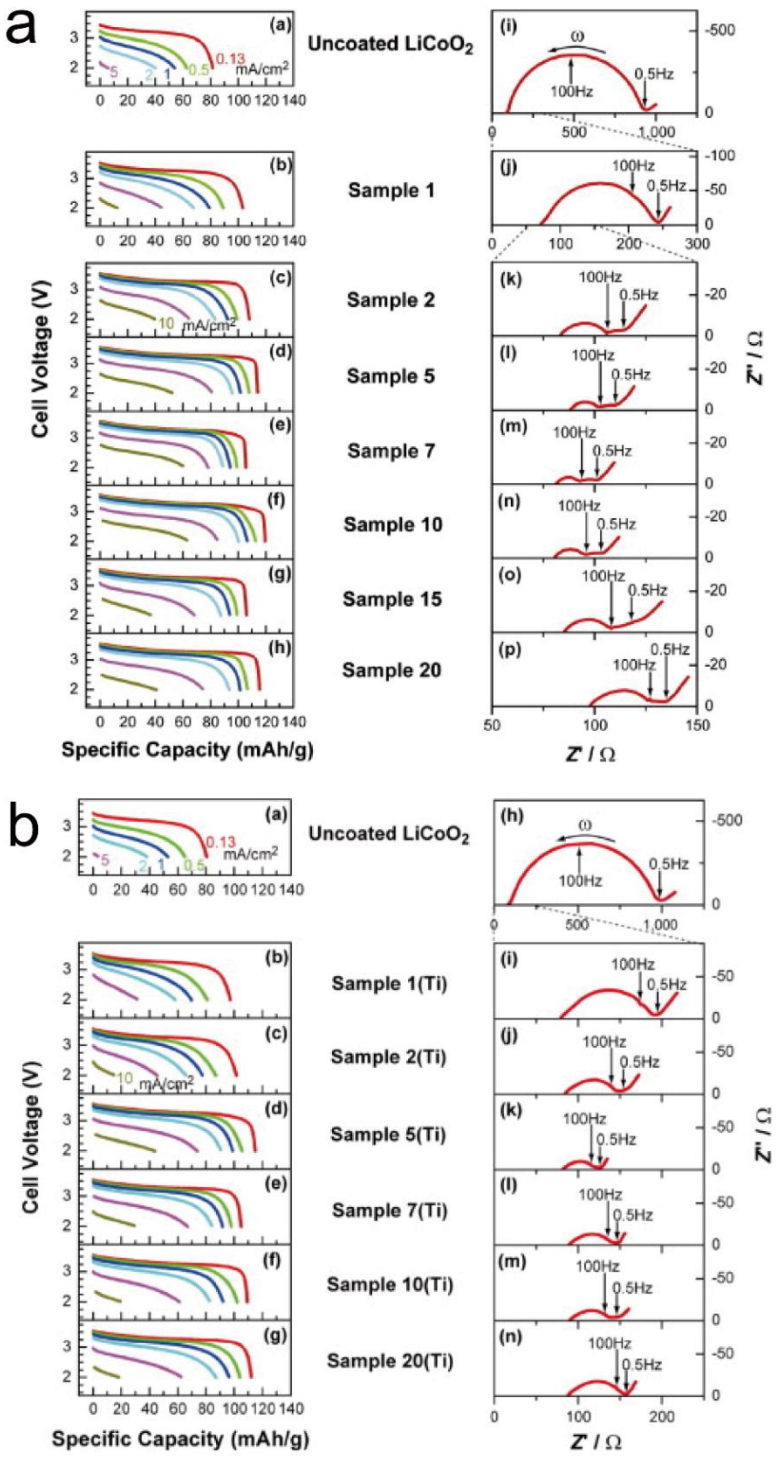

Figure 2-4 Galvanostatic discharge/charge and electrochemical impedance spectroscopy profiles of uncoated $LiCoO_2$ and $LiCoO_2$ coated with (a) $Li_4Ti_5O_{12}$ and (b) $LiNbO_3$[136].

SAKUDA et al.[137, 138] introduced a sol-gel method to coat SiO_2 and Li_2SiO_3 amorphous nanofilms on $LiCoO_2$, respectively, which not only inhibit the formation of space charge layer, but also eliminate interfacial side reactions, thereby reduce the interfacial resistance. The coating layer can affect the pre-index factor of the Arrhenius equation instead of conductive activation energy. The In/80Li_2S·20P_2S_5/$LiCoO_2$@Li_2SiO_3, In/80Li_2S·20P_2S_5/$LiCoO_2$@ SiO_2 and In/80Li_2S·20P_2S_5/$LiCoO_2$ all-solid-state lithium batteries exhibit capacities of 110, 80 and 60 mAh g^{-1} after 50 cycles at the current density of 0.1 C, respectively. The results illustrate that the ionic conductivity of the interfacial modification layer is crucial to improve the electrochemical performance of all-solid-state lithium batteries.

In addition, during the battery preparation and cycling process, the high-resistance interfacial layer can be formed due to the inter-diffusion reaction between the active materials and the solid electrolytes. Coating an oxide layer on the surface of active material can prevent the occurring of elemental diffusion and the formation of the interfacial layer, thus reducing the interfacial impedance and promoting the transport efficiency of lithium ions of the interfacial contact between the active material and solid electrolyte. Through characterization by using HRTEM and EDS, WOO et al.[139]

confirmed that a high-resistance interface layer with a thickness of 30 nm (including Co, S, and P elements) formed within the interface of $LiCoO_2/Li_{3.25}Ge_{0.25}P_{0.75}S_4$ after numerous cycles. Coating a Al_2O_3 thin layer on $LiCoO_2$ surface by atomic layer deposition (ALD) can inhibit elemental diffusion and reduce the interfacial resistance.

SUMITA et al.[140] simulated the charge-discharge state of the $LiFePO_4/Li_3PS_4$ interface by density functional-molecular dynamics (DF-MD). Due to the band matching and chemical potential difference within the $LiFePO_4/Li_3PS_4$ interface, a lean Li layer formed in the sulfide electrolyte during the charge process, resulting in the instability of the interface. Employing an oxide interface layer can reduce the interface impedance. SAKUDA et al.[141] synthesized a $LiFePO_4$ glass-ceramic cathode material. Through constructing a layer of nano-amorphous lithium phosphate on the cathode surface, the resultant $LiFePO_4/Li_2S\text{-}P_2S_5$ can effectively improve the velocity of charge transfer. As a result, the as-prepared $LiFePO_4$ glass-ceramic electrode materials exhibit higher discharge specific capacity than that of commercialized $LiFePO_4$.

Furthermore, due to the volume change within the cathode layer during the charge-discharge process, a large stress/strain can occur at the interface of the cathode, resulting in layer pulverization and poor solid-solid contact. Reducing the particle size or coating thin layer

on the cathode surface can effectively alleviate the problems of volume change and stress concentration, which are beneficial to lithium ion migration and cycling stability. OKUMURA et al.[142] introduced buffer layers of NbO_2, ZrO_2, or MoO_2 at the $LiCoO_2$/LATP interface by pulsed laser deposition (PLD). The insertion of NbO_2 can not only reduce the activation energy of interfacial charge transfer, but also inhibit the dramatic change of Co-O valence during the de-lithiation process, alleviating the interfacial stress caused by volume change.

In order to further improve the energy density of all-solid-state lithium batteries, ternary cathode materials with high-capacity ($LiNi_{0.8}Co_{0.15}Al_{0.05}O_2$(NCA), NCM) and $LiNi_{0.5}Mn_{1.5}O_4$ (LNMO), $LiCoMnO_4$ with high-voltage of 5 V are used in all-solid-state lithium batteries. XU et al.[143, 144] prepared a core-shell $LiAl_xCo_{1-x}O_2$ electrode by using annealing method, releasing a discharge specific capacity of 115 mAh g^{-1} and 84 mAh g^{-1} with the current density of 1 C and 5 C at room temperature, respectively. The aluminum-rich layer on the cathode surface can reduce the interface impedance when used as a buffer layer. Due to the higher ionic conductivity of $Li_{10}GeP_2S_{12}$, the assembled battery achieved an initial discharge specific capacity of 123.1 mAh g^{-1} at 0.1 C with a Coulombic efficiency of 69.1%. Furthermore, the particle size,

surface impurities, and defects of the NCA are also investigated. The results showed that the particle size can be reduced by mechanical ball milling and corresponding to the intimate solid-solid contact. The impurities and defects of cahode suface can also be removed by annealing process. The resultant NCA/ $Li_{10}GeP_2S_{12}$ battery display an initial discharge specific capacity and coulombic efficiency of 146 mAh g^{-1} and 76% at 0.1 C, respectively.

To address the poor compatibility of spinel $LiNi_{0.5}Mn_{1.5}O_4$ (5 V)with sulfide solid electrolytes, TATSUMISAGO et al.[145] coated Li_3PO_4 on the surface of LNMO by PLD technology. Although the buffer layer reduces the interface impedance between the LNMO and Li_2S-P_2S_5, the average operating voltage of In/80%Li_2S-20%P_2S_5/LNMO all-solid-state battery only display 4.7 V with a low discharge specific capacity of 62 mAh g^{-1}. KANNO et al.[146] investigated the electrochemical performance and capacity fade mechanism in $LiNbO_3$-LNMO/LGPS/Li all-solid-state lithium batteries. It shows initial discharge specific capacity of 80 mAh g^{-1} and the capacity retention rate of 75% after 10 cycles (Figure 2-5). The main reasons for the severe capacity fading can be attributed to:

(1) The irreversible reaction between the electrodes and sulfide solid electrolyte.

(2) Irreversible side reaction occurs in the cathode layer when charging to 5 V.

(3) The unstable performance of LGPS-AB interface, resulting in the decomposition of the LGPS electrolyte.

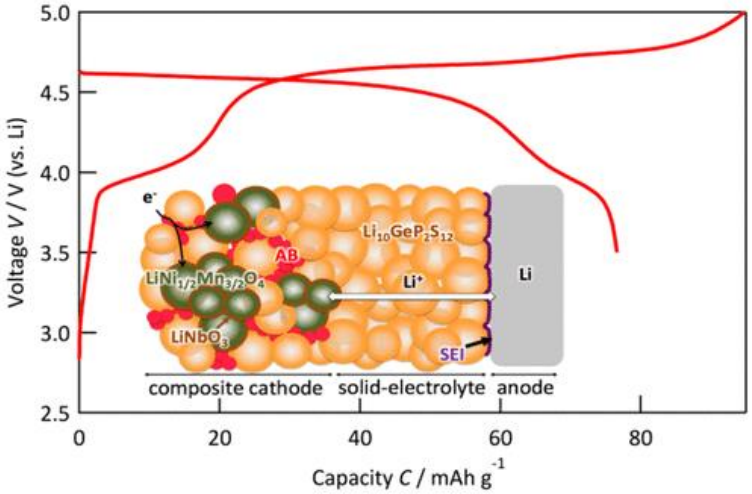

Figure 2-5 Galvanostatic discharge/charge profiles and Schematic of the interfacial reactions of $LiNbO_3$-LNMO/LGPS/Li[146].

Although lithium-insertion transition metal oxides and phosphate cathode materials exhibit high discharge voltages, the limited reversible capacity still narrows the application field in all-solid-state lithium batteries. At the same time, the interfacial compatibility and stability between the oxide cathode and the sulfide solid electrolyte have not been fully resolved. Therefore, it is critical to develop cathode materials with higher specific capacities and desired compatibility.

2.2.2.2. Chalcogenides based on lithium-sulfur and lithium-selenium reactions (~2.0 V)

Compared with traditional oxide cathode materials, chalcogenides and chalcogen elements can release higher specific capacities than those of lithium intercalated transition metal oxides and phosphate cathode materials. At the same time, the sulfide cathodes and sulfide solid electrolytes show similar chemical composition and chemical potential, thus suppressing the formation of serious space charge layer when combining them together. Using chalcogenide cathode materials instead of traditional oxide cathode materials can meet the requirement of all-solid-state lithium batteries with high-energy and long-life [147-151].

Lithium-sulfur battery is an emergent secondary battery system, which employ sulfur or lithium sulfide as the active material of the cathode electrode consist with lithium metal anode material. During the discharge process, lithium ions extracted from the anode material to the cathode side, S–S bonds of the sulfur are broken and combine with lithium ions to form insoluble lithium sulfide[132-134, 152-154].

During the discharge progress, the electrochemical reactions and transportations proceed inversely. The reversible reaction

between chemical and electrical energy proceed through the broken and formation of S–S bonds, as shown in Figure 2-6[29].

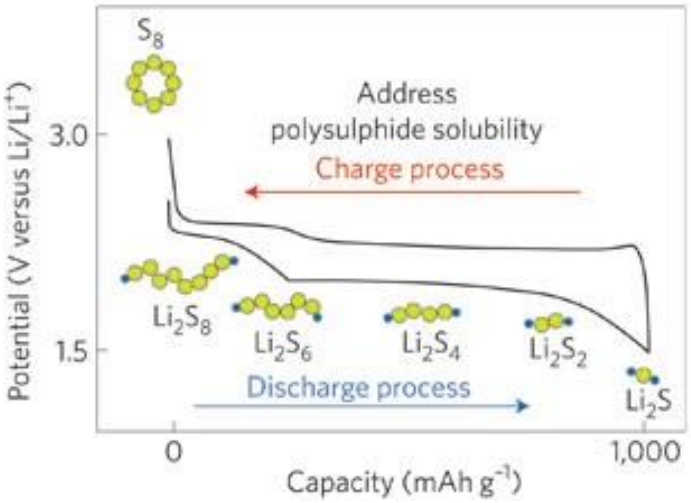

Figure 2-6 Galvanostatic discharge/charge curves and intermediates of lithium-sulfur batteries[29].

The electrochemical reaction equation of Sulfur cathode is shown as below:

Cathode:

$$S_8 + 16Li^+ + 16e^- \leftrightarrow 8Li_2S \quad (1)$$

Anode:

$$Li \leftrightarrow Li^+ + e^- \quad (2)$$

Total reaction equation:

$$S_8 + 16Li \leftrightarrow 8Li_2S \quad (3)$$

Based on equations of conversion reaction, lithium sulfides are formed by the reaction of one sulfur with two lithium ions, resulting in two electrons transition during the charge-discharge process. Because of the low molar mass of sulfur atom, the theoretical specific

capacity of sulfur can reach 1675 mAh g^{-1}, which is about ten times than that of traditional lithium intercalated transition metal oxide or phosphate cathode materials. Lithium-sulfur batteries can also display a high weight energy density (~ 2600 Wh kg^{-1}) and volume energy density (~2200 Wh L^{-1}), which also higher than that of cathodes using in commercial lithium-ion batteries. Furthermore, lithium-sulfur batteries show great potential in the field of energy storage because of the properties of abundant raw materials, non-toxicity and environmental friendliness[1, 155].

The electrochemical reaction process of liquid electrolyte based lithium-sulfur battery proceeds in complex multi-steps. Typically, the reduction reaction from S to Li_2S during the discharge process can be divided into three stages, corresponding to two discharge voltage platforms of 2.4 and 2.1 V, respectively. The first stage of 2.4 V attribute to two-step reduction reactions from S_8 to S_6^{2-}. During this period, the long-chain polysulfides was generated.

$$S_8 + 2e^- \rightarrow S_8^{2-} \quad (4)$$

$$3S_8^{2-} + 2e^- \rightarrow 4S_6^{2-} \quad (5)$$

The second stage is located between the 2.4 V and 2.1 V, corresponding to the formation of S_4^{2-}:

$$2S_6^{2-} + 2e^- \rightarrow 3S_4^{2-} \quad (6)$$

The third stage is located from 2.1 V to the cut-off voltage of discharge period, corresponding to the further reducing process from long-chain polysulfides to insoluble Li_2S:

$$S_4^{2-} + 2e^- + 4Li^+ \rightarrow 2Li_2S_2 \quad (7)$$

$$Li_2S_2 + 2e^- + 2Li^+ \rightarrow 2Li_2S \quad (8)$$

Because of the slow solid-state reaction kinetics of insoluble Li_2S_2 and Li_2S, the final product is generally in form of a mixture of them, and the actual discharge specific capacity is lower than the theoretical value. During the charge process, two voltage platforms of 2.2 and 2.5 V correspond to the forming of insoluble Li_2S_2 and soluble Li_2S_x ($4<x\leq8$), respectively.

Although liquid electrolyte based lithium sulfur batteries have significant advantages compared with other battery systems, some problems need to be solved either[156]:

(1) Sulfur and lithium sulfides (Li_2S_2 and Li_2S) possess low electronic and ionic conductivity, which could increase the resistance of the whole battery, and reduce the utilization of active materials as well as Coulombic efficiency.

(2) During the charge-discharge process, the reversible transition between S and Li_2S would lead to severe volume changes, which lead to the forming of cracks within the cathode layer.

(3) The shuttle effect occurs between the cathode and anode during the charge-discharge process, which is generated under the effect of concentration and electric field gradients. It causes soluble polysulfides (Li_2S_x, $4<x\leq8$) reduced into insoluble Li_2S and deposit on the surface of the anode, resulting in a reduction of active materials and corrosion of the lithium metal. Moreover, some electrochemical processes are irreversible and cause the decreasing in Coulombic efficiency.

(4) Lithium dendrites can be formed by lithium deposition during the charge process, which can cause internal short circuit, resulting in safety concerns.

In order to deal with these problems, many strategies have been proposed, including the introduction of conductive additives or construction of conductive networks to promote electrons migration; optimization of the cathode structure to shorten the diffusion pathway of lithium ions; the increasing of the specific surface area within cathode materials and the reduction of the thickness of the Li_2S_2 or Li_2S layer; designing of appropriate cathode materials with appropriate porosity and structural strength to alleviate volume changes and stress/strain during the charge-discharge process; and selection of appropriate electrolyte additives to prevent lithium dendrites from growing[157].

Although some carbon-based materials and metal compounds are currently introduced into lithium-sulfur batteries to improve electronic conductivity and adsorb soluble polysulfides, the shuttle effect of soluble polysulfides cannot be completely eliminated in liquid electrolyte based lithium-sulfur batteries. All-solid-state lithium-sulfur batteries using inorganic solid electrolytes are able to completely solve the polysulfide shuttle effect. However, volume changes during charge-discharge process would increase the solid-solid interface stress/strain and interface impedance, leading to a low electrochemical reaction kinetics. Improving the electronic/ionic conductivity and structural stability of sulfur become chanllenges to achieve high-performance all-solid-state lithium-sulfur batteries[158-160].

HAYASHI et al.[161, 162] reported a method to prepare mixtures of S-CuS and Li_2S-Cu by mechanical ball milling. During the charge and discharge process, S and CuS participate into the electrochemical reaction, the Li-In/80%Li_2S-20%P_2S_5/S-CuS all-solid-state lithium-sulfur battery exhibit specific discharge capacity of 650 mAh g^{-1} after 20 cycles. Li_2S and Cu form Li_xCuS with high electrochemically activation performance during the mechanical ball milling process, thereby improving electrochemical performance. The Li-In/80%Li_2S-20%P_2S_5/Li_2S-Cu all-solid-state lithium-sulfur

battery release an initial discharge specific capacity of 490 mAh g^{-1} and maintain 350 mAh g^{-1} after 20 cycles.

KANNO et al.[163] prepared S-AB composite with particle size of 1–10 nm by gas-solid mixture method. Compared with the mechanical ball milling method, S-AB show a intimate contact within the cathode layer. Li-Al/$Li_{3.25}Ge_{0.25}P_{0.75}S_4$/S-AB all-solid-state lithium-sulfur battery release an improved initial discharge specific capacity from 120 mAh g^{-1} to 590 mAh g^{-1}. After 15 cycles, the capacity still remains 420 mAh g^{-1}. Subsequently, KANNO et al.[164] synthesized S/CMK-3 composite, which not only improve the electric conductivity, but also inhibit the volume change of S, resulting in improved electrochemical performances of all-solid-state battery. The Li-Al/$Li_{3.25}Ge_{0.25}P_{0.75}S_4$/S/CMK-3 show a high capacity of 700 mAh g^{-1} after 10 cycles.

TATSUMISAGO et al.[165, 166] prepared two different cathode composites by mechanical ball milling method, obtained S-AB-SE and Li_2S-AB-SE composite cathodes. Sulfur in the S-AB-SE shows amorphous structure with small particle size. The assembled Li-In/80%Li_2S-20%P_2S_5/S-AB-SE all-solid-state lithium-sulfur battery maintain discharge specific capacities of 853 and 996 mAh g^{-1} under the current densities of 1.3 and 0.64 mA cm^{-2} after 200 cycles at room temperature, respectively. The Li_2S-AB-SE improves

interfacial contact between the electrolyte and cathode by reducing the particle size of Li_2S. Li-In/80%Li_2S-20%P_2S_5/Li_2S-AB-SE show reversible specific capacities of 800 and 270 mAh g^{-1} under 0.03 C and 3.5 C. Recently, SUN et al.[167] reported a Se-Li_3PS_4-C composite synthesized by mechanical ball milling. At room temperature, the Li-Sn/Li_3PS_4/Se-Li_3PS_4-C battery demonstrate an initial specific capacity of 652 mAh g^{-1} under 50 mA g^{-1} with an active material utilization of 96%. After 100 cycles, the reversible specific capacity remained the value of 585 mAh g^{-1}, corresponding to a capacity retention of 90%.

Although the electronic conductivity of the S-C composite can be increased by conductive carbon, the electronic and ionic conductivity of the solid electrolyte cannot be significantly improved by simply mixing. The velocity of charge transfer is essential for the efficiency of electrochemical reactions, which could influence the electrochemical performance. *In-situ* coupling conductive carbon and solid electrolytes with cathode material can improve the electronic and ionic conductivity of cathode materials. YAO et al.[168] employed the thiamine method to deposit a layer composed by amorphous sulfur nanoparticle (~10 nm) on the surface of graphene oxide. rGO can not only increase the electric conductivity, but also mitigates volume variations. The nano-level particle size can

also shorten the migration distance in lithium ions and increase the contact area within the cathode layer. The Li/LPOS/LGPS/rGO@S all-solid-state Li-S battery demonstrate an initial discharge specific capacity of 1629 mAh g^{-1} under the current density of 0.05C at 60 ^{o}C, which is close to the theoretical value. The specific capacity maintained 830 mAh g^{-1} under 0.1 C even after 750 cycles. LIANG et al.[169] synthesized nano-size Li_2S through precipitation method. By *in-situ* coating a thin layer of β-Li_3PS_4 solid electrolyte with a liquid-phase method, the Li_2S@β-Li_3PS_4 with core shell structure was successfully prepared. The high ionic conductivity and small particle size of this cathode composite can reduce the interface impedance and improve the rate and cycling performance of all-solid-state lithium batteries. At the temperature of 60 ^{o}C, the battery displays a reversible specific capacity of 402 mAh g^{-1} under 0.1 C with a capacity retention of 71 % after 100 cycles. TATSUMISAGO et al.[170] reported a solid solution of Li_2S-LiX (X=Cl, Br, and I) synthesized by mechanical ball milling. Doping LiX into the active material can not only improve the ionic conductivity, the utilization of Li_2S active material is also improved because LiI disperse into the Li_2S matrix to provide additional electrochemical reaction sites during charging process. The Li-In/75%Li_2S-25%P_2S_5/80Li_2S-20LiI battery show an initial specific capacity of 1090 mAh g^{-1} under 0.5

C with an active material utilization of 95% at 25 °C. Even after 2000 cycles, the battery can maintain a reversible specific capacity of 980 mAh g^{-1} under 2 C with a capacity retention of 100%. WANG et al.[171] introduced a method to construct the electronic/ionic conductive networks in the cathode materials, by dissolving Li_2S, Li_6PS_5Cl, and PVP in ethanol to induce co-precipitation, which was followed by high-temperature carbonization to form Li_2S-Li_6PS_5Cl-C composite. Li_2S and Li_6PS_5Cl nanoparticles homogenously distributed in the C matrix, improving the mechanical and conductive properties of the cathode composite. The Li-In/80%Li_2S-20%P_2S_5/Li_2S-Li_6PS_5Cl-C release a reversible specific capacity of 830 mAh g^{-1} under the current density of 50 mA g^{-1} for 60 cycles.

2.2.2.3. Transition metal polysulfides based on anionic redox reactions (~2.0 V)

Although *in-situ* combining carbon material or solid electrolytes with active materials can construct an effectively electronic/ionic conductive network within cathodes, most all-solid-state lithium-sulfur batteries could operate at high temperatures (60 °C) due to the intrinsic insulating properties of S or Li_2S as well as the slow charge transfer kinetics of the solid-solid interfacial contact. In order to allow all-solid-state Li-S battery demonstrate excellent

electrochemical performance at room temperature, suitable active materials are essential. High theoretical specific capacity, similar operating voltages with electrolyte, high electronic/ionic conductivity at room-temperature and low cost as well as convenient preparation processes become the challenges to realize high electrochemical performances of batteries[172].

The classical oxide cathode materials and transition metal sulfides display different reaction mechanism during the charge/discharge process. For classical lithium intercalation process in oxide cathode materials, due to the 3d metal cationic band is much higher than the p band of oxygen, the ion-electron transfer reactions occur from lithium to the lowest unoccupied energy level of the transition metal d band in ionic oxides. Discharge/charge (lithium ions intercalation/de-intercalation) process relies on the d metal level to host/release the associated electrons, which is called cation-driven redox process. For transition metal sulfide materials, the p band of sulfur is located in a higher position and therefore closer or even penetrate the d band of transition metal (Figure 2-7). Due to the charge transfer donation of these two bands, the anionic redox process is triggered, which can improve the reversible capacity of the battery, [172].

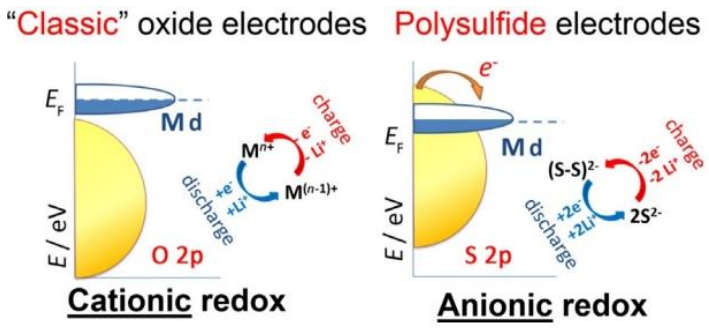

Figure 2-7 two mechanisms of redox activity in electrode materials[172].

As shown in Figure 2-8, the specific capacity comparison of various cathode materials are shown in the plot, where the x axis indicates the specific capacity based on the total weight of cathode and anode layer, the y axis shows the value of voltage plateau. Traditional cathode materials such as $LiNi_xCo_yMn_{1-x-y}O_2$ and $LiFePO_4$ only can display the specific capacity of 150–250 mAh g^{-1}, while the sulfide based cathode materials can reach ~700 mAh g^{-1}.The transition metal sulfides such as a-TiS_4[173], NiS_2[174, 175] and TiS_3[175] have been widely studied in all-solid-state batteries due to low cost of raw materials and abundant yields. Meanwhile, the relatively high transport kinetics can promote the conductivities and reducing charge transfer resistance. Furthermore, sulfide electrolytes show superior compatibility with transition metal sulfide cathodes due to similar chemical potential, thus realizing high energy density[176, 177].

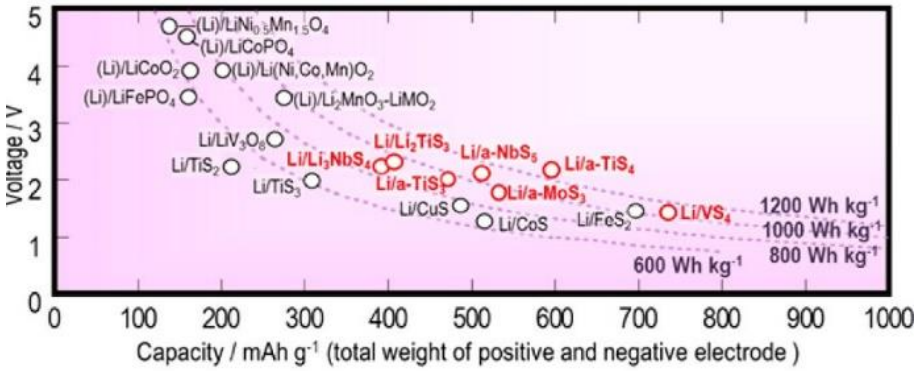

Figure 2-8 Specific capacity comparation of various cathode materials[172].

1970s–1980s, scientists explored the application of transition metal chalcogenides for lithium-ion batteries. Recently, advanced characterization and simulation techniques have been utilized into the reaction mechanism analysis of metal sulfides. Depending on the different properties, the reaction mechanism of cathode materials during the charge and discharge is divided into two categories: intercalation reactions and conversion reactions. In conventional intercalation-based materials, Li ions could be stored in the lattice of electrode without dramatically structural changes.

Reversible intercalation/de-intercalation reaction equation:

$$x\mathrm{Li}^+ + \mathrm{MQ}_y + x\mathrm{e}^- \leftrightarrow \mathrm{Li}_x\mathrm{MQ}_y \quad (9)$$

Cathode materials based on the conversion reaction would be completely decomposed when react with Li ions.

Reversible conversion reaction equation:

$$x\mathrm{Li}^+ + \mathrm{MQ}_y + x\mathrm{e}^- \leftrightarrow \mathrm{Li}_x\mathrm{Q}_y + \mathrm{M} \quad (10)$$

Although these materials can exhibit high theoretical specific capacity, poor reversibility and high voltage hysteresis could be induced due to the large volume variation.

Due to the abundant resources and low price of natural pyrite, it has been explored as active material for all-solid-state lithium batteries. The cubic-FeS_2 with a high theoretical specific capacity value (894 mAh g^{-1}), has been widely studied. During the initial discharge process, FeS_2 firstly transits into the Li_2FeS_2 interphase due to the intercalation reaction. Then Li_2FeS_2 is completely converted into Fe^0 and Li_2S. The subsequent cycling process display a complex electrochemical reaction mechanism that the FeS_2 phase would not generate again during the initial charge process and following cycles. Attribute to the cleavage/formation of S–S bonds, the anionic redox-driven reaction mechanism is proceeded and provide a high specific capacity of FeS_2[178].

LEE et al.[179] synthesized cubic-FeS_2 by solvothermal method, it can release a high reversible discharge specific capacity, which is pretty close to the theoretical value (894mAh g^{-1}) when assembled in Li/$77.5Li_2S{\cdot}22.5P_2S_5$/$FeS_2$ all-solid-state lithium battery. Owing to the four-electron reaction and advanced battery system, the specific capacity is significantly higher than liquid battery system, as shown in Figure 2-9.

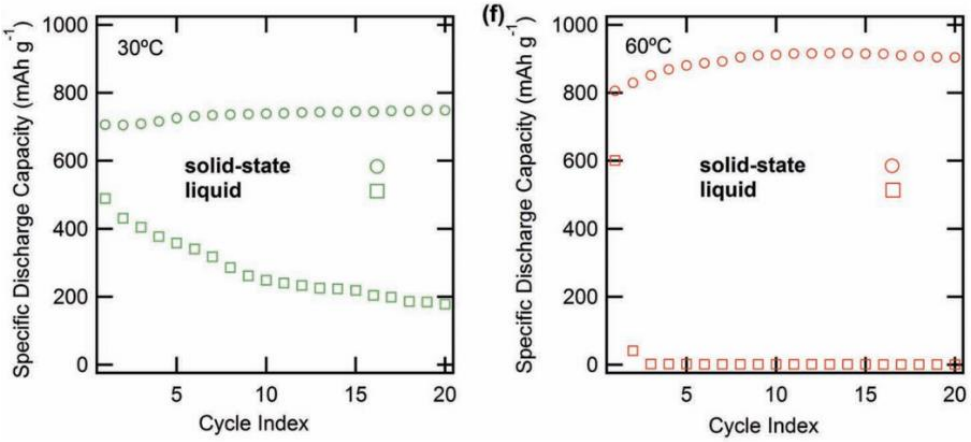

Figure 2-9 Cyclic performances of cubic FeS_2 assembled in two different battery systems[179].

Transition metal sulfides display electrochemical activity performances when employed in the lithium-sulfur battery and possess the fixation/trapping properties for polysulfides in conventional liquid lithium-sulfur batteries. Recently, PASSERINI et al. [108] successfully prepared C-FeS_2-S composite with different mixing ratio by mechanical ball milling, which was introduced as cathode materials in LI/LiI-Li_3PS_4/CFS(5:5) all-solid-state lithium-sulfur batteries. It releases a discharge specific capacity of 1200 mAh g^{-1} after 20 cycles with active material loading of 1 mg cm^{-2}. When the loading of active material increased to 5 mg cm^{-2}, the specific capacity would be slightly decreased (710 mAh g^{-1}).

As a cathode material with amorphous structure, TiS_3 shows a high theoretical specific capacity of 558 mAh g^{-1} and a moderate operating voltage. HAYASHI et al.[180, 181] synthesized amorphous

TiS_3 by mixing TiS_2 and S together using high-energy ball milling. The assembled Li-In/80Li_2S-20P_2S_5/TiS_3 battery demonstrate an initial discharge specific capacity of ~400 mAh g^{-1}. After 10 cycles, the reversible specific capacity remain the capacity of 300 mAh g^{-1}. *Ex-situ* XRD and Raman results indicate that TiS_3 maintain the amorphous structure during cycling. Due to the open and random structural characteristics of amorphous materials, freedom transport pathway can be provided within the cathode, therefore obtain high reversible capacity and long cycle life. Experimental results demonstrate that the initial Coulombic efficiency and cycling stability of amorphous TiS_3 are better than those of crystalline TiS_3. XRD and HRTEM results illustrate the c-TiS_3 can be partially amorphized during the first discharge process, resulting in the consuming of irreversible capacity.

2.2.2.4. Layered transition metal disulfides based on intercalation/de-intercalation reaction (~2.0 V)

Scientists also successfully sythesized single-layer graphene by mechanical exfoliation in 2004, then ultra-thin two-dimensional nanomaterials has been prepared either. Graphene possesses a series of advantages such as high electrical conductivity, large specific surface area and good mechanical strength. Two-dimensional layered

transition metal disulfides MX_2 (M: transition metal, X: chalcogenide) show a similar structure with graphene, and display strong anisotropy performances in electrical, chemical, mechanical, and thermal properties. When inserting the transition metal into two layers of chalcogenides, an X-M-X sandwich structure could be formed, which could reach a ultra thin thickness of 6-7 Å for single layer. These layers are stacked by van der Waals forces, the M-X located in in-plane is connected by covalent bonds. Therefore, single or few layers of transition metal disulfides can be obtained from transition metal disulfides by exfoliation process. Depending on the different physical properties, transition metal disulfides could be divided into insulators (HfS_2), semiconductors (MoS_2, WS_2), semimetals (WTe_2, $TiSe_2$), and metals (NbS_2, VSe_2). Most transition metal disulfides have three homogeneous phases of triclinic (1T), hexagonal (2H) and trigonal (3R), which can proceed phase transition under certain conditions. Transition metal disulfides possess a wide application range, which can be utilized in catalysis, energy storage, sensor, and electronics devices[182, 183].

Transition metal disulfide also show great potential in the field of electrochemical energy storage[184-187]. In general, transition metal disulfides exhibit a desirable theoretical specific capacity, which is higher than that of conventional lithium-ion battery.

However, most of transition metal disulfides show the property of semiconductor with low conductivity, resulting in poor rate performance. In addition, continuous lithium-ion intercalation/de-intercalation leads to structural destruction and electrode pulverization, corresponding to rapid capacity fade. As a result, they exhibit poor electrochemical performance in lithium-ion batteries. Two-dimensional transition metal disulfides with high specific surface area can provide abundant electrochemical reaction sites, as following reduce the de-intercalation energy barrier of lithium ions, as a results shorten the charging diffusion distance. However, due to the high surface free energy and van der Waals attraction, 2D transition metal disulfides are easily restacked on the cathode surface and form a layered structure similar with that of bulk materials. This condition not only lead to the structure loss of 2D material, but also affects the electrochemical performance. There are three types of 2D transition metal disulfides electrodes for lithium-ion batteries: Self-assembled structures of transition metal disulfides nanosheets, 2D transition metal disulfides with increased d-spacing and 2D transition metal disulfides matrix composite.

As a typical member of transition metal disulfides, layered MoS_2 has wide applications in transistors, biosensors and energy storage devices[188]. Layered MoS_2 exhibits a high theoretical

specific capacity of 670 mAh g^{-1}. The layer spacing can provide more suitable space for lithium ions. As a cathode material, the chemical reaction equations of discharge/de-intercalation process are summarized as follows:

De-intercalation:

$$MoS_2 + xLi^+ + xe^- \leftrightarrow Li_xMoS_2 \quad (11)$$

Conversion:

$$Li_xMoS_2 + (4-x)Li^+ + (4-x)e^- \leftrightarrow Mo + 2Li_2S \quad (12)$$

ADAMS et al.[189] applied MoS_2 in In-Li/Li_6PS_5Br/MoS_2 all-solid-state batteries. After the initial discharge process, MoS_2 is converted into Li_2S and Mo. Mo nanoparticles are homogenously distributed in the cathode layer, and Li_2S participates to the following reaction during the subsequent cycles. At room temperature, the battery exhibits reversible capacity of 190 mAh g^{-1} after 40 cycles. When the temperature increased to 70 °C, the battery remains reversible capacity of 270 mAh g^{-1} under the current density of 0.2C after 700 cycles with capacity retention of 85%. The particle size of MoS_2 limits the value of reversible capacity, it is necessary to prepare nanostructure MoS_2 in the future to improve the electrochemical performance of all-solid-state batteries. TU et al.[190] designed a cathode composite by *in-situ* coating $Li_7P_3S_{11}$ solid electrolyte thin layer on the MoS_2 particle surface with a liquid phase method,

resulting in a $MoS_2@Li_7P_3S_{11}$ composite. The $Li/Li_7P_3S_{11}/MoS_2@Li_7P_3S_{11}$ all-solid-state battery show an initial discharge specific capacity of 868.4mAh g^{-1} under 0.1C, the corresponding Coulombic efficiency is 77.1%. It also maintained a reversible capacity of 238.1 $mAhg^{-1}$ under 1 C after 400 cycles, as shown in Figure 2-10. Reasonable interface modification not only increases the contact area between the cathode and solid electrolyte, but also provides more active sites in charge process, thus improving the utilization of active materials. In addition, the coating layer can also alleviate the volume change, ensuring an excellent interfacial contact, and improving the cycling stability of the battery.

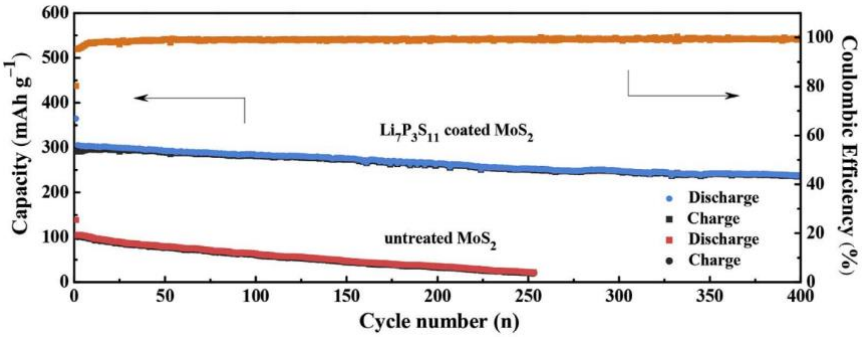

Figure 2-10 Cyclic performances of $Li/Li_7P_3S_{11}/MoS_2@Li_7P_3S_{11}$ all-solid-state battery[190].

The intercalation reaction based TiS_2 was applied into lithium batteries and exhibited high energy and power density in 1970s. TiS_2 was considered to be the most promising electrode material due to its high conductivity, high ion diffusion coefficient and light weight. WHITTINGHAM et al. reported that TiS_2 can exhibit high specific

capacity and cycling stability in lithium rechargeable batteries. LEE et al.[191] reduced the particle size of TiS_2 through high-energy ball milling, which can improve the utilization of active material and the dynamics of charge transmission. TiS_2 cathode based on de-intercalation reaction showed good rate performance in Li/77.5Li_2S-22.5P_2S_5/TiS_2 all-solid-state batteries. At 0.2 C, it can release an initial discharge specific capacity of 200 mAh g^{-1} with the capacity retention rate of 90% after 50 cycles. Even at the current density of 10 C, the battery can maintain a reversible capacity of 150 mAh g^{-1} after 50 cycles. JUNG et al.[191-193] prepared a TiS_2/ Li_2S-P_2S_5 nanocomposite by ball milling method. The obtained $Li_{0.5}In$/Li_3PS_4/TiS_2-SE all-solid-state lithium batteries exhibit initial discharge specific capacity of 416 and 837 mAh g^{-1} in the voltage range of 1.5–3.0 V and 1.0–3.0 V, respectively. After 60 cycles within the range of 1.5–3.0 V, the capacity retention can reach 95%. HRTEM and *ex-situ* XRD characterization techniques demonstrate that the additional capacity contribution arises from the generation of surface Li-Ti-P-S amorphous phases during ball milling process.

JUNG et al. also investigated the electrochemical performance differences of various battery structures for Li-In/TiS_2 all-solid-state batteries. Although LGPS possesses a higher ionic conductivity than LPS, the poor stability of LGPS at low potential range can cause

severe capacity degradation of solid-state batteries. Combining LGPS-LPS double-layer solid electrolyte with TiS_2-LGPS cathode composite can optimize the battery structure. Li-In/LGPS-LPS/TiS_2-LGPS all-solid-state batteries achieve a discharge specific capacity of ~60 mAh g^{-1} under the current density of 20 C in the voltage range of 1.5–3.0 V. The experimental results confirm that the ionic conductivity of the cathode layer is an important issue in the all-solid-state battery. The development of solid electrolytes with high ionic conductivity, the appropriate cathode material as well as reasonable battery structures are essential to improve the electrochemical performance of all-solid-state batteries. Single-layer TiS_2 nanosheets were prepared by mechanochemical and ultrasonic exfoliation method, which exhibited good electrochemical performance compared with bulk materials in Li-In/LGPS-LPS/TiS_2-NS all-solid-state batteries which is due to ultra-thin nanosheet structure not only increase the interfacial contact between the active material and the solid electrolyte, but also shortens the transport pathway of lithium ions, and finally improves the electronic conductivity.

YAO et al.[194] synthesized VS_2 nanoflowers by solvothermal method and use them as the active material in all-solid-state batteries. The Li/LPOS/LGPS/hc-VS_2 battery maintains a reversible specific

capacity of 532.2 mAh g^{-1} under current density of 50 mA g^{-1} with 30 cycles. The reversible specific capacity remains 436.8 and 270.4 mAh g^{-1} under the current density of 100 and 500 mA g^{-1} after 100 cycles, as shown in Figure 2-11. VS_2 with high crystallinity demonstrates an outstanding electrochemical performance, due to the high conductivity and unique crystal structure.

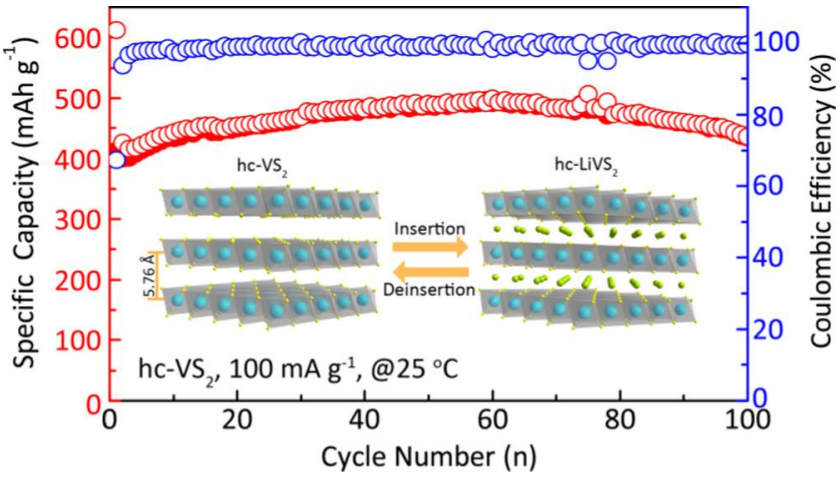

Figure 2-11 Crystal structure and cyclic performances of hc-VS_2 cathode material under the current density of 0.1 mA g^{-1}[194, 195].

2.2.2.5. Transition metal sulfides based on conversion reactions (1.0–2.0 V)

The transition metal sulfides based on conversion reactions are different from the cathode material with intercalation/de-intercalation reactions, which can react with lithium ions via

chemical bond breaking/rebuilding [1, 196, 197]. The reaction equation for the conversion reaction is shown as below:

$$M_aX_b + (bn)Li^+ + (bn)e^- \leftrightarrow aM^0 + bLi_nX \qquad (13)$$

Where M represents transition metal elements (Fe, Co, Ni, Cu, Mn, etc.), X is anion (O^{2-}, S^{2-}, Se^{2-}, F^-, P^{3-}, etc.), *n* is the oxidation state of anions, and 0 reflects the reduction of transition metals into metallic state. During the first discharge process, the transition metal compound reacts with lithium ions and converted into nanoparticles M^0 and lithium compounds Li_nX. The M^0 nanoparticles are uniformly dispersed in the Li_nX matrix and form M^0/Li_nX nanocomposite phase. Subsequently, during the charge process, lithium ions in Li_nX are de-intercalated and react with the transition metal nanoparticle M^0 to form M_aX_b. The conventional transition metal compounds used as cathode materials in lithium battery include metal fluoride, oxide, nitride, sulfide, selenide, phosphide, etc. Among them, the transition metal fluorides and sulfides possess higher theoretical potentials.

In the most of transition metal sulfides which are based on the conversion reaction, CuS exhibits a higher discharge voltage (~2.0 V vs. Li/Li^+) and a theoretical specific capacity of 560 mAh g^{-1}. ADAMS et al.[198] applied CuS as an active material used in Li-In/Li_6PS_5Br/CuS all-solid-state batteries to explore the electrochemical properties and reaction mechanisms. The all-solid-

state battery has initial discharge capacity of 650 mAh g^{-1} under the current density of 0.02 C. After 20 cycles, the battery remains a reversible capacity of 90 mAh g^{-1}. The high-resistance $Cu_yLi_{6-y}PS_5Br$ interphase could be formed by the reaction between Li_6PS_5Br and CuS. The large volume change of the electrolyte can cause cracks of the composite and separate the cathode from the electrolyte, resulting in rapid capacity decay and poor cycling performance of solid-state batteries. HAYASHI et al.[199] applied $Cu_xMo_6S_{8-y}$ as an active material in all-solid-state lithium batteries. It displays a reversible capacity of ~200 mAh g^{-1} at the current density of 20 C at 120 ºC after 50 cycles. The high discharge specific capacity and rapid capacity decay are mainly due to Cu diffusing into the Li_2S-P_2S_5 solid electrolyte at high temperatures, resulting in an increase in the internal resistance of the battery. Adding acetylene black AB into the cathode material can effectively inhibit the diffusion of Cu and improve the cycling performance of Li-In/Li_2S-P_2S_5/CuxMo_6S_{8-y}. the as-prepared battery remains reversible capacity of 190 mAh g^{-1} under 60 C after 100 cycles at 160 ºC. Besides, using chemical method can remove Cu from $Cu_xMo_6S_{8-y}$. The obtained Mo_6S_{8-y} can also improve the high-temperature cycling stability of the battery.

In order to improve the electronic/ionic conductivity and structural stability of transition metal sulfides based on conversion reactions, YAO et al.[200] synthesized a ~10 nm thin layer of $Li_7P_3S_{11}$ solid electrolyte, which was *in-situ* deposited on the surface of Co_9S_8 nanosheets by liquid phase method, not only improving the interfacial contact between the solid electrolyte and the active material, but also forming a good lithium-ion transition channel, and reducing the interface impedance of Li/LPOS/LGPS/Co_9S_8-LPS all-solid-state lithium battery. Consequently, an initial discharge specific capacity of 633 mAh g^{-1} at a current density of 0.38 mA cm^{-2} was achieved. The battery displays an initial Coulombic efficiency of 90.7%, and remains the reversible specific capacity of 421 mAh g^{-1} at 1.27 mA cm^{-2} after 1000 cycles, as shown in Figure 2-12.

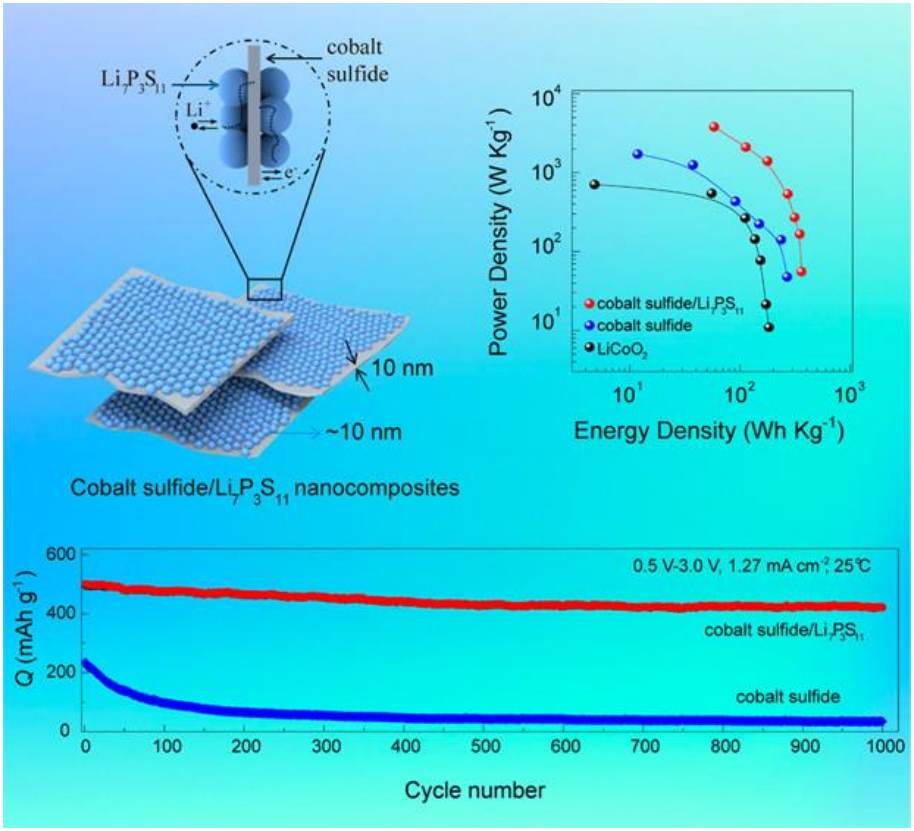

Figure 2-12 Schematic illustration, Ragone plot and Long-term cyclic performance of Li/LPOS/LGPS/Co_9S_8-LPS battery[200].

2.2.2.6. Anode material based on alloying reaction (< 1.0 V)

Graphite anode is mainly utilized in commercial lithium-ion batteries because of the long-term cyclic stability, abundant resources and low cost[201-208]. However, the theoretical specific capacity of the graphite is relatively low (375 mAh g^{-1}). A new material with low cost, high energy density and cycling stability is urgently demanded. Alloy anode materials exhibit high specific capacity, moderate working voltage and reliable safety performance[209-215]. However, the alloy anodes can undergo severe volume changes (up to 300%)

during alloying/de-alloying process, causing serious cracks of the electrode, and resulting in rapid capacity decay and poor cycling stability. The large irreversible capacity losing during the initial cycles also limits the practical application of alloys. To address these issues, tremendous works have been devoted:

(1) The alloy anodes with specific nanostructures, not only can eliminate the stress/strain occur caused by volume change, but also shorten the transmission distance of lithium ions and provide additional lithium storage sites.

(2) Nanocomposites by introducing carbon matrix to mitigate the volume change while increasing the electronic conductivity of the electrode.

(3) Alloying anode material with the second phase M. The second phase M not only alleviates volume changes during charge-discharge processes, but also enhances the electronic conductivity of anode materials. Two phases can mitigate both volume changes of anode when the second phase M display electrochemical activity[216-218].

Many metals such as Si, Sn, Sb, Al, Mg, Bi, In, Zn, Pb, Ag, Pt, Au, Cd, As, Gas, and Ge can react with lithium, where the Si, Sn, Sb, Al and Mg with the properties of low cost, abundant storage, and environmentally friendly have been widely studied as anode

materials[219-224]. Silicon displays a low discharge voltage (0.06 V vs. Li/Li^+) with a high theoretical specific capacity (4200 mAh g^{-1}), which is currently studied in many research works. However, the low initial Coulombic efficiency and large volume changing limit the large-scale application of Si anode in lithium-ion batteries[225, 226].

Takada et al.[227-230] have systematically studied the application of Si anode in all-solid-state batteries. Firstly, Li_2S and SiS_2 were introduced as raw materials to obtain amorphous Li_2SiS_3 cathode materials through high-energy ball milling method. The initial discharge specific capacity of Li-In/70Li_2S-30P_2S_5/Li_2SiS_3 ASSLB based on continuous conversion and alloying reaction is close to 2500 mAh g^{-1}, the high specific surface area of the active material results in high discharge specific capacity. However, the low electronic conductivity of Li_2SiS_3 lead to large irreversible capacity losses and poor Coulombic efficiency. Introducing conductive additives and reducing particle size can overcome the problem of low conductivity. Experiment results show that the Li_2SiS_3 thin film prepared by PLD method can shorten the electron transmission distance. Adding FeS into Si can increase the conductivity, resulting in a higher electrochemical performance than that of Si. Subsequently, amorphous Si nanofilms with the thickness of 50 nm were prepared by magnetron sputtering technology. The Li-In/70Li_2S-30P_2S_5/a-Si

all-solid-state battery can display a reversible specific capacity of 2500mAh g^{-1} under 10 mA cm^{-2} after 100 cycles. Takada et al. also explored the electrochemical performance when introducing a few amounts of O into amorphous Si nanofilms. During the conversion reaction period, the cycling performance of all-solid-state batteries can be enhanced due to the formation of a non-electrochemically active skeleton. O can effectively prolong the cycle life without reducing capacity and rate performance. The Li-In/70Li_2S-30P_2S_5/a-$SiO_{0.4}$ battery obtains a reversible capacity of more than 2800 mAh g^{-1} at 0.1 mA cm^{-2} after 100 cycles with the capacity decay of 0.06%.

LEE et al.[231-234] has also reported a work that assemble Si nanoparticles in Li/77.5Li_2S-22.5P_2S_5/Si all-solid-state batteries, the battery releasing an initial discharge specific capacity of 3127 mAh g^{-1} and an initial Coulombic efficiency of 43.7%. After 40 cycles, the battery exhibits a capacity retention of 66.9%. The electrochemical performance of nano-Si in all-solid-state batteries is significantly better than that of liquid based batteries. In order to solve the problem of volume expansion of Si anode, the following methods are utilized:

(1) Using conductive additives to alleviate the volume expansion and maintain the contact between the Si particles.

(2) Limiting the voltage window of charge and discharge processes, to reduce the degree of electrode pulverization, and

prolong the cycle life.

(3) Decreasing the particle size of Si to reduce the mechanical stress and capacity decay.

Through above three strategies, the traditional acetylene black can be replaced by multi-walled carbon nanotubes, leading to the increase in the specific surface area and electronic conductivity. The n-Si/MWCNT materials exhibit the best electrochemical properties over various voltage ranges. Limiting the cut-off voltage range to 0.05–1.0 V during the charge-discharge process, the specific discharge capacity of Li/77.5Li_2S-22.5P_2S_5/n-Si/MWCNT all-solid-state battery can be stabilized at 800 mAh g^{-1} after 100 cycles, which is significantly higher than that of bulk Si. However, due to the extremely low conductivity of Si, the loading amount of active material is limited in all-solid-state batteries. At the same time, the poor solid-solid interfacial contact between the active material and the solid electrolyte also inhibits the transportation of lithium ions. In order to increase the loading amount of the Si anode in all-solid-state batteries, it is necessary to increase the electronic and ionic conductivity of the active material. The nano-Si of Si-Ti-Ni ternary alloy embedded in the $Ti_4Ni_4Si_7$ matrix, which demonstrate a similar microstructure with the nano-Si anode, become an ideal anode material for lithium-ion batteries. However, due to the poor

conductivity of Si-Ti-Ni ternary alloys, pre-lithiated $Li_{3.2}Ti_4Ni_4Si_7$ hybrid conductors were synthesized through lithium metal powder (SLMP) to improve the electrochemical performance.

Si-C composite have been obtained from industrial waste asphalt by pyrolysis with a simple process. Soft amorphous carbon materials exhibit superior lithium storage and hybrid conductivity[235-237]. The Li-In/77.5Li_2S-22.5P_2S_5/Si-C all-solid-state battery display a discharge specific capacity of 1089.2 mAh g^{-1} after 100 cycles with a Coulombic efficiency of 99%. They also applied polypropylene nitrile as a carbon precursor to prepare Si/C fibers by using electrospinning and heat treatment. Experiments results shown that Si/C fibers with smaller diameter possess ideal capacity retention. The Li-In/77.5Li_2S-22.5P_2S_5/Si/C all-solid-state battery displays a reversible capacity of approximately 700 mAh g^{-1} after 70 cycles with a Coulombic efficiency of 99.2%.

The Sn can undergo an alloying reaction with Li to form the $Li_{17}Sn_4$ alloy phase, and each Sn atom can contain 4.25 Li atoms. The theoretical specific capacity of the Sn anode is 959.5 mAh g^{-1} with the operating voltage of 0.5 V (vs. Li/Li^+). Although the mass specific capacity of the Sn anode is lower than that of the Si and Li anodes, the volumetric specific capacity can reach about 2000 mAh cm^{-3}, featuring the highest value among these three anode materials.

However, just similar with other Li alloy materials, the alloying reaction of the Sn anode during charge-discharge process leads to dramatically volume expansion, causing rupture and pulverization of the anode, resulting in low capacity retention[238]. LEE et al.[239-241] employed Sn metal nano-powders as active material in Li-In/77.5 Li_2S-22.5P_2S_5/Sn all-solid-state battery. It exhibits reversible capacity of 800mAh g^{-1} at the current density of 0.1 C at 60 ºC for 50 cycles. In order to solve the volume expansion issue of the Sn alloy anode during the charge-discharge process, Sn is completely embedded in the one-dimensional C matrix. The one-dimensional C substrate not only improves conductivity, but also impedes the volume expansion. The porosity of carbon fibers is a major factor to influence the particle size and dispersion of Sn. The Li/77.5Li_2S-22.5P_2S_5/Sn/C all-solid-state battery maintained a reversible capacity of 762 mAh g^{-1} after 50 cycles with the Coulombic efficiency of 99.5%. Due to the advanced conductivity and stability, Sn can be used as an active carrier for Si. The Sn-Si alloy in Li-In/77.5Li_2S-22.5P_2S_5/Sn-Si all-solid-state battery maintained a reversible capacity of 1000 mAh g^{-1} after 50 cycles.

HAYASHI et al.[242, 243] prepared 80SnS·20P_2S_5 amorphous material with micro size by mechanical ball milling method. The Li-In/80Li_2S-20P_2S_5/80SnS·20P_2S_5 all-solid-state battery displays a

discharge specific capacity of 400 mAh g^{-1} at 64 μA cm^{-2} after 50 cycles. As a network former, P_2S_5 can effectively improve the discharge capacity and cycle stability of all-solid-state batteries. Besides, the liquid phase method was used to synthesize needle and sheet SnS by changing different coordination solvents. The Li-In/80Li_2S-20P_2S_5/SnS all-solid-state battery based on the alloying reaction, can release a reversible discharge specific capacity of 620 mAh g^{-1} at a current density of 0.13 mA cm^{-2} after 15 cycles. The primary reason of the improved electrochemical performance for needle-like SnS can be attributed to the improved solid-solid interfacial contact, which formed a continuous lithium-ion conductive channel in the composite.

In order to improve the interfacial contact between lithium metal and solid electrolyte, Li-In alloy is used as anode materials in many all-solid-state batteries. However, due to the high cost of In, Li-In alloys cannot meet practical applications.

2.2.2.7. Lithium metal anode materials (0 V)

Lithium metal possesses low electrode potential (−3.04 V vs. NHE) and high theoretical specific capacity (3862 mAh g^{-1}), which is an ideal anode material [7, 41, 244-250]. Using lithium metal in traditional liquid lithium-ion batteries can directly cause the

interfacial reaction between the lithium metal and electrolyte during the charge-discharge process, consequently forming a solid electrolyte interface film (SEI). At the same time, non-homogenously lithium deposition will cause lithium dendrite growth, resulting in dead lithium and lithium content loss, and increased interfacial impedance. Lithium dendrites may pierce the separator and cause short circuit and thermal runaway.

All-solid-state lithium battery using inorganic solid electrolytes instead of the traditional liquid electrolyte and separator, which is expected to improve the safety performance and energy density. However, due to the strong reducing nature, lithium metal can easily react with high-valent metal cations in the solid electrolyte, forming an intermediate layer with high interfacial impedance. Furthermore, despite solid electrolytes show the high mechanical strength, lithium dendrites can grow along grain boundaries and pores of solid electrolyte. In order to improve the interfacial stability between lithium metal and solid electrolyte, electrolyte surface modification, lithium metal surface modification and interfacial buffer layer are investigated.

JANEK et al.[251] categorized the interface between the lithium metal and solid electrolyte into two types:

(1) Thermodynamically stable interface, which means a two-

dimensional interface between the solid electrolyte and lithium metal without any reaction. In this condition, thermodynamically equilibrium between the lithium metal and solid electrolyte is achieved.

(2) Thermodynamically unstable interface. Driving by thermodynamics, the solid electrolyte reacts with lithium metal to form a three-dimensional interface. According to the charge transport characteristics of the reactive layer, the interface layer can be further divided into two categories:

a. Hybrid conductor interface. The reactants possess both electronic and ionic conductivity, the interfacial layer gradually grows within the solid electrolyte, and changing the properties of the entire block. The formation of a hybrid conductor interface will eventually lead to electrons pass through the entire solid electrolyte, causing self-discharge of the battery. Solid electrolytes containing multivalent cations tend to form interfaces of conductor mixture, the introduction of artificial SEI films can avoid the formation of mixed conductor interfaces.

b. Kinetically stabilized solid electrolyte interface. This interface layer is a stable thin film layer that display the performances of electronically insulating or low electrical conductivity, which can inhibit the further growth of the interface layer. The electrochemical

performances of all-solid-state battery is highly dependent on the ionic conductivity of the interfacial layer.

An *in-situ* characterization technique was designed to directly explore the reaction region of the solid electrolyte interface[252-254], as shown in the Figure 2-14. Typically, the argon ion beam was generated to attack the metal target, then a thin metal film was *in-situ* sputtering on the surface of the solid electrolyte. X-ray photoelectron spectroscopy was employed to observe the chemical reaction between the solid electrolyte and the metal. Subsequently, the interface reactions between the lithium metal and sulfide solid electrolytes with high ionic conductivity such as $Li_7P_3S_{11}$, $Li_{10}GeP_2S_{12}$, and Li_6PS_5X was characterized, respectively. The interfacial reactions were analyzed by *in-situ* X-ray photoelectron spectroscopy combined with time-dependent electrochemical impedance spectroscopy (EIS). For the $Li_7P_3S_{11}$ solid electrolyte, a non-growing interface layer was formed when react with lithium metal. The interphase mainly composed of the decomposition products of Li_2S and Li_3P. This interface layer is similar with the SEI film in a conventional lithium-ion battery. A layer with the thickness of 2.3 nm is obtained after a 30-hour standing in Li/$Li_7P_3S_{11}$/Li symmetrical battery. For the $Li_{10}GeP_2S_{12}$ solid electrolyte, it reacts with lithium metal to form a hybrid conductor interface, and the

interface layer gradually grows into the electrolyte. The interface layer is mainly composed of Li_2S, Li_3P, and Li-Ge alloys. The thickness of the interface layer in Li/$Li_{10}GeP_2S_{12}$/Li symmetrical battery is about 20 nm after standing for 30 h. For the Li_6PS_5X solid electrolyte, the solid electrolyte interface layer formed by reacting with lithium metal, which is mainly composed of Li_2S, Li_3P, and LiX. Among them, Li_6PS_5Cl and Li_6PS_5Br exhibit slow growth of SEI, which is similar with $Li_7P_3S_{11}$. Furthermore, Li_6PS_5I and $Li_{10}GeP_2S_{12}$ exhibit high SEI impedance.

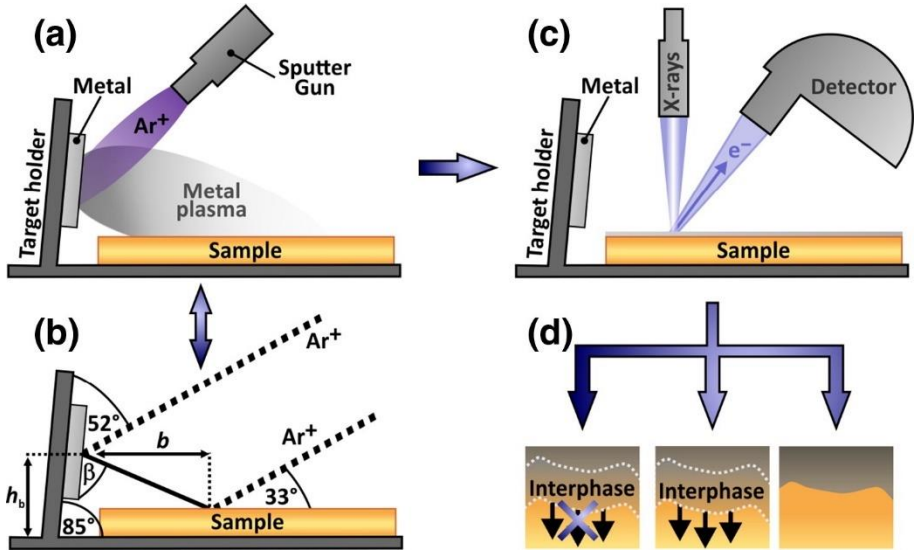

Figure 2-14 The *in-situ* characterization technique for solid electrolyte reaction interphase analysis[254].

MO et al.[255-259] calculated the chemical and electrochemical stability of a series of sulfide solid electrolyte-electrode interfaces by using density-functional theory of first-principle calculations. In the ternary sulfide solid electrolyte, the substitution of Ge^{4+} in LGPS by

hovalent or allovalent cations has little effect on improving the phase stability, electrochemical stability and conductivity of the solid electrolyte, while anion substitution has a great effect on its intrinsic performance. The conductivity decreasing attributes to the reducing of the lattice constant, while the increasing of lattice constant has a limited effect on the improvement of conductivity. The size of S^{2-} is close to the optimal value for the migration of lithium ions in the structural skeleton. The sulfide solid electrolyte possesses a narrow thermodynamically electrochemical window, the spontaneous chemical reaction occurs when contact with lithium metal, as a result Li_2S, Li_3P, Li-Ge alloys would be formed. A hybrid conductor interface is formed within the interface between Li and $Li_{10}GeP_2S_{12}$, and the resulting Li-Li_3PS_4 interface forms a kinetically stable solid electrolyte interface. The elimination of high-valent cations and the technology of hybrid anion utilization can improve the stability of the electrolyte when coupling with lithium metal. The results show that the good stability of the solid electrolyte is not attributed to the thermodynamic intrinsic properties, but corresponding to the kinetic stability. The slow decomposition reaction kinetics and poor electronic transportation in the interfacial layer are important issues to limit the kinetic stability. The calculation results also confirm that the decomposition and interface engineering of SEI film are

important problems to influence the performances of all-solid-state batteries. The interface layer can insulate electrons while conduct ions exhibits good interfacial stability and lower impedance. Artificial coating method is an effectively strategy to stabilize the interface and reduce the impedance of the interface.

2.3. Summary

In summary, compared with traditional lithium ion battery, all-solid-state batteries possess advanced safety performance and high energy density, have broad development potential in the fields of power using and energy storage. Lithium metal with low potential and high theoretical specific capacity, becomes the one of most ideal anode materials for solid-state batteries. Many sulfide solid electrolytes would spontaneously decompose when contact with metallic lithium, resulting in an increasing interfacial impedance and lithium consumption. A lithium-stable solid electrolyte, Li_6PS_5Cl, was introduced in this project as electrolyte to achieve long cycle life of the battery. On the other hand, the traditional Li-intercalation based transition metal oxide cathode material releases a low theoretical specific capacity, the high-resistance space charge layer exists in the contact within sulfide solid electrolytes, cannot meet the requirement of high-energy density solid-state batteries. The

transition metal sulfide not only exhibits a high theoretical specific capacity and moderate working voltage range, but also displays ideal interfacial compatibility between the sulfide solid electrolyte and cathode materials, become the one of the most promising electrode materials for achieving high energy density all-solid-state lithium batteries. Nevertheless, in transition metal sulfide cathode materials with anionic redox driven chemistry, sulfur fully or partially exists in the state of S_2^{2-} pairs, and this has a strong influence on specific capacity. For example, MoS_2 only has S^{2-} pairs, displaying a theoretical specific capacity of 670 mAh g^{-1}[190, 260]. MoS_3 has both S_2^{2-} and S^{2-} pairs, showing a higher theoretical specific capacity of 837 mAh g^{-1}[261]. A cathode material with large amount of S_2^{2-} pairs become candidate to realize high theoretical specific capacity. The transition metal sulfides were *in-situ* combined with solid electrolytes, forming a good ionic conductive network and structural framework, could not only improve the charge transport kinetics in the composite, but also enhance the structural stability during the charge-discharge process. However, the electrochemical performance of transition metal sulfides in all-solid-state batteries still need to be further improved, the electrochemical reaction and capacity decay mechanism of transition metal sulfides in all-solid-state batteries are still unclear as well. The purpose of this study is

the designing and improvement of MoS_6 material with various synthesis methods, and explore electrochemical properties when using in the all-solid-state batteries.

The research content of this thesis mainly includes the following aspects:

(1) Preparation and analysis of MoS_6 as a cathode material in all-solid-state lithium batteries.

Micro-size MoS_6 was prepared by aqueous solution reaction. MoS_6 has been considered as one of promising cathode materials for all-solid-state lithium battery because of its ultra-high theoretical specific capacity of 1117 mAh g^{-1} due to the high S_2^{2-} content as well as amorphous nature, which possess open and random transmission path to achieve cycling stability[262], therefore showing potential applications in high energy all-solid-state battery. *Ex-situ* XRD, HRTEM and XPS were used to analyze the reaction mechanism during the charge and discharge process.

(2) Preparation and analysis of MoS_6@15%$Li_7P_3S_{11}$ composite in all-solid-state lithium batteries.

By *in-situ* coating $Li_7P_3S_{11}$ solid electrolytes on the MoS_6, the resultant MoS_6@15%$Li_7P_3S_{11}$ composite can achieve an improved ion diffusion coefficient range. The Li/Li_6PS_5Cl/MoS_6@15%$Li_7P_3S_{11}$ all-solid-sate lithium batteries

show a high initial discharge capacity and long cycle life. Besides, the MoS_6@15%$Li_7P_3S_{11}$ composite displays a high energy density and power density. This contribution provides a new sulfide-based cathode material with high specific capacity and superior ion diffusion coefficient, showing promising application potential for all-solid-state lithium batteries.

(3) Preparation and analysis of 95MoS_6·5LiI composite in all-solid-state lithium batteries.

A transition metal sulfide composite 95MoS_6·5LiI with a superior electrochemical reaction kinetics was prepared by mechanical ball milling for all-solid-state lithium batteries. After cooperated LiI with MoS_6, the average ion diffusion coefficient was improved during the first cycle. The all-solid-state lithium batteries with 95MoS_6·5LiI exhibit high initial and reversible capacity. This work demonstrates a promising transition metal sulfide composite with high Li-ion transport kinetics, showing a new insight to improve the electrochemical performance for high-performance all-solid-state lithium batteries.

Chapter 3. Experiments

3.1. Materials preparation

3.1.1. MoS_6

3.1.1.1.. Introduction

Traditional sulfide cathode materials based on insertion reactions can accommodate lithium ions in their lattice without serious structural change during the intercalation/de-intercalation reaction of:

$$x\mathrm{Li}^+ + \mathrm{MS}_y + x\mathrm{e}^- \leftrightarrow \mathrm{Li}_x\mathrm{MS}_y \quad (14)$$

where M represents the transition metal. Although insertion reaction based cathode materials present stability and long cycle life performance when using in the all-solid-state lithium battery, they still have intrinsic problems related to the limit space for lithium ions, leading to a low specific capacity[172]. Nevertheless, for transition metal sulfide cathode materials with anionic redox driven chemistry (a-TiS_4[173], MoS_3[261] and FeS_2[179]), sulfur fully or partially exists in the state of S_2^{2-} pairs, which has a strong influence on specific capacity. For example, MoS_2 only has S^{2-}pairs, displaying a theoretical specific capacity of 670 mAh g^{-1}[190, 260]. MoS_3 has both S_2^{2-} and S^{2-} pairs, showing a higher theoretical specific

capacity of 837 mAh g^{-1}[261]. The electronic structure of the S_2^{2-} group allows them to donate or receive electrons. Their ability as donors is attributed to the π^*_g orbital, which can release electrons that convert S_2^{2-} to S^{2-}. Because of the reversible reaction of $S_2^{2-} + 2e^- \rightarrow 2S^{2-}$, multi-electron reactions proceed during charge/discharge process, resulting in a high specific capacity[172, 190]. In addition, transition metal sulfides with anionic redox driven chemistry display a high voltage plateau of about 2 V, which is close to that of lithium-sulfur batteries.

Although transition metal sulfides have numerous advantaged when using as cathode materials, the environmental concern of them is also an essential part. As an abundant and non-toxic material, transition metal sulfides show sustainable property compared with other rare materials used in battery systems. For example, they can be easily recycled and reducing the pollution for the environment. However, the synthesis of transition metal sulfides would involve hazardous chemicals and energy-intensive processes, which may have negative environmental impacts if not managed properly. The careful management is necessary to prevent the harm of environmental. Furthermore, the economic feasibility of using transition metal sulfides is also tied to the availability of the raw materials and the stability of the supply chain. The fluctuating prices

of transition metals can impact the cost of producing these sulfides, which in turn affects their economic viability.

3.1.1.2. Preparation of $(NH_4)_2Mo_2S_{12}$ precursor.

$(NH_4)_2Mo_2S_{12}$ was used as a precursor and synthesized by wet chemical methods. Briefly, 4.5 g of $(NH_4)_6Mo_7O_{24}{\cdot}4H_2O$ and 3 g of $NH_2OH{\cdot}HCl$ were dissolved in 60 ml of water (50 °C). 12 g of sulfur powder and 60 ml of $(NH_4)_2S$ (6−20 % aqueous solution) were mixed and stirred for 1 h. The above two solutions were mixed together and placed in the oven at 50 °C and 90 °C for 1 h and 4 h, respectively. After filtering, the filtrate was mixed with 20 ml of $(NH4)_2S$ and allowed to stand for 36 h, which were filtered and washed with water, ethanol carbon disulfide and diethyl ether.

3.1.1.3. Preparation of MoS_6

Micro-size MoS_6 was prepared by aqueous solution reaction corresponding to the reaction of:

$$(NH_4)_2Mo_2S_{12} + I_2 \rightarrow 2NH_4I + 2MoS_6 \qquad (15)$$

Typically, 0.28 g of $(NH_4)_2Mo_2S_{12}$ and 0.2 g of iodine were separately dissolved in *N*, *N*-dimethylformamide. Afterward, two solutions were thoroughly mixed together and kept stirring for 30 minutes. The obtained MoS_6 was filtered, washed with *N, N*-

dimethylformamide, CS_2, and acetone and finally dried and storage in argon atmosphere.

3.1.2. MoS_6 @ $Li_7P_3S_{11}$ composite

3.1.2.1. Introduction

Although the amorphous multi-sulfide active materials can shorten the transmission distance of lithium ions, and increase the theoretical specific capacity, the mixing of the active material and the solid electrolyte by manual grinding or mechanical ball milling cannot obtain an ideal solid-solid contact interface, resulting in the reducing of the reversible capacity due to some active materials cannot participate in the electrochemical reaction during the charge-discharge process. The lithium-ion transportation properties within interfacial contact between cathode and solid electrolyte are generally considered to be the essential part of the electrochemical reaction. In order to improve the interfacial contact between the active material and the solid electrolyte, so as to promote the charge transfer kinetics of lithium ions, the composite is formed by *in-situ* coating the solid electrolyte nanoparticles on the surface of active material, which can not only improve the solid-solid interface contact, shorten the transport path of lithium ions, but also further improve the rate and cycling performance of all-solid-state lithium batteries.

3.1.2.2. Preparation of MoS_6@15%$Li_7P_3S_{11}$ composite

A *in-situ* liquid phase reaction with annealing process were conducted for the MoS_6@15%$Li_7P_3S_{11}$ composite preparation[261]. In a typical process, the as-prepared MoS_6 were mixed with P_2S_5 and Li_2S powders, then magnetic stirring in anhydrous acetonitrile at 60 ^oC for 12 h. After removing the residual solvent, MoS_6 *in-situ* coated with $Li_7P_3S_{11}$ precursor was collected and then heated at 260 ^oC for about 1 h to obtain MoS_6@15%$Li_7P_3S_{11}$ composite.

The synthesis details of $Li_{10}GeP_2S_{12}$, Li_6PS_5Cl and 75%Li_2S-24%P_2S_5-1%P_2O_5 can be found elsewhere, the ionic conductivities of these solid electrolytes were 8.27×10^{-3} S cm^{-1} ($Li_{10}GeP_2S_{12}$), 3.5×10^{-3} S cm^{-1} (Li_6PS_5Cl) and 1.54×10^{-3} S cm^{-1} (75%Li_2S-24%P_2S_5-1%P_2O_5).

3.1.3. 95MoS_6·5LiI composite

3.1.3.1. Introduction

Due to the limited electrochemical reaction kinetics of MoS_6, the assembled all-solid-state lithium batteries suffered from low utilization of active materials during the charge-discharge process, leading to poor specific capacity and short lifespan[170, 260]. Recently, MoS_2@LiI-LiBr has been reported as a high

electrochemical reaction kinetics cathode material, which can enhance the ionic conductivity due to LiI-LiBr reduce the interaction between Li^+ and S^{2-}, as a result improve the utilization of active materials[263]. Therefore, doping LiI into MoS_6 is an effective strategy to improve the reversible capacity during the charge/discharge process[170].

3.1.3.2. Preparation of $95MoS_6 \cdot 5LiI$

To prepare the $95MoS_6 \cdot 5LiI$ (mol %) composites, a mixture of MoS_6 and LiI powders was placed into a ZrO_2 pot and then mechanically milled with a planetary ball mill for 9 h at 510 rpm in argon atmosphere.

3.2. Fabrication and evaluation of all-solid-state batteries

3.2.1. Battery assembling of MoS_6

3.2.1.1. All-solid-state lithium battery assembling

For electrochemical performance analysis of above-synthesized samples, the obtained MoS_6, $Li_{10}GeP_2S_{12}$ and Super P were mixed together at weight ratio of 40:50:10. For the preparation of $Li/Li_{10}GeP_2S_{12}/Li_6PS_5Cl/MoS_6$ all-solid-state batteries, upon cold pressing at 240 MPa, Li_6PS_5Cl (150 mg) solid electrolyte pellet

(ϕ=10 mm) can be fabricated. Then, the above-synthesized composites cathodes were homogeneously spread on the electrolyte surface and applied cold pressing again under 240 MPa. Finally, the metallic lithium foil (ϕ=10 mm) was attached to the other side of Li_6PS_5Cl layer with 360 MPa. For the purpose of comparison, the $Li/Li_{10}GeP_2S_{12}/75\%Li_2S\text{-}24\%P_2S_5\text{-}1\%P_2O_5/MoS_6$ all-solid-state batteries were fabricated as well. The bilayer pellets (ϕ=10 mm) consisting of $Li_{10}GeP_2S_{12}$ and orthorhombic phase $75\%Li_2S\text{-}24\%P_2S_5\text{-}1\%P_2O_5$ were constructed under 240 Mpa either. The above mentioned cathodes were spread on the side of $Li_{10}GeP_2S_{12}$ solid electrolytes homogeneously followed with 240 MPa cold pressing. The metallic lithium foil (ϕ=10 mm) was placed on the $75\%Li_2S\text{-}24\%P_2S_5\text{-}1\%P_2O_5$ solid electrolyte side by pressing them together under 360 MPa. The reason for bilayer solid electrolyte pellet is due to the instability between $Li_{10}GeP_2S_{12}$ and lithium metal. All the processes were operated in glove box with dry argon atmosphere.

3.2.1.2. Lithium-ion battery assembling

In order to analysis the electrochemical performances of MoS_6 when coupling with liquid electrolyte, the lithium-ion battery was assembled. Typically, 100 mg of MoS_6 was mixed with 28.6 mg of super P, and then 0.375 g of 4%PVDF was dropped into the powder

mixture. The mixture with 4%PVDF stirred with ball milling machine, black paint was generated. After applied the paint on the Aluminum foil and dried for 12 h, the cathode layer was successfully prepared. The coin cell composed by the cathode of MoS_6 cathode wafer, lithium metal, polyethylene separator film, and commercial electrolyte.

3.2.2. Battery assembling of MoS_6@15%$Li_7P_3S_{11}$ composite

The obtained MoS_6@15%$Li_7P_3S_{11}$ composite, $Li_{10}GeP_2S_{12}$ and Super P were mixed together with weight ratio of 40:50:10. For the preparation of Li/$Li_{10}GeP_2S_{12}$/Li_6PS_5Cl/MoS_6@15%$Li_7P_3S_{11}$ all-solid-state batteries, upon cold pressing at 240 MPa, Li_6PS_5Cl (150 mg) solid electrolyte pellet (ϕ=10 mm) can be fabricated. Then, the above-synthesized composite cathodes were homogeneously spread on the electrolyte surface and applied cold pressing again under 240 MPa. Finally, the metallic lithium foil (ϕ=10 mm) was attached to the other side of Li_6PS_5Cl layer with 360 MPa.

3.2.3. Battery assembling of 95MoS_6·5LiI composite

For the purpose of electrochemical performance evaluating, the as-synthesized MoS_6 or 95MoS_6·5LiI composite were mixed with $Li_{10}GeP_2S_{12}$ and Super P in mass ratio of 40:50:10. Afterward, 150

mg of Li_6PS_5Cl solid electrolytes were cold pressed into pellets under 240 MPa. Then, the above-mentioned composite cathodes were uniformly spread on the electrolyte surface and cold pressed under 240 MPa. Finally, a piece of lithium foil was placed on the other side of the solid electrolyte pellet by pressing them together under 360 MPa. All of the process were operated in argon atmosphere.

3.3. The electrochemical performances analysis of Battery

Galvanostatic charge and discharge tests were conducted on the multi-channel battery test system under various current densities with voltage range from 1.0 V to 3.0 V at room temperature. The galvanostatic intermittent titration technique (GITT) was tested under 1 A g^{-1} for 1 min followed by rest for 120 min. The Li ions diffusion coefficient (D) was determined by Eq. 16 based on the Fick's second law[264-267]:

$$D = \frac{4}{\pi\tau}\left(\frac{n_m v_m}{S}\right)^2 \left(\frac{\Delta E_s}{\Delta E_t}\right)^2 \quad (16)$$

Where τ is the time duration of the pulse, n_m and v_m are the molar mass (mol) and volume (cm^3/mol) of the active material, respectively. S is the cell interfacial area, ΔE_s and ΔE_t are voltage drops of the pulse and discharge process[268].

The electrochemical work station (Solartron 1470E) was employed for cyclic voltammetry (CV) measurements and

electrochemical impedance spectroscopy (EIS). All measurements were proceeded under room temperature.

3.4. Materials characterization

X-ray diffractions (XRD) measurements were performed on Bruker D8 Advance Davinci with Cu *K*α radiation of λ = 1.54178 Å in a 2θ range of 10–60^{o} to determine the crystal structure of samples. Raman spectra results were recorded in the range of 250 to 580 cm^{-1} by Raman spectrophotometer (Renishaw inVia Reflex) with 532 nm laser. The atom ratio of MoS_6 was analyzed by the inductively coupled plasma emission spectrometer analysis (ICP-OES, Spectro Arcos, Spectro). Field emission scanning electron microscopy (SEM, S-4800, Hitachi) and Field emission scanning electron microscopy energy dispersive spectroscopy (SEM-EDS) were conducted to confirm the morphology, particle size and elements distribution. High-resolution transmission electron microscopy (HRTEM) was conducted on FEI Tecnai F20 for the existence of $Li_7P_3S_{11}$ solid sulfide electrolyte thin layer coated on the MoS_6 surface. X-ray photoelectron spectroscopy (XPS, Axis Supra, Kratos) is used for energy bonding detection. The sample cross-sections used for mechanism analysis were performed on focused-ion-beam (FIB, Helios-G4-CX, Thermo scientific).

3.4.1. X-ray diffractions (XRD)

X-ray diffraction (XRD) is a powerful analytical technique employed extensively in the field of materials science, chemistry, physics, and geology for the characterization of crystalline materials. The core functionality of XRD revolves around the investigation of the internal atomic structure and arrangement within a substance by exploiting the diffraction phenomenon that occurs when a monochromatic X-ray beam interacts with a crystalline lattice.

When X-rays encounter the orderly array of atoms in a crystal, they undergo scattering events governed by Bragg's Law. The scattered waves interfere constructively at specific angles (Bragg angles), producing intense peaks on a detector, which are collectively referred to as the diffraction pattern or diffractogram. Each peak corresponds to a set of interatomic spacings (*d*-spacings) and crystallographic planes within the material.

Key functionalities of XRD include:

(1) Phase Identification: By comparing the observed diffraction patterns against reference databases, XRD enables the identification of the crystalline phases present in a sample, thus determining its chemical composition and mineralogy.

(2) Crystal Structure Analysis: Detailed analysis of the intensities and positions of diffraction peaks allows for the

determination of unit cell parameters (lattice constants), space groups, and atomic positions within the crystal lattice.

(3) Texture Analysis: The preferred orientation of crystals in a polycrystalline material (texture) can be quantified using XRD techniques.

(4) Structural Studies: In-depth studies of crystal structures can reveal changes in bonding environments, oxidation states, or complex structural transformations under varying conditions such as temperature, pressure, or composition.

Overall, XRD provides invaluable information about the fundamental nature of solids, including their composition, crystal structure, microstructure, and preferred orientations, making it an indispensable tool in both research and industrial quality control settings.

3.4.2. Raman spectrophotometer

Raman spectroscopy instrument serves as a versatile analytical tool widely utilized in various scientific disciplines for non-destructive identification and characterization of materials. The primary function of a Raman spectrometer involves probing the vibrational, rotational, and other low-frequency modes of molecules within a sample through the inelastic scattering of light.

Raman spectroscopy is based on the Raman effect, where incident monochromatic light, often from a laser source, interacts with the molecular bonds within a substance. When this light is scattered by the molecules, most of it scatters elastically, corresponding to the well-known Rayleigh scattering. However, a small fraction (approximately 1 in 10^{-6} to 10^{-8} photons) scatter inelastically, gaining or losing energy during the process. This shift in energy corresponds to the vibrational transitions occurring within the molecule and results in a unique spectral fingerprint for each material.

The main functions of a Raman spectrometer include:

(1) Molecular Identification: By analyzing the Raman spectrum, which displays peaks corresponding to the vibrational frequencies of the molecules, one can identify the chemical composition and functional groups present in a sample. This is particularly useful for organic and inorganic compounds, pharmaceuticals, biological tissues, and minerals.

(2) Structural Analysis: Raman spectroscopy reveals information about the molecular structure, including conformational isomers, polymorphs, and the presence of defects in crystalline materials. It can also detect subtle changes in molecular geometry and bond lengths.

(3) Low Concentration Detection: With advancements in instrumentation, such as near-infrared lasers and surface-enhanced Raman spectroscopy (SERS), it is possible to detect trace amounts of substances even down to single-molecule detection levels.

(4) Temperature and Pressure Dependent Studies: Raman spectroscopy can be performed under controlled environmental conditions, allowing for real-time monitoring of molecular changes during reactions or under variable stressors.

3.4.3. Inductively coupled plasma emission spectrometer analysis (ICP-OES)

Inductively Coupled Plasma Optical Emission Spectrometry (ICP-OES) is a highly sensitive and accurate analytical technique employed for the qualitative and quantitative determination of a wide range of elements in various sample matrices. This advanced method combines the principles of plasma physics with optical emission spectroscopy to deliver rapid, multi-element analysis with exceptional precision and reproducibility.

In an ICP-OES system, a sample is introduced into a high-temperature plasma generated by an inductively coupled radiofrequency (RF) field. The plasma torch, operating at temperatures exceeding 6000 °C, effectively atomizes and ionizes the

sample components, converting them into excited atomic and ionic species. Upon returning to their ground state, these species emit characteristic wavelengths of light, which are detected and measured by a high-resolution optical spectrometer.

The primary functions and advantages of ICP-OES include:

(1) Elemental Analysis: Capable of detecting nearly all elements in the periodic table, from alkali metals to transition metals, rare earth elements, and several non-metals, ICP-OES allows for the simultaneous determination of multiple elements at concentrations ranging from parts per million (ppm) to parts per billion (ppb).

(2) Broad Dynamic Range: It has a large linear dynamic range, meaning it can quantify elements over several orders of magnitude without significant loss of precision.

(3) Accuracy and Precision: Due to the inherent stability of the plasma and the use of external calibration standards, ICP-OES provides reliable and repeatable measurements with low detection limits.

(4) Trace Element Detection: The sensitivity of ICP-OES is particularly advantageous for detecting trace elements, which may be critical for regulatory compliance, quality control, or research purposes.

3.4.4. Field emission scanning electron microscopy (SEM)

In this work, secondary electrons (SEs) were used to scan surfaces of samples to obtain information. In SEM, secondary electrons (SEs) play a pivotal role in imaging and surface analysis. Secondary electrons are generated as a result of the interaction between the primary electron beam and the sample material. When the high-energy incident electrons impinge upon the specimen surface, they can cause atoms within the material to become excited or ionized, leading to the ejection of electrons that were originally bound to those atoms. These ejected electrons are known as secondary electrons and typically carry much lower energies than the primary electrons.

The key feature of secondary electrons in SEM applications is their sensitivity to the topographical details at the surface of the specimen. Due to their low kinetic energy and short escape depth, SEs are predominantly emitted from close to the surface, providing information about surface topology with excellent resolution and contrast. This makes them particularly useful for creating high-resolution images that reveal intricate surface features such as texture, roughness, and morphology.

Secondary electron detectors in an SEM are designed to capture these low-energy electrons effectively. By raster-scanning the

focused primary electron beam across the sample and continuously collecting the secondary electrons emitted, a detailed topographic image is constructed. The resulting SEM images display a strong signal intensity variation with respect to surface inclination, which enhances the three-dimensional appearance of the imaged structures.

In summary, the secondary electron imaging mode in a scanning electron microscope is crucial for visualizing and characterizing the microstructure and surface properties of various materials in fields ranging from materials science and engineering to biology and geology. It offers a non-destructive method for obtaining highly-detailed, high-contrast images that provide valuable insights into the surface characteristics of specimens.

3.4.5. SEM-energy dispersive spectroscopy

Scanning Electron Microscopy coupled with Energy Dispersive Spectroscopy (SEM-EDS) is a powerful combination of analytical tools that provides both morphological and elemental compositional information about a sample.

Energy Dispersive Spectroscopy (EDS) is an accessory attached to the SEM that analyzes the X-ray emissions produced by the sample when it is bombarded by the electron beam. When high-energy electrons from the SEM penetrate the material, they can

dislodge inner shell electrons from the atoms, causing the higher energy outer shell electrons to drop down and fill the vacancies. In doing so, characteristic X-rays are emitted, each with a specific energy level that is unique to the element from which they originated.

The EDS detector captures these X-rays and measures their energy, thereby identifying and quantifying the elemental composition of the sample. This information is displayed as an elemental map or spectrum, providing a semi-quantitative or quantitative distribution of elements across the scanned area. Consequently, SEM-EDS not only gives insight into the sample's morphology but also its chemical makeup, allowing for comprehensive material characterization.

As a practical characterization technique, SEM-EDS can perform elemental analyses at micron or even submicron scales, facilitating diverse applications in materials science, geology, forensics, biology, semiconductor technology, and many other fields to understand the relationship between microstructure and composition.

3.4.6. High-resolution transmission electron microscopy (HRTEM)

High Resolution Transmission Electron Microscopy (HRTEM)

is an analytical technique in the field of materials science and nanotechnology that delivers ultra-high resolution imaging of materials at the atomic scale. HRTEM works by utilizing a highly focused beam of electrons transmitted through an extremely thin specimen, typically less than 100 nm and often below 1 nm thick, to create detailed images of the internal structure of materials.

The principal function of HRTEM based on its ability to resolve the arrangement of atoms within a crystalline lattice. As the electrons pass through the specimen, they interact with the periodic potential of the crystal, leading to interference patterns that form the basis of the image. The high resolving power of HRTEM instruments allows for the visualization of individual lattice fringes, which correspond to the distances between adjacent crystal planes, thereby providing precise information about the crystal structure and orientation.

Additionally, HRTEM can reveal defect structures, such as dislocations, grain boundaries, and interfaces, which are critical in understanding material properties and behavior. Moreover, it can produce Fourier transforms of the images, which can be analyzed to determine crystal structures directly from the diffraction patterns. Furthermore, advanced HRTEM setups can incorporate exit wave reconstruction techniques and other computational algorithms to enhance the interpretability of the acquired data.

Another important aspect of HRTEM is its compatibility with other TEM-based techniques like Selected Area Electron Diffraction (SAED), which enable further characterization of the chemical composition, electronic structure, and bonding environments within the material.

3.4.7. Time-of-Flight Secondary Ion Mass Spectroscopy (TOF-SIMS)

Time-of-Flight Secondary Ion Mass Spectrometry (TOF-SIMS) is a sophisticated surface analysis technique that provides high-resolution chemical information about the topmost layers of a sample. It is widely recognized for its ability to detect a vast array of elements and molecular species, even in complex mixtures, with exceptional sensitivity and spatial resolution.

Key features of TOF-SIMS include:

(1) High Sensitivity: TOF-SIMS can detect trace elements and impurities at concentrations as low as parts per billion (ppb) or even parts per trillion (ppt), making it an excellent tool for quality control and failure analysis.

(2) High Mass Resolution: The technique offers high mass resolution, allowing for the differentiation between isotopes and closely related molecular species, which is crucial for complex

sample analysis.

(3) Depth Profiling: By varying the sputtering conditions, TOF-SIMS can be used to create depth profiles of the sample, providing information about the composition as a function of depth.

Chapter 4. MoS_6[1]

4.1. Characterization results of MoS_6

To better demonstrate the property of as-prepared samples, the characterization techniques were revealed. The as-prepared $(NH_4)_2Mo_2S_{12}$ display a crystal structure, which matched well with standard peaks in the PDF card (JCPDS: F73-0900)(Figure 4-1)[269].

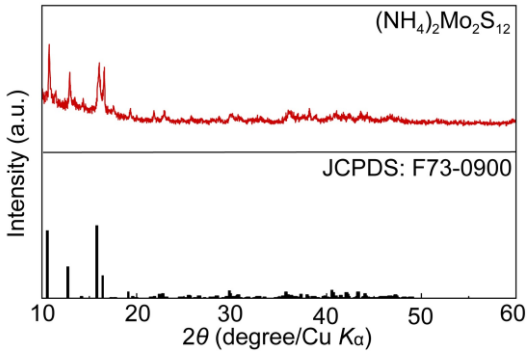

Figure 4-1 XRD pattern of $(NH_4)_2Mo_2S_{12}$.

Micro-size MoS_6 was prepared by aqueous solution reaction with $(NH_4)_2Mo_2S_{12}$, showing an amorphous structure (Figure 4-2).

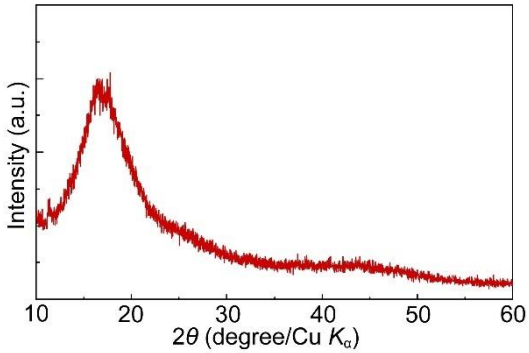

Figure 4-2 XRD pattern of MoS_6.

[1] The data used in this chapter have been published by Mingyuan Chang as first author in journal of Batteries named "Micro-sized MoS_6@ 15% $Li_7P_3S_{11}$ composite enables stable all-solid-state battery with high capacity. Batteries, **2023**, 9(11): 560."

To better demonstrate the property of as-prepared sample, the Mo/S atom ratio was measured by inductively coupled plasma emission spectrometer (Table 4-1). The actual remaining weight ratio of Mo and S were 31.5 wt.% and 63.5 wt.%, indicating Mo/S ratio is 6.036, which in agreement with the theoretical value of 6.

Table 4-1 The inductively coupled plasma emission spectrometer analysis of MoS_6.

Elements	S	Mo
Weight %	63.5	31.5
Atom %	85.7	14.2

In order to confirm the bonds in MoS_6, Raman spectroscopy was performed (Figure 4-3). The peaks located at the range of 286–385cm^{-1} and 518–550 cm^{-1} correspond to vibrations of molybdenum sulfide bonds and bridging disulfide/terminal disulfide[26, 27].

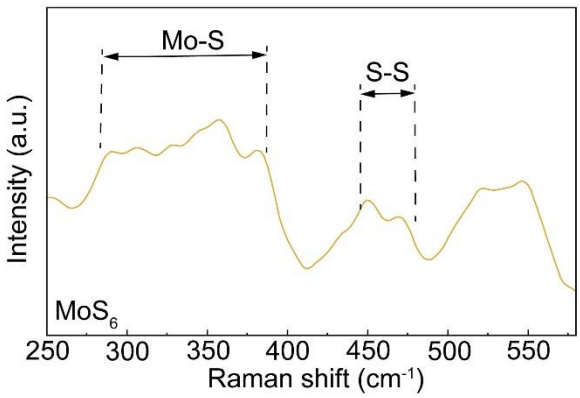

Figure 4-3 Raman spectra of MoS_6.

The morphology and microstructure of MoS_6 was observed by

SEM and HRTEM (Figure 4-4). The particle size for MoS_6 is in the range of 1–4 μm (Figure 4-4a). HRTEM images further confirm the amorphous nature of MoS_6 (Figure 4-4b), which is well matched with the result of SAED rings shown in Figure 4-4c.

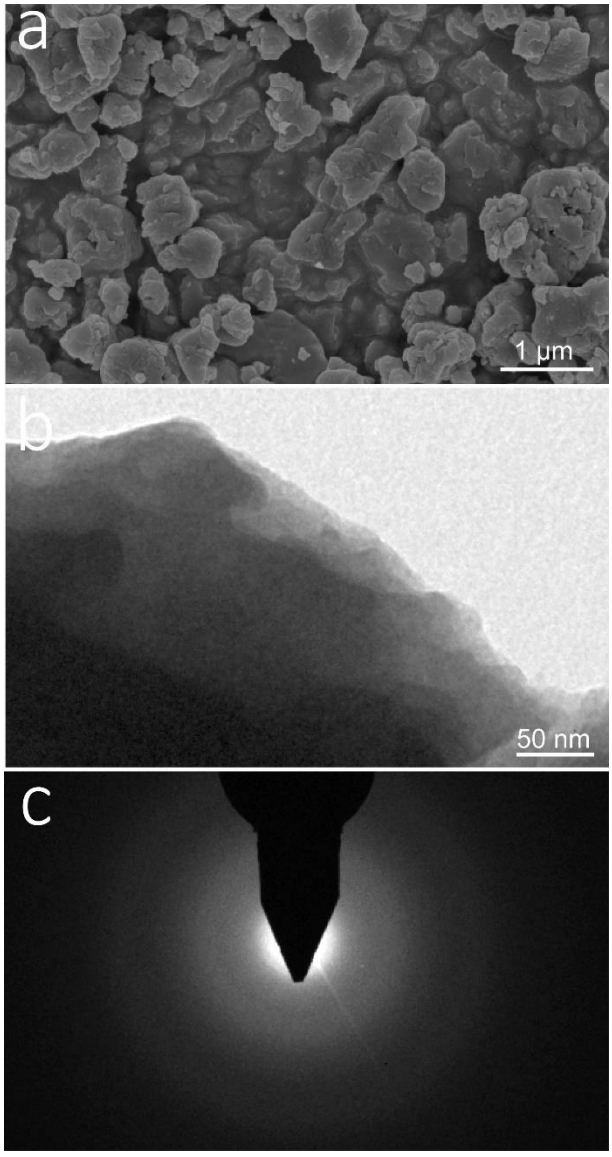

Figure 4-4 SEM image of (a) MoS_6. TEM image of (b) MoS_6 as well as SAED image of (c) MoS_6.

To guarantee the uniformity of the characterization results, the SEM and TEM figures of MoS_6-2 and MoS_6-3 are shown in Figure

4-5. Both of them display the particle size range of 1–4 μm, and show the amorphous structure in TEM figures, which are well matched with MoS_6 in Figure 4-4.

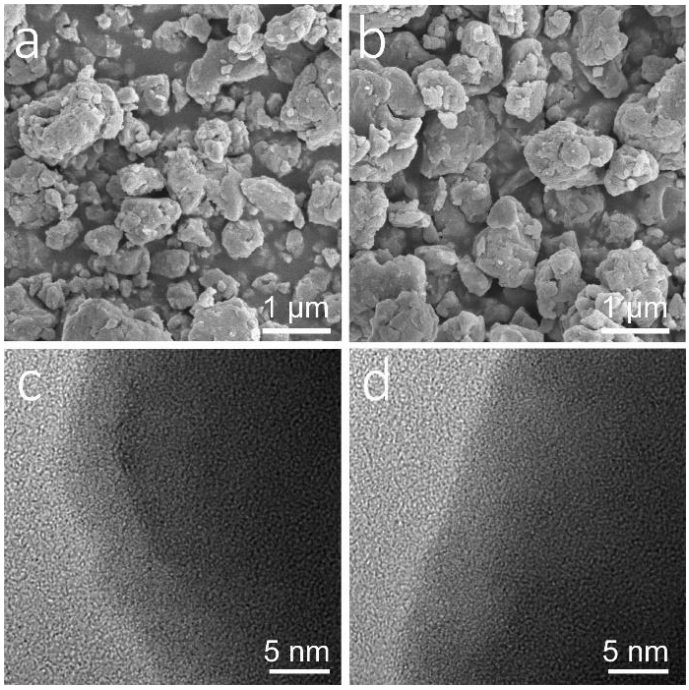

Figure 4-5 SEM images of (a) MoS_6-2 and (b) MoS_6-3. TEM images of (c) MoS_6-2 and (d) MoS_6-3.

4.2. Electrochemical performances of MoS_6

The electrochemical performances of MoS_6 were tested in all-solid-state lithium batteries, where two type battery configures were employed at 25 °C under 0.2 A g^{-1}, i.e. $Li/Li_6PS_5Cl/MoS_6$ and $Li/Li_{10}GeP_2S_{12}/75\%Li_2S\text{-}24\%P_2S_5\text{-}1\%P_2O_5/MoS_6$ all-solid-state batteries. As shown in Figure 4-6, $Li/Li_6PS_5Cl/MoS_6$ all-solid-state battery exhibits a reversible specific capacity of 361.8 mAh g^{-1} after 200 cycles, which is higher than the value of 78.3 mAh g^{-1} for

Li/$Li_{10}GeP_2S_{12}$/75%Li_2S-24%P_2S_5-1%P_2O_5/MoS_6 all-solid-state battery, showing a better capacity retention.

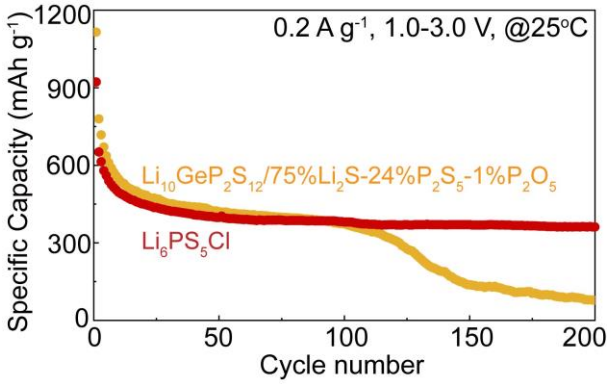

Figure 4-6 Cyclic performances of Li/Li_6PS_5Cl/MoS_6 and Li/ $Li_{10}GeP_2S_{12}$/75%Li_2S-24%P_2S_5-1%P_2O_5/MoS_6 all-solid-state batteries under 0.2 A g^{-1}.

For the purpose of comparison, cyclic performances of 50MoS_6: 50$Li_{10}GeP_2S_{12}$, 40MoS_6: 50$Li_{10}GeP_2S_{12}$: 10Super P and 40MoS_6: 40$Li_{10}GeP_2S_{12}$: 20Super P were performed under 0.1 A g^{-1} at 25 °C to determine the appropriate mixing ratio, as shown in Figure 4-7. The discharge capacity of 40MoS_6: 50$Li_{10}GeP_2S_{12}$: 10Super P was 544.8 mAh g^{-1} after 10 cycles, which is higher than 394.69 mAh g^{-1} and 438.29 mAh g^{-1} for 50MoS_6: 50$Li_{10}GeP_2S_{12}$ and 40MoS_6: 40$Li_{10}GeP_2S_{12}$: 20Super P, respectively, showing a high reversible discharge capacity.

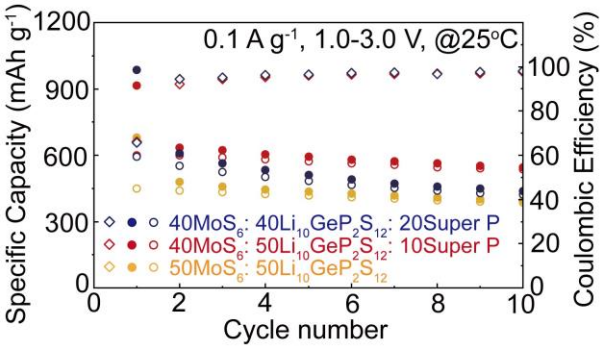

Figure 4-7 Cyclic performances of all-solid-state batteries with $50MoS_6$: $50Li_{10}GeP_2S_{12}$, $40MoS_6$: $50Li_{10}GeP_2S_{12}$: 10Super P and $40MoS_6$: $40Li_{10}GeP_2S_{12}$: 20Super P cathodes under 0.1 A g^{-1}.

To reveal the electrochemical reaction mechanism of MoS_6, CV curves of Li/Li_6PS_5Cl/MoS_6 all-solid-state batteries were performed for the first three cycles, as shown in Figure 4-8a. During the first cathodic scan, reduction peak at around 1.75 V can be attribute to the lithiation process of MoS_6 and further conversion process. During the initial anodic scanning period, the oxidation peak at 2.25 V corresponds to the de-lithiation processes and the formation of molybdenum sulfides[200, 270]. Clearly, the redox reactions of MoS_6 occur within the potential window of 1.0–3.0 V, which was selected to further evaluate electrochemical performances. Figure 4-8b present the first three cycles galvanostatic discharge-charge curves of MoS_6 and MoS_6@15% $Li_7P_3S_{11}$ composites in all-solid-state lithium batteries under 0.1 A g^{-1} at 25 °C. The all-solid-sate lithium battery with MoS_6 cathodes deliver high initial discharge capacities of 913.9 mAh g^{-1}.

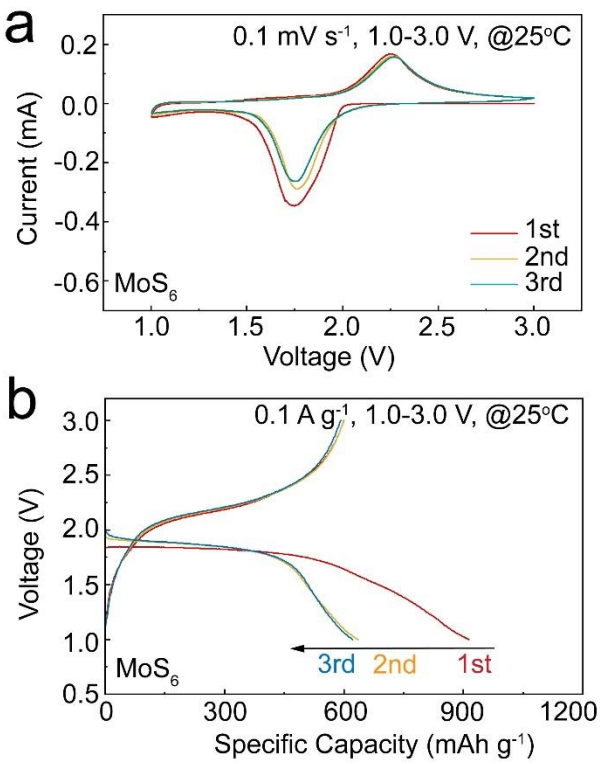

Figure 4-8 CV curves of (a) MoS_6. Galvanostatic discharge/charge profiles of (b) MoS_6 cathodes under the current density of 0.1 A g^{-1}.

To guarantee the reproducibility of electrochemical performances, the initial discharge specific capacity of MoS_6-1, MoS_6-2 and MoS_6-3 under the current density of 0.1 A g^{-1} are shown in Table 4-2. All of them display the similar performance, demonstrating the reproducibility of the data. As shown in the Figure 4-9, the error bar was also derived from the capacity data of MoS_6, MoS_6@15%$Li_7P_3S_{11}$ and MoS_6·5LiI. The small error range can co-confirm the reproducibility of samples.

Table 4-2 The specific capacity comparison of MoS_6-1, MoS_6-2 and MoS_6-3 under the current density of 0.1 A g^{-1}.

Sample No.	Current density (A g^{-1})	Specific capacity (mAh g^{-1})
MoS_6-1	0.1	913.9
MoS_6-2	0.1	916.9
MoS_6-3	0.1	903.9

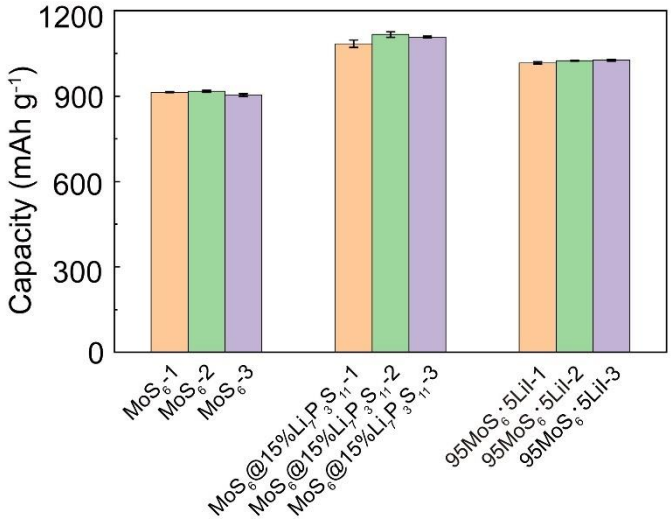

Figure 4-9 The capacity data and error range of MoS_6, MoS_6@15%$Li_7P_3S_{11}$ and MoS_6·5LiI.

For comparison, the liquid electrolyte based battery with MoS_6 cathode material was assembled and tested as well. The galvanostatic discharge/charge profiles of Li/Li_6PS_5Cl/MoS_6 and Li/commercial liquid electrolyte (matched with NMC811 cathode)/MoS_6 are shown in Figure 4-10. The shape of voltage curve and plateau location of the battery using liquid electrolyte is roughly same with those of the

all-solid-state battery. However, due to the shuttle effect[271-274], the initial discharge capacity of Li/commercial liquid electrolyte/MoS_6 is 812.43 mAh g^{-1}, which is lower than 913.9 mAh g^{-1} of the Li/Li_6PS_5Cl/MoS_6 battery. After 3 cycles, the discharge capacity of Li/commercial liquid electrolyte/MoS_6 decreases to 395.93 mAh g^{-1} (622.3 mAh g^{-1} for Li/Li_6PS_5Cl/MoS_6). As a result, the Li/Li_6PS_5Cl/MoS_6 system is chosen for further analysis works.

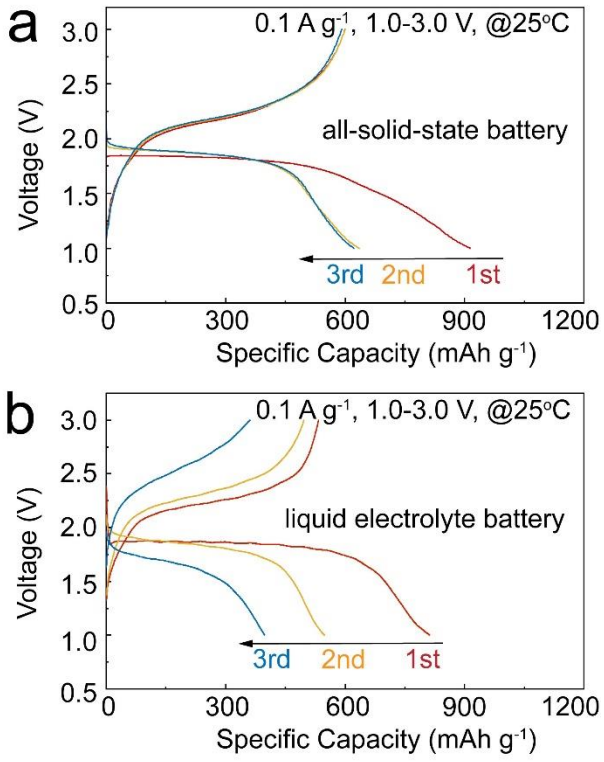

Figure 4-10 Galvanostatic discharge/charge profiles of (a) Li/Li_6PS_5Cl/MoS_6 and (b) Li/commercial liquid electrolyte/MoS_6 under the current density of 0.1 A g^{-1}.

To explore the principle of cathode kinetics and capacity variation for Li/Li_6PS_5Cl/MoS_6 all-solid-state lithium battery, EIS was conducted with the amplitude of 15 mV from 10^6 to 0.1 Hz. The

corresponding equivalent circuit model is shown in the Figure 4-11, where R_e is the resistance of the electrolyte, semicircle shows the interfacial charge transfer resistance (R_{ct}) emerges, the constant phase angle element (*CPE*) is used to indicate the behavior of non-ideal capacitance of the double-layer, and Z_w represents the Warburg resistance, which indicating the lithium ions diffuse into the bulk electrodes[200, 270]. The fitted results of R_e and R_{ct} are listed in Table 4-3.

Table 4-3 EIS fitting results of MoS_6 and MoS_6@15%$Li_7P_3S_{11}$ under 0.1 A g^{-1} after 20 cycles.

Cathode materials	1st cycle		20th cycle	
	R_e (Ω)	R_{ct} (Ω)	R_e (Ω)	R_{ct} (Ω)
MoS_6	105.42	/	384.11	52.96

After the first cycle, the EIS plot is straight line. MoS_6 exhibits a R_e value of 105.42 Ω. After 20 cycles, MoS_6 delivers R_e value of 384.11 Ω and R_{ct} value of 52.96 Ω.

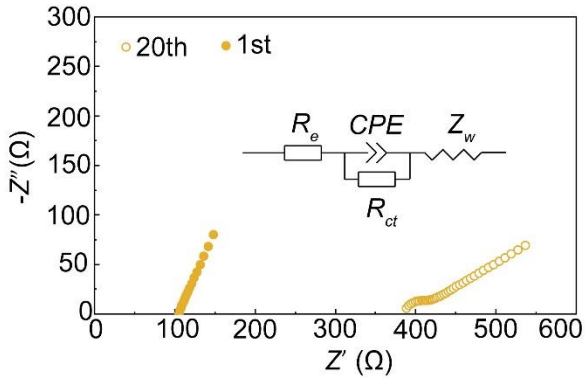

Figure 4-11 Nyquist plots and the equivalent circuit diagram of MoS_6 and MoS_6@15%$Li_7P_3S_{11}$ composite cathodes after 1st and 20th cycles at 0.1 A g^{-1} within1.0–3.0 V.

The rate capabilities of MoS_6 cathode were performed under various current densities from 0.1 to 2 A g^{-1} (Figure 4-12a). MoS_6 cathode exhibited superior reversible discharge capacities of 683.9, 516.8, 407.7, 326.2 and 255.8 mAh g^{-1} under current densities of 0.1, 0.2, 0.5, 1 and 2 A g^{-1}, respectively. The rate capability of MoS_6 can be further enhanced, which lead to improved electrochemical reaction kinetics. As shown in Figure 4-12b, the Ragone plot gives the relationship between the average power density and energy density. Under current density of 0.1 and 2.0 A g^{-1}, the MoS_6 cathodes deliver energy and power densities of 495.8 Wh kg^{-1} and 1332.2 W kg^{-1} based on the total cathode layer composed of MoS_6, $Li_{10}GeP_2S_{12}$ and super P.

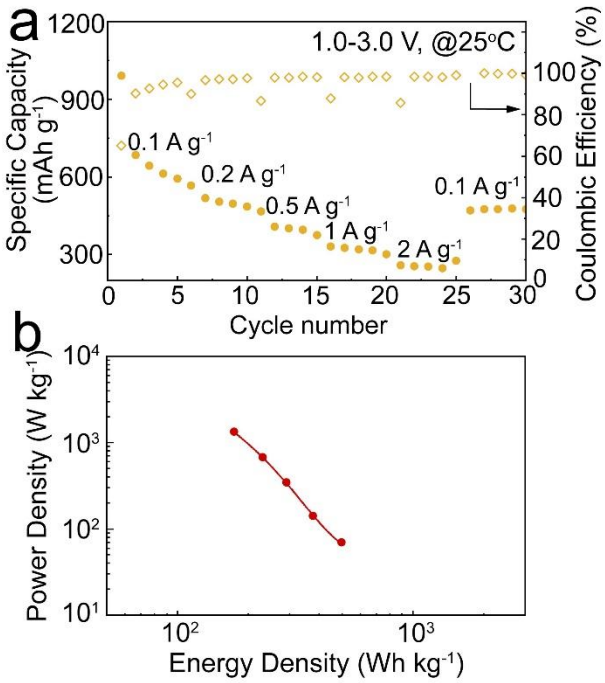

Figure 4-12 (a) Rate performances of MoS_6 under different current densities. (b) Ragone plot deduced from the rate performances in (a).

The long-term cycling stability of MoS_6 under 1 A g^{-1} is further shown in Figure 4-13. After activation at 0.1 A g^{-1} for the first 5 cycles, the MoS_6 rapidly decay for the first 100 cycles and decreases to 0 mAh g^{-1} after 500 cycles at 1 A g^{-1}. The limited reversible capacity and bad cyclic performances are mainly ascribed to the poor interfacial contact and structural instability[261, 275].

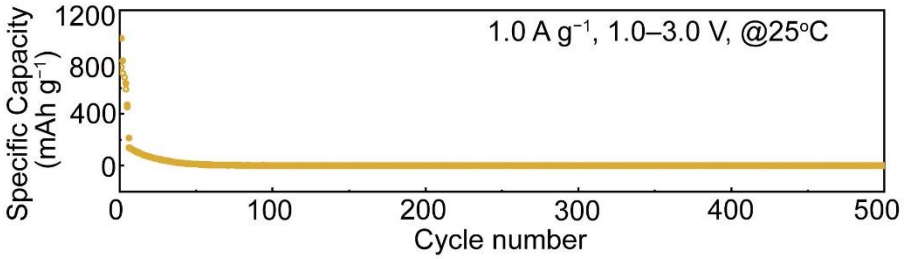

Figure 4-13 Long-term cyclic performance of MoS_6 under 1 A g^{-1}.

MoS_6 has been considered as one of promising cathode materials for all-solid-state lithium battery because of its ultra-high theoretical specific capacity of 1117 mAh g^{-1} due to the high S_2^{2-} content as well as amorphous nature, which possess open and random transmission path to achieve cycling stability, therefore showing potential applications in high energy all-solid-state battery. However, the challenges such as poor contact between the cathode and electrolyte, limited ionic transport kinetics and low electrochemical reaction kinetics lead to an unappealing Coulombic efficiency and poor rate performances, resulting in reversible specific capacity of 635.1 mAh g^{-1}. Further strategies are employed in following chapters to obtain MoS_6@15%$Li_7P_3S_{11}$ and 95MoS_6·5LiI, which can provide intimate contact within the cathode and electrolyte, improved ionic transport kinetics and high electrochemical reaction kinetics.

Chapter 5. MoS_6@15%$Li_7P_3S_{11}$[2]

5.1. Characterization results of MoS_6@15% $Li_7P_3S_{11}$

To better demonstrate the property of as-prepared sample, the synthesis procedures of MoS_6@15%$Li_7P_3S_{11}$ composite are schematically illustrated in Figure 5-1. $Li_7P_3S_{11}$ solid electrolyte precursor was *in-situ* coated on the MoS_6 surface during the facile liquid phase deposition method. After the 260 °C annealing treatment, MoS_6@15%$Li_7P_3S_{11}$ composite was successfully prepared.

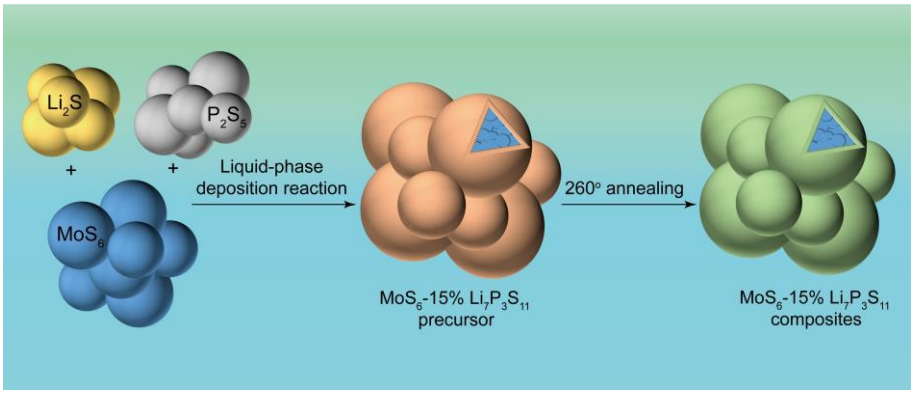

Figure 5-1. Schematic diagram of preparation procedure for MoS_6@15%$Li_7P_3S_{11}$ composite.

XRD patterns of MoS_6 and MoS_6@15%$Li_7P_3S_{11}$ composite are shown in Figure 5-2, confirming amorphous nature of MoS_6. No characteristic peaks for $Li_7P_3S_{11}$ sulfide electrolyte were detected, indicating the low coating amount of $Li_7P_3S_{11}$ sulfide electrolyte.

[2] The data used in this chapter have been published by Mingyuan Chang as first author in journal of Batteries named "Micro-sized MoS_6@ 15% $Li_7P_3S_{11}$ composite enables stable all-solid-state battery with high capacity. Batteries, **2023**, 9(11): 560.".

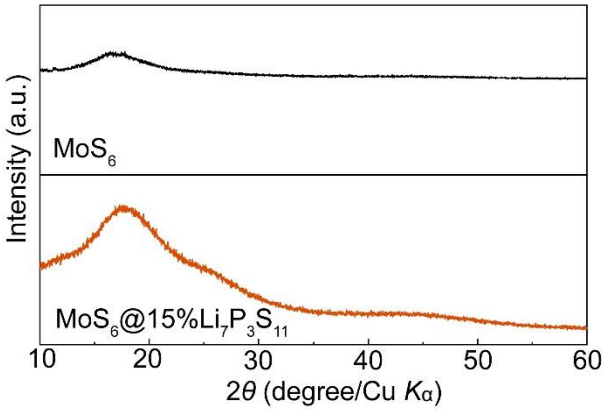

Figure 5-2 XRD patterns of MoS_6 and MoS_6@15%$Li_7P_3S_{11}$ composite.

In order to confirm the existence of $Li_7P_3S_{11}$ sulfide solid electrolyte in MoS_6@15%$Li_7P_3S_{11}$ composite, Raman spectroscopy was performed (Figure 5-3). The peaks located at the range of 286–385cm^{-1} and 518–550 cm^{-1} correspond to vibrations of molybdenum sulfide bonds and bridging disulfide/terminal disulfide[276, 277]. Furthermore, the peak located at 421cm^{-1} can be attributed to the PS_4^{3-} in $Li_7P_3S_{11}$ sulfide solid electrolyte[200].

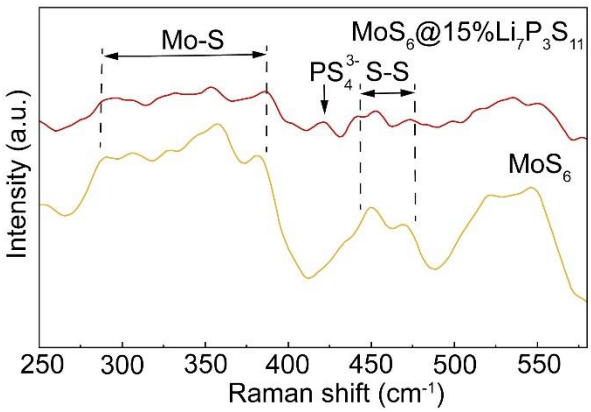

Figure 5-3 Raman spectra of MoS_6 and MoS_6@15%$Li_7P_3S_{11}$ composite.

The microstructures of MoS_6 and MoS_6@15%$Li_7P_3S_{11}$ composites were observed by SEM (Figure 5-4). The particle sizes for MoS_6 and MoS_6@15%$Li_7P_3S_{11}$ composite are in the range of 1-4μm.

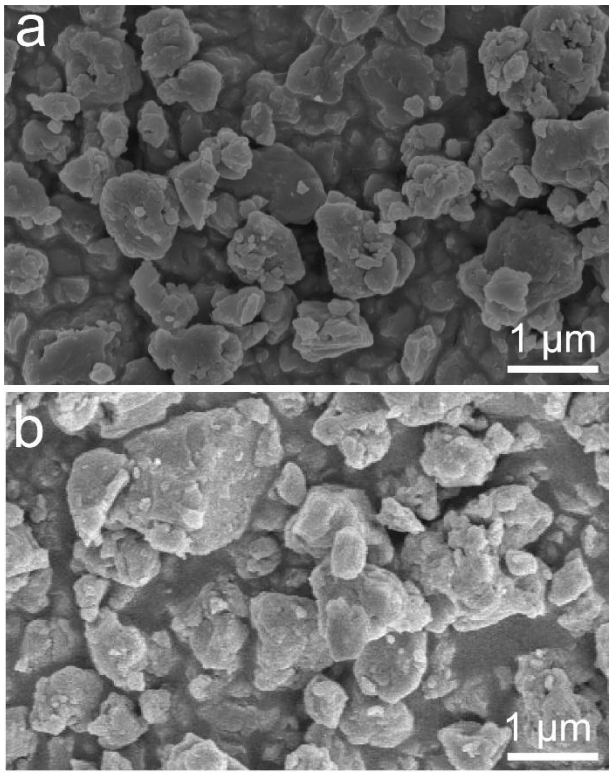

Figure 5-4 SEM images of (a) MoS_6 and (b) MoS_6@15% $Li_7P_3S_{11}$.

EDS mapping of MoS_6@15%$Li_7P_3S_{11}$ composite clearly illustrate the well distribution of molybdenum (blue), phosphorus (purple) and sulfur (yellow) (Figure 5-5).

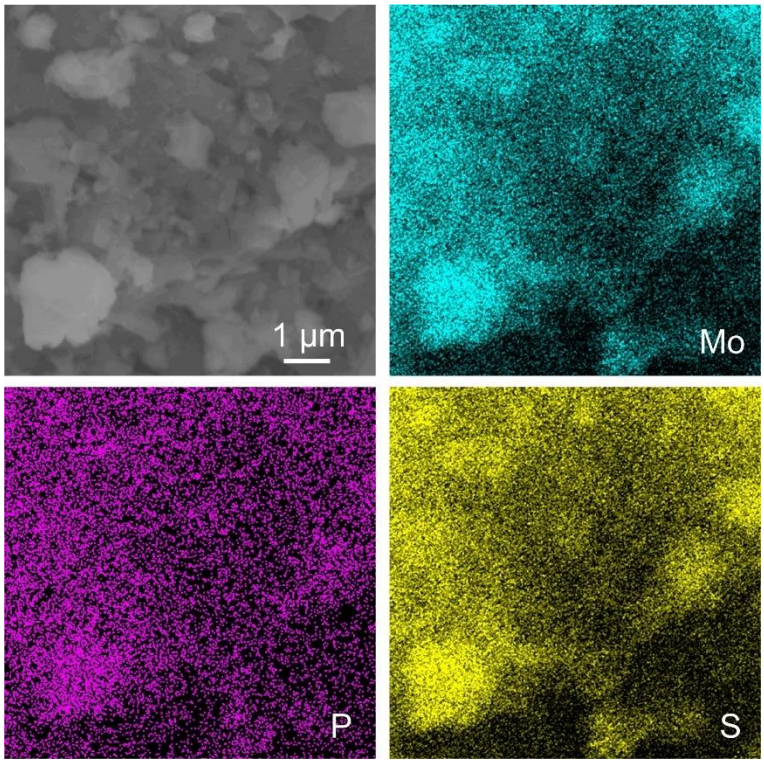

Figure 5-5 EDS mapping of MoS_6@15%$Li_7P_3S_{11}$ composite.

HRTEM images further confirm that $Li_7P_3S_{11}$ solid electrolytes uniformly grow on the surface of MoS_6 (Figure 5-6), which facilitates ionic transport and creates intimate interfacial contact.

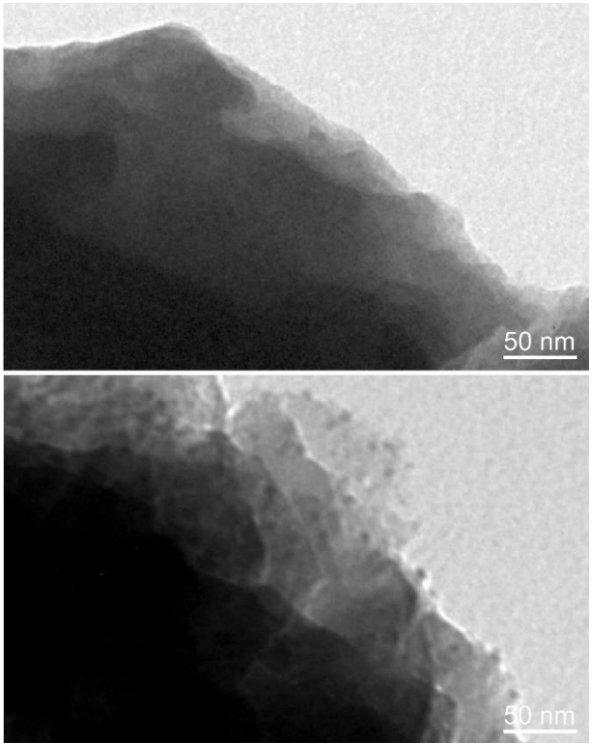

Figure 5-6 TEM images of (a) MoS_6 and (b) MoS_6@15% $Li_7P_3S_{11}$.

As shown in Figure 5-7, the *d*-spacings of 0.38, 0.35 and 0.309 nm correspond to the d_{030}, d_{202}, and d_{-211} spacing of $Li_7P_3S_{11}$, respectively[200].

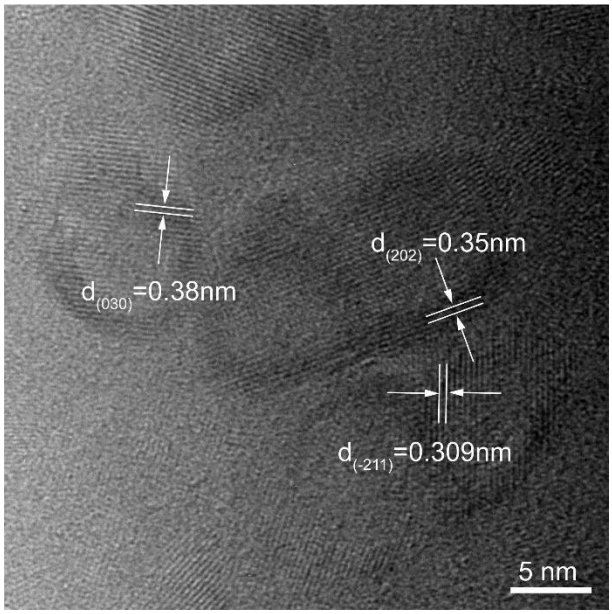

Figure 5-7 HRTEM images of MoS_6@15% $Li_7P_3S_{11}$.

To guarantee the uniformity of the characterization results, the SEM and TEM images of MoS_6@15%$Li_7P_3S_{11}$-2 and MoS_6@15%$Li_7P_3S_{11}$-3 are shown in Figure 5-8. Both of them display the particle size range of 1–4 μm, and show lattice fringes in TEM figures, which are well matched with MoS_6@15%$Li_7P_3S_{11}$ in Figure 5-4 and Figure 5-6.

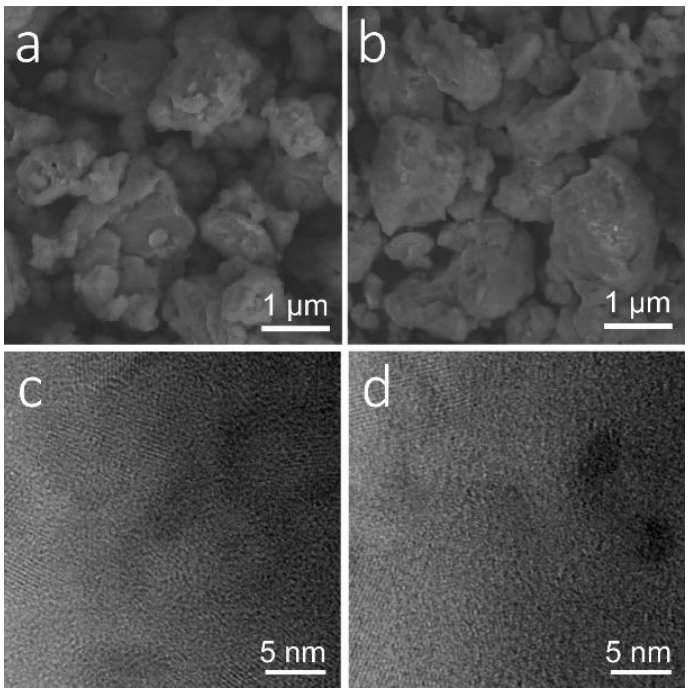

Figure 5-8 SEM images of (a) MoS_6@15%$Li_7P_3S_{11}$-2 and (b) MoS_6@15%$Li_7P_3S_{11}$-3. TEM images of (c) MoS_6@15%$Li_7P_3S_{11}$-2 and (d) MoS_6@15%$Li_7P_3S_{11}$-3.

5.2. Electrochemical performances of MoS_6@15% $Li_7P_3S_{11}$

To reveal the electrochemical reaction mechanism of MoS_6 and MoS_6@15% $Li_7P_3S_{11}$ composites, CV curves of Li/Li_6PS_5Cl/MoS_6 and Li/Li_6PS_5Cl/MoS_6@15%$Li_7P_3S_{11}$ all-solid-state batteries were performed for the first three cycles, as shown in Figure 5-9. During the first cathodic scan, reduction peak around 1.75 V can be attribute to the lithiation process of MoS_6 and further conversion process. During the initial anodic scanning period, the oxidation peak at 2.25 V corresponds to the de-lithiation processes and the forming of molybdenum sulfides. The CV curves of MoS_6@15%$Li_7P_3S_{11}$

composite are similar to those of the MoS_6, showing the same electrochemical reaction process[200, 270, 275, 278]. Even so, the redox peaks of MoS_6@15%$Li_7P_3S_{11}$ composite are narrower and stronger than those of the MoS_6, indicating the enhancement of reversibility and electrochemical reaction kinetics owning to the favorable ionic diffusion. The apparent overlapping of CV curves from the second cycle indicates that MoS_6@15%$Li_7P_3S_{11}$ composite has excellent cycling stability.

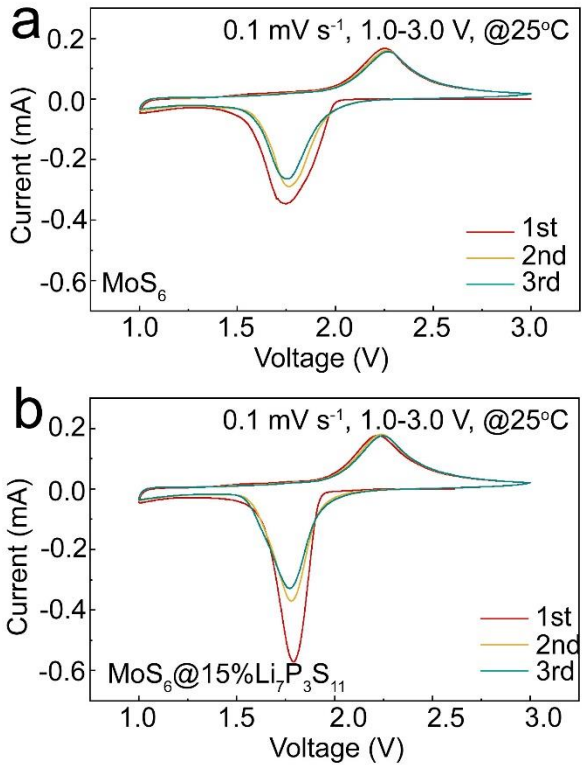

Figure 5-9 CV curves of (a) MoS_6 and (b) MoS_6@15%$Li_7P_3S_{11}$ composite.

Figure 5-10 present the first three cycles galvanostatic

discharge-charge curves of MoS_6 and MoS_6@15% $Li_7P_3S_{11}$ composites in all-solid-state lithium batteries under 0.1 A g^{-1} at 25 ^oC. The all-solid-sate lithium battery with MoS_6 cathodes deliver high initial discharge capacities of 913.9 mAh g^{-1}. After coupling with $Li_7P_3S_{11}$ solid-electrolyte thin layer, all-solid-state lithium battery with MoS_6@15%$Li_7P_3S_{11}$ composite cathodes can deliver an initial and reversible discharge capacities of 1083.8 mAh g^{-1} and 851.5 mAh g^{-1}, respectively (Figure 5-10b), which are superior to the values of many sulfide-based cathode materials reported previously, such as rGO-MoS_3, cubic FeS_2, Co_9S_8@$Li_7P_3S_{11}$ and MoS_2@$Li_7P_3S_{11}$[179, 190, 200, 261].

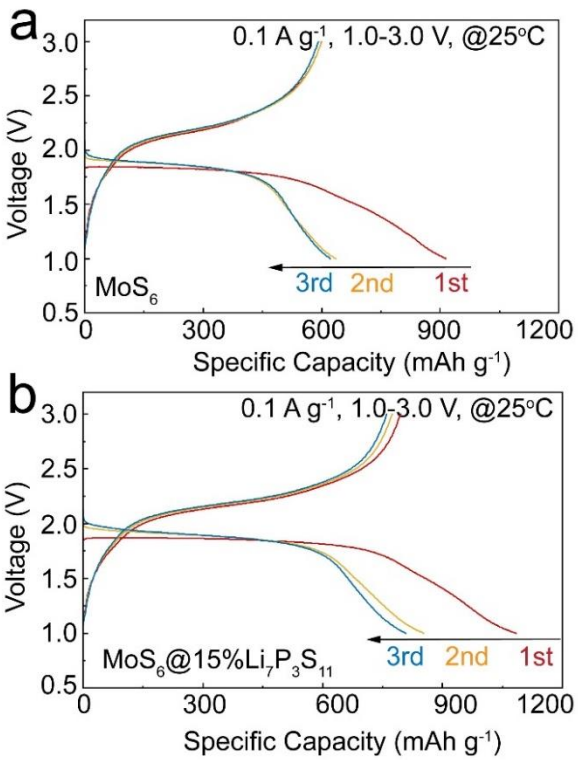

Figure 5-10 Galvanostatic discharge/charge profiles of (a) MoS_6 and (b) MoS_6@15%$Li_7P_3S_{11}$ composite cathodes at 0.1 A g^{-1}.

To guarantee the reproducibility of electrochemical performances, the initial discharge specific capacity of MoS_6@15%$Li_7P_3S_{11}$-1, MoS_6@15%$Li_7P_3S_{11}$-2 and MoS_6@15%$Li_7P_3S_{11}$-3 under the current density of 0.1 A g^{-1} are shown in Table 5-1. All of them display the similar number, demonstrating the reproducibility of the data.

Table 5-1 The specific capacity comparison of MoS_6@15%$Li_7P_3S_{11}$-1, MoS_6@15%$Li_7P_3S_{11}$-2 and MoS_6@15%$Li_7P_3S_{11}$-3 under the current density of 0.1 A g^{-1}.

Sample No.	Current density (A g^{-1})	Specific capacity (mAh g^{-1})
MoS_6@15%$Li_7P_3S_{11}$-1	0.1	1083.8
MoS_6@15%$Li_7P_3S_{11}$-2	0.1	1116.5
MoS_6@15%$Li_7P_3S_{11}$-3	0.1	1107.5

As shown in Table 5-2, the initial discharge capacity of rGO-MoS_3, FeS_2, Co_9S_8@$Li_7P_3S_{11}$ and MoS_2@$Li_7P_3S_{11}$ were 1241.4 mAh g^{-1}, 750 mAh g^{-1}, 633 mAh g^{-1} and 868.4 mAh g^{-1}, while the reversible capacities were around 760 mAh g^{-1}, 730 mAh g^{-1}, 574 mAh g^{-1} and 669.2 mAh g^{-1}, separately. The increased reversible discharge capacity compared with MoS_6 could be attributed to the better interface compatibility between active material and solid electrolyte.

Table 5-2 Electrochemical performances comparison of various active materials in all-solid-state batteries.

Active Material	Electrolyte	Anode	Voltage Range (V)	Initial Capacity (mAh g^{-1})	Reversible Capacity (mAh g^{-1})	References
rGO-MoS_3	$Li_{10}GeP_2S_{12}$/75%Li_2S-24%P_2S_5-1%P_2O_5	Li	0.5–3 V	1241.4	~760	17
Cubic FeS_2	77.5%Li_2S-22.5%P_2S_5	Li	1–3 V	750	~730	10
Co_9S_8@$Li_7P_3S_{11}$	$Li_{10}GeP_2S_{12}$/75%Li_2S-24%P_2S_5-1%P_2O_5	Li	0.5–3 V	633	574	21
MoS_2@$Li_7P_3S_{11}$	$Li_7P_3S_{11}$	Li	0.1–3 V	868.4	669.2	19
MoS_6	Li_6PS_5Cl	Li	1–3 V	913.9	635.1	This work
MoS_6@15%$Li_7P_3S_{11}$	Li_6PS_5Cl	Li	1–3 V	1083.8	851.5	This work

As shown in Figure 5-11, MoS_6@15%$Li_7P_3S_{11}$ composite exhibits a remarkably stable cyclic performance with an impressive reversible specific capacity of 693.2 mAh g^{-1} after 20 cycles, while MoS_6 only shows 517.7 mAh g^{-1}. The excellent electrochemical performance of MoS_6@15%$Li_7P_3S_{11}$ composite attribute to the $Li_7P_3S_{11}$ thin layer, which can improve the cathode-electrolyte compatibility.

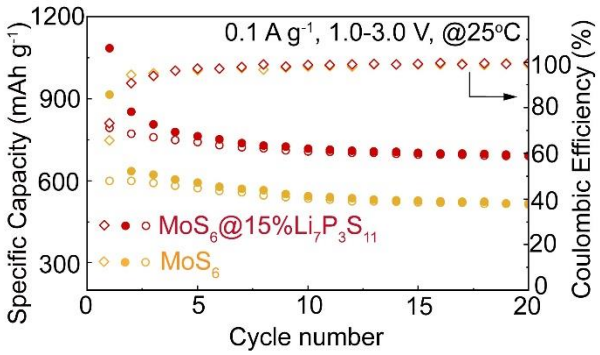

Figure 5-11 Cyclic performances of Li/Li_6PS_5Cl/MoS_6 and Li/Li_6PS_5Cl/MoS_6@15%$Li_7P_3S_{11}$ all-solid-state batteries under 0.1 A g^{-1}.

Actually, the coating ratio of $Li_7P_3S_{11}$ solid electrolyte also effect the electrochemical performances of MoS_6@$Li_7P_3S_{11}$ composites (Figure 5-12). Li/Li_6PS_5Cl/MoS_6@10%$Li_7P_3S_{11}$ and Li/Li_6PS_5Cl/MoS_6@20%$Li_7P_3S_{11}$ deliver initial discharge of 967.8 mAh g^{-1} and 991.4 mAh g^{-1}, respectively. After 20 cycles, the capacity retention of 10%$Li_7P_3S_{11}$ and 20%$Li_7P_3S_{11}$ coated electrodes were 476.1 mAh g^{-1} and 496.3 mAh g^{-1}. Obviously,

Li/Li_6PS_5Cl/MoS_6@15%$Li_7P_3S_{11}$ displays a highest reversible capacity.

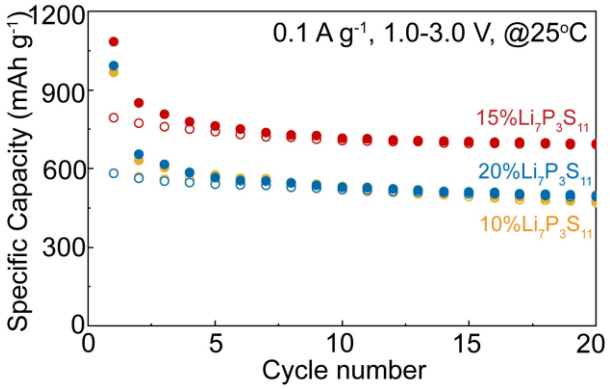

Figure 5-12 Cyclic performances of MoS_6@10%$Li_7P_3S_{11}$, MoS_6@15%$Li_7P_3S_{11}$ and MoS_6@20%$Li_7P_3S_{11}$ cathodes under 0.1 A g^{-1}.

To explore the principle of cathode kinetics and capacity variation for Li/Li_6PS_5Cl/MoS_6 and Li/Li_6PS_5Cl/MoS_6@15%$Li_7P_3S_{11}$ all-solid-state lithium battery, EIS was conducted with the amplitude of 15 mV from 10^6 to 0.1 Hz. The corresponding equivalent circuit model is shown in the Figure 5-13, where R_e is the resistance of the electrolyte, semicircle shows the interfacial charge transfer resistance (R_{ct}) emerges, the constant phase angle element (*CPE*) is used to indicate the behavior of non-ideal capacitance of the double-layer and Z_w represents the Warburg resistance, which indicating the lithium ions diffuse into the bulk electrodes[200, 270].

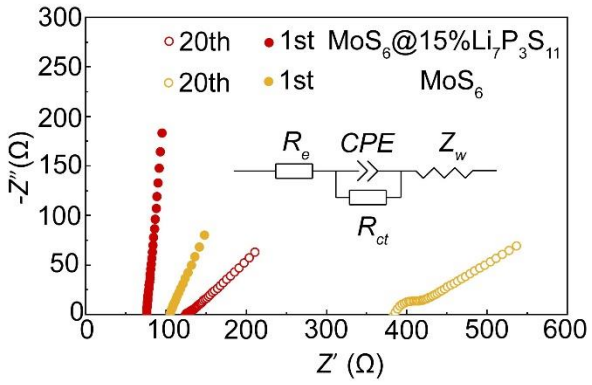

Figure 5-13 Nyquist plots and the equivalent circuit diagram of MoS_6 and MoS_6@15%$Li_7P_3S_{11}$ composite cathodes over range of 1.0–3.0 V at 0.1 A g^{-1}after 1st and 20th cycles.

The fitted results of R_e and R_{ct} are listed in Table 5-3. After the first cycle, the EIS plots of both all-solid-state lithium batteries are straight lines. MoS_6@15%$Li_7P_3S_{11}$ composite exhibits a R_e value of 75.89 Ω, which is lower than that of MoS_6 with 105.42 Ω. After 20 cycles, MoS_6 delivers higher R_e (384.11 Ω) and R_{ct} (52.96 Ω). On the contrary, MoS_6@15%$Li_7P_3S_{11}$ composite shows R_e and R_{ct} values of 124.79 Ω and 10.78 Ω due to the intimate interfacial contacts.

Table 5-3 EIS fitting results of MoS_6 and MoS_6@15%$Li_7P_3S_{11}$ under 0.1 A g^{-1} after 20 cycles.

Cathode materials	1st cycle		20th cycle	
	R_e (Ω)	R_{ct} (Ω)	R_e (Ω)	R_{ct} (Ω)
MoS_6	105.42	/	384.11	52.96
MoS_6@15%$Li_7P_3S_{11}$	75.89	/	124.79	10.78

The rate capabilities of MoS_6 and MoS_6@15%$Li_7P_3S_{11}$ composite cathode were performed under various current densities from 0.1 to 2 A g^{-1} (Figure 5-14). MoS_6@15%$Li_7P_3S_{11}$ composite cathode exhibited superior reversible discharge capacities of 801.5, 648.1, 536.3, 454.4 and 370.8 mAh g^{-1} under current densities of 0.1, 0.2, 0.5, 1 and 2 A g^{-1}, respectively, while MoS_6 only delivered 683.9, 516.8, 407.7, 326.2 and 255.8 mAh g^{-1}. The excellent rate capability of MoS_6@15%$Li_7P_3S_{11}$ composite can be attributed to enhanced ionic diffusivity, which lead to improved electrochemical reaction kinetics.

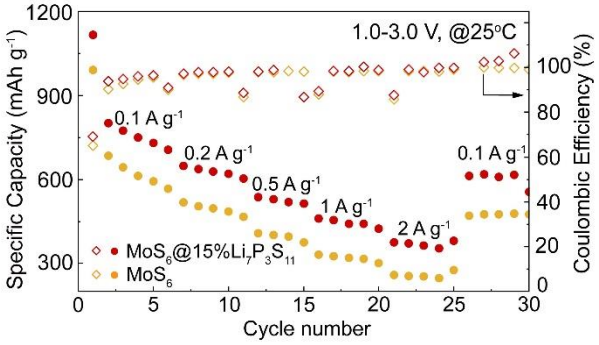

Figure 5-14 Rate performances of MoS_6 and MoS_6@15%$Li_7P_3S_{11}$ composite under different current densities.

As shown in Figure 5-15, the Ragone plot gives the relationship between the average power density and energy density. Under current density of 0.1 and 2.0 A g^{-1}, the MoS_6@15%$Li_7P_3S_{11}$ composite cathodes deliver energy and power densities of 588 Wh kg^{-1} and

1358 W kg^{-1} based on the total cathode layer composed of MoS_6@15%$Li_7P_3S_{11}$ composite, $Li_{10}GeP_2S_{12}$ and super P, which are significantly higher than 495.8 Wh kg^{-1} and 1332.2 W kg^{-1} of MoS_6 at the same current densities, respectively.

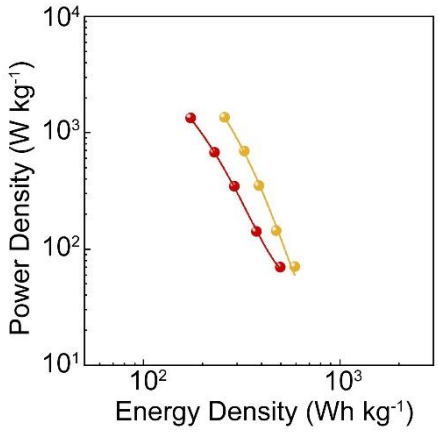

Figure 5-15 Ragone plot deduced from the rate performances in Figure 5-14.

The long-term cycling stability of MoS_6@15%$Li_7P_3S_{11}$ composite cathode under 1 A g^{-1} is further shown in Figure 5-16a, showing high reversible capacity of 400 mAh g^{-1} after 1000 cycles. Furthermore, the $Li_7P_3S_{11}$ thin layer still existed even after long-term cycling, as shown in Figure 5-16b. The EDS mapping of MoS_6@15%$Li_7P_3S_{11}$ composite clearly illustrate the well distribution of phosphorus (red), sulfur (yellow), and molybdenum (green).

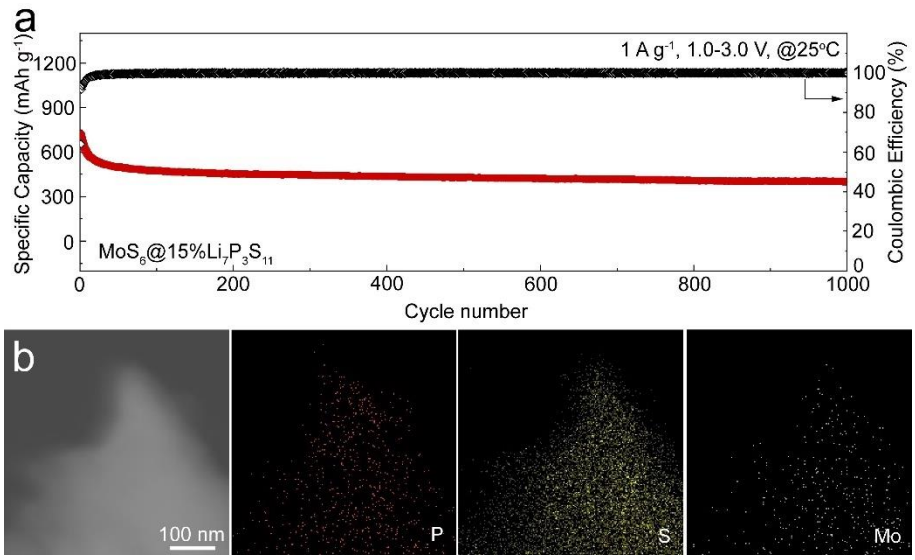

Figure 5-16 (a) Long-term cyclic performance of MoS_6@15%$Li_7P_3S_{11}$ composite under 1 A g^{-1}. (b) The EDS mapping of MoS_6@15%$Li_7P_3S_{11}$ composite after 1000 cycles.

CV measurements were also conducted to illustrate the electrochemical reaction kinetics. The relationship between the peak current (i) and scan rate obeys the power law: $i = av^b$. The b-value is fitted by the log(v)-log(i) plot. The b-value of 1.0 indicates a surface-mediated mode while 0.5 displays a diffusion-controlled mode. As shown in Figure 5-17a, c, the CV curves show similar shapes and gradually broadened redox peaks. Under the same scan rate, the curves intensity of MoS_6@15%$Li_7P_3S_{11}$ composite was higher than MoS_6, indicating MoS_6@15%$Li_7P_3S_{11}$ composite can maintain a fast electrochemical kinetics with increasing scan rate. As shown in Figure 5-17b, the fitted b-values of reduction peak and oxidation peak are 0.50 and 0.67 in MoS_6@15%$Li_7P_3S_{11}$ composite,

respectively, which are lower than the fitting *b*-values of 0.62 and 0.76 in MoS_6 (Figure 5-17d), indicating the electrochemical reaction kinetics are dominated by diffusion-controlled processes. This condition allows full intercalation of lithium ions, thereby realize high reversible capacity[261, 279].

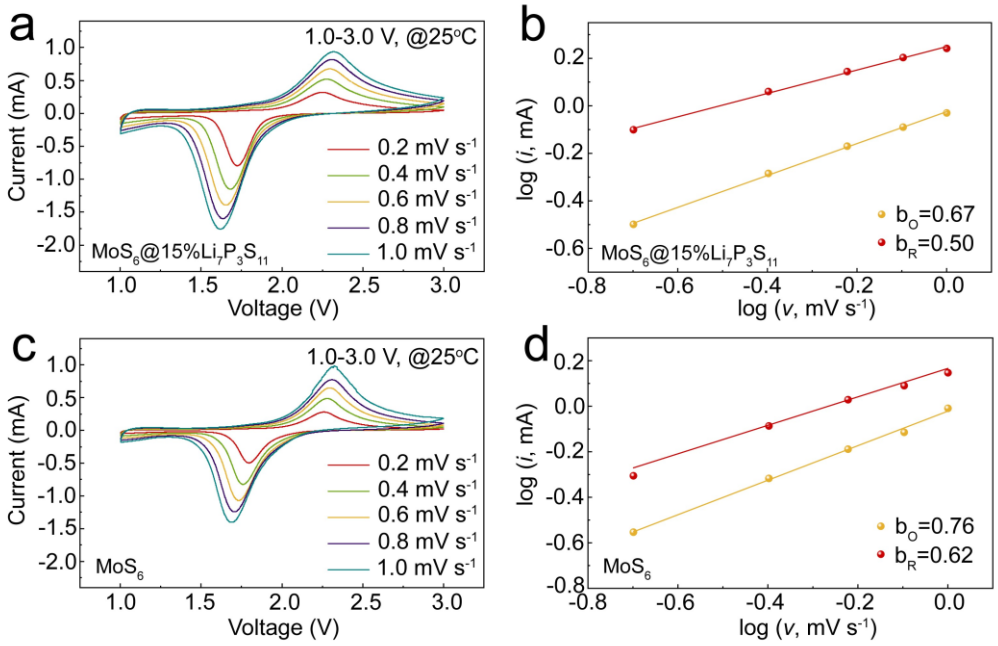

Figure 5-17 CV curves at different scan rates of (a) MoS_6@15%$Li_7P_3S_{11}$ composite and (c) MoS_6. The log (peak current) *vs.* log (scan rate) fitted plots at reduction and oxidation peaks of (b) MoS_6@15%$Li_7P_3S_{11}$ composite and (d) MoS_6.

To further quantify the ionic transport kinetics of Li/Li_6PS_5Cl/MoS_6@15%$Li_7P_3S_{11}$ and Li/Li_6PS_5Cl/MoS_6 all-solid-state batteries, GITT were conducted to determine the lithium ions diffusion coefficient at 1 A g^{-1} under 1.0–3.0 V. As shown in Figure

5-18, the ion diffusion coefficient range of MoS_6@15%$Li_7P_3S_{11}$ composite were calculated to be 10^{-11}–10^{-10} cm^2 s^{-1}, which is higher than MoS_6 with 10^{-12}–10^{-11} cm^2 s^{-1}. Obviously, the ionic diffusivity of MoS_6@15%$Li_7P_3S_{11}$ composite was enhanced significantly, which is beneficial for the rapid lithium ions transportation, and thus significantly improving the electrochemical performances in terms of high discharge capacity and rate capability.

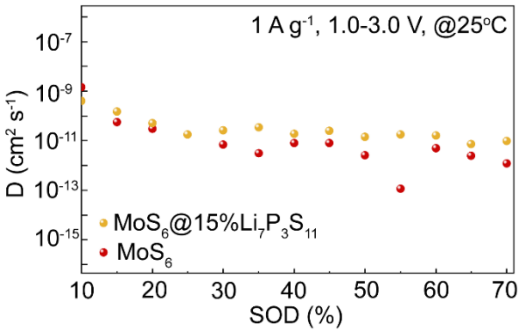

Figure 5-18 GITT plot of Li/Li_6PS_5Cl/MoS_6@15%$Li_7P_3S_{11}$ composite and Li/Li_6PS_5Cl/MoS_6 all-solid-state lithium batteries.

In this work, $Li_7P_3S_{11}$ was *in-situ* coated on the MoS_6, the resultant MoS_6@15%$Li_7P_3S_{11}$ can realize the intimate contact between the cathode material and solid electrolyte, while decreasing the weight ratio of active material based on the total cathode layer, which decreases the energy density. Another MoS_6 based composite was designed in this project, which not only increases the weight ratio of MoS_6 for a higher energy density, but also improves the utilization of the active material, releasing a high specific capacity

during the charge-discharge process.

Chapter 6. $95MoS_6 \cdot 5LiI$[3]

6.1. Characterization results of $95MoS_6 \cdot 5LiI$

The preparation of $95MoS_6 \cdot 5LiI$ composite are schematically illustrated in Figure 6-1. LiI was mixed with MoS_6 homogeneously by ball milling. After mixed as-prepared $95MoS_6 \cdot 5LiI$ with $Li_{10}GeP_2S_{12}$ and Super P, the composite cathodes were obtained.

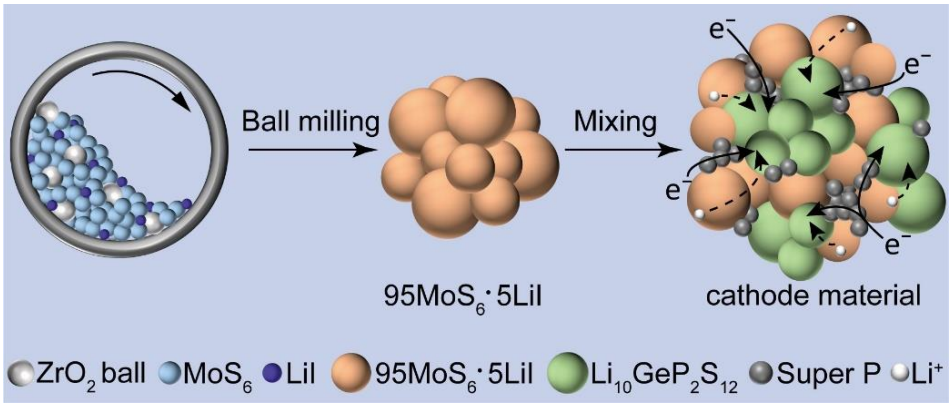

Figure 6-1 schematic illustration of preparation process for $95MoS_6 \cdot 5LiI$ composite.

X-ray diffraction (XRD) patterns of MoS_6 and $95MoS_6 \cdot 5LiI$ composites are shown in Figure 6-2, demonstrating the amorphous structure of MoS_6. No diffraction peaks of LiI were detected, indicating the low mixing amount of LiI.

[3] The data used in this chapter have been accepted by Mingyuan Chang as first author to the journal of chemcomm named "LiI doped MoS_6 composite for room temperature all-solid-state lithium batteries"

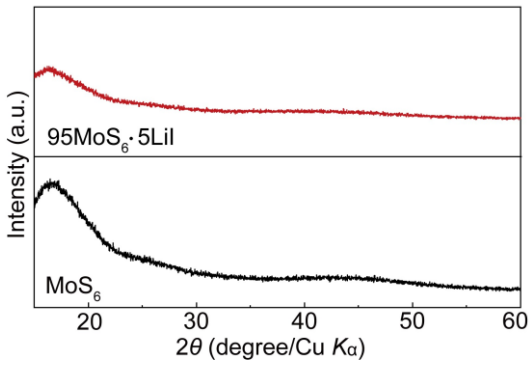

Figure 6-2 XRD pattern of MoS_6 and $95MoS_6{\cdot}5LiI$ composite.

As shown in Figure 6-3, the morphology and microstructure of MoS_6 and $95MoS_6{\cdot}5LiI$ were clearly detected by field emission scanning electron microscopy (SEM) and high-resolution transmission electron microscopy (HRTEM). After ball milling process, the particle sizes for $95MoS_6{\cdot}5LiI$ composite were in the range of 0.5–2 μm (Fig. 6-3b), which was smaller than that of MoS_6 (1–4 μm) (Fig. 6-3a).

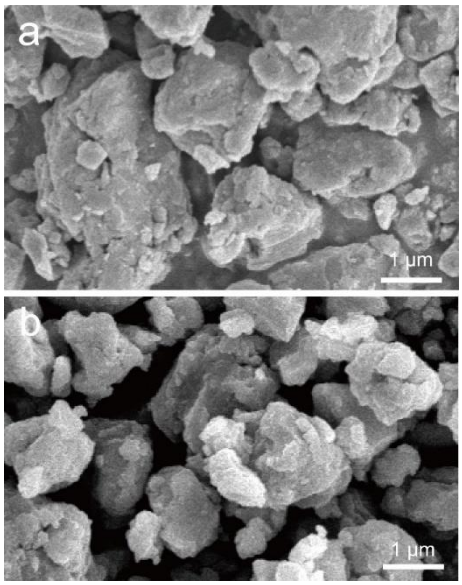

Figure 6-3 SEM images of (a) MoS_6 and (b) $95MoS_6{\cdot}5LiI$ composite.

The scanning transmission electron microscopy-energy dispersive spectroscopy (STEM-EDS) mapping images of $95MoS_6{\cdot}5LiI$ further illustrate the well distribution of S (yellow), Mo (blue) and I (green) (Figure 6-4).

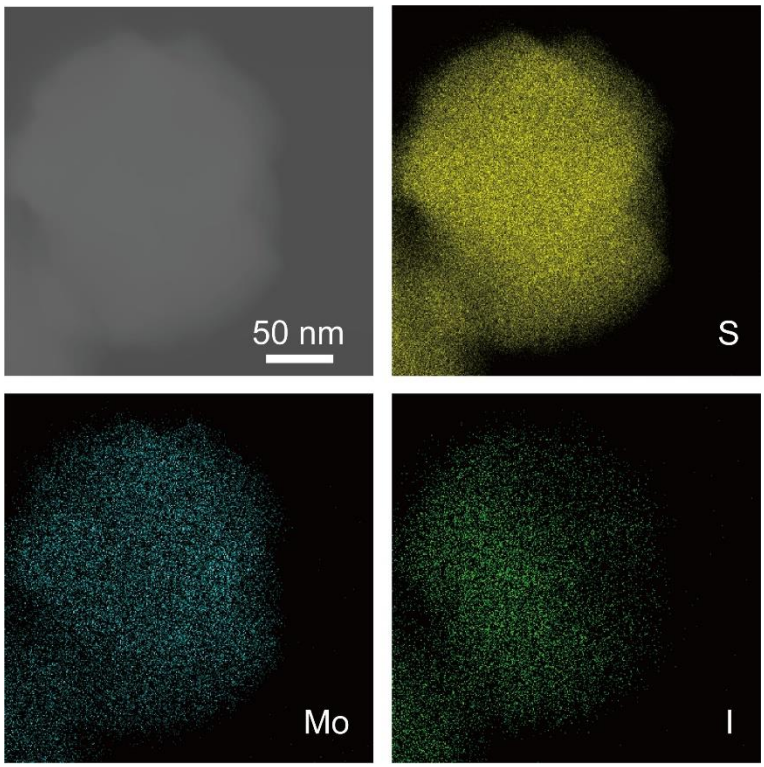

Figure 6-4 STEM elemental mapping images of $95MoS_6{\cdot}5LiI$ composite.

The TEM images and selected area electron diffraction (SAED) pattern (Figure 6-5) further confirm the amorphous nature of $95MoS_6{\cdot}5LiI$ composite after ball milling, which display similar morphology with that of MoS_6 (Fig. 6-5b). Furthermore, there is no lattice in the $95MoS_6{\cdot}5LiI$ composite, as shown by the SAED pattern (Figure 6-5c).

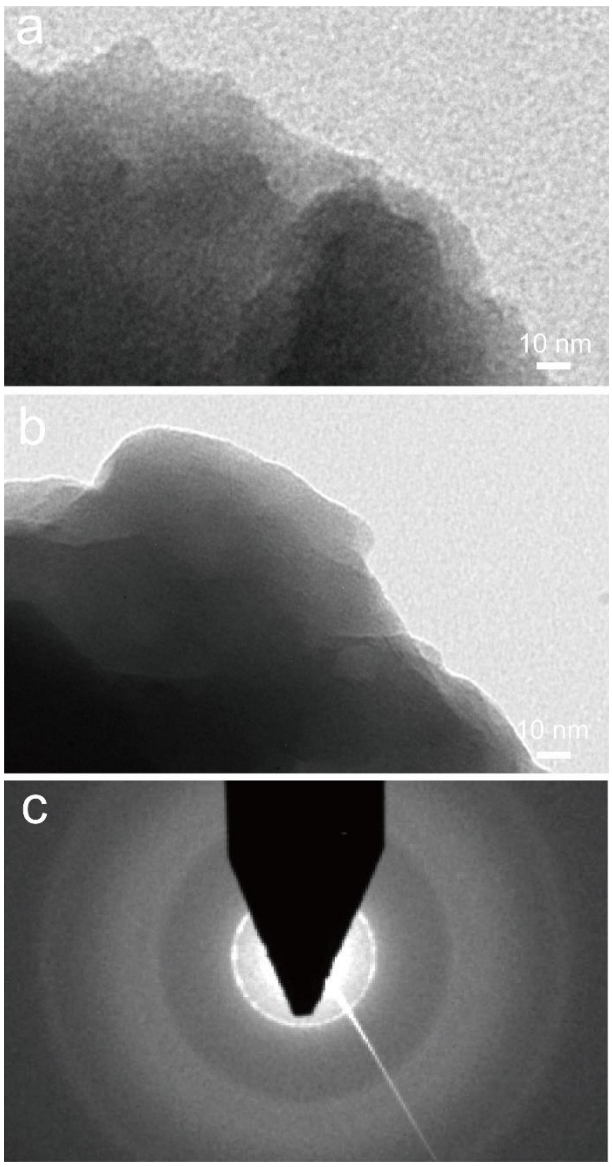

Figure 6-5 TEM images of (a) MoS_6 and (b) $95MoS_6{\cdot}5LiI$ composite as well as SAED pattern of (c) $95MoS_6{\cdot}5LiI$ composite.

To guarantee the uniformity of the characterization results, the SEM and TEM figures of $95MoS_6{\cdot}5LiI$-2 and $95MoS_6{\cdot}5LiI$-3 are shown in Figure 6-6. Both of them display the particle size range of 0.5–2 μm, and show the amorphous structure in TEM figures, which are well matched with $95MoS_6{\cdot}5LiI$ in Figure 6-3 and Figure 6-5.

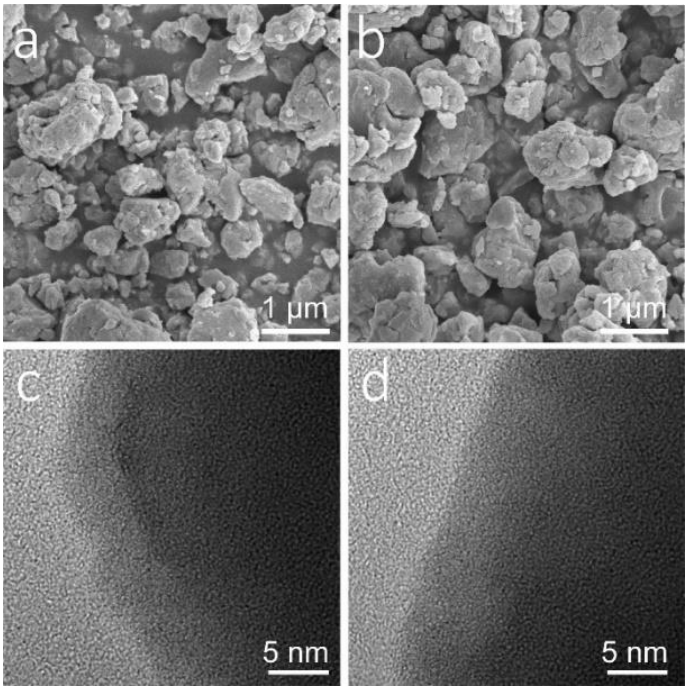

Figure 6-6 SEM images of (a) MoS_6-2 and (b) MoS_6-3. TEM images of (c) MoS_6-2 and (d) MoS_6-3.

To demonstrate the successful doping of LiI into the MoS_6 matrix, time-of-flight secondary ion mass spectroscopy (TOF-SIMS) was employed to demonstrate the ionic bonds differentiation among MoS_6, LiI and $95MoS_6{\cdot}5LiI$. The TOF-SIMS 3D distribution images of I^-, S_2^{2-} and IS^{3-} for MoS_6, LiI and $95MoS_6{\cdot}5LiI$ are shown in Figure 6-7. Due to the chemical properties, only S_2^{2-} and I^- were detected in MoS_6 and LiI, respectively. After doping LiI into the MoS_6, IS^{3-} ions were homogeneously distributed in the $95MoS_6{\cdot}5LiI$ composite, which indicates that the $95MoS_6{\cdot}5LiI$ is solid solution instead of simply mixture.

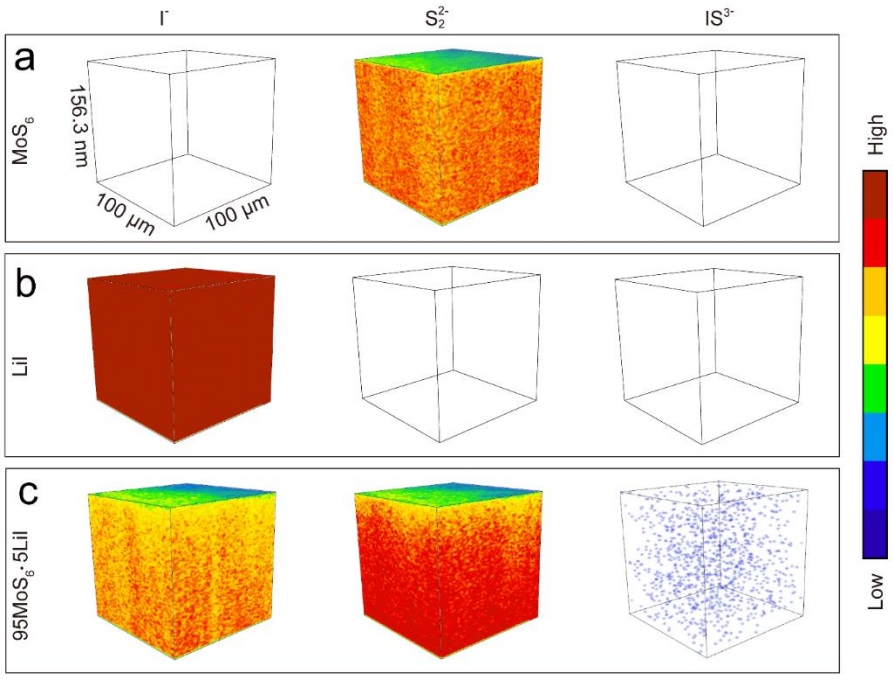

Figure 6-7 TOF-SIMS 3D distribution images of I^-, S_2^{2-} and IS^{3-} ions for (a) MoS_6, (b) LiI and (c) $95MoS_6 \cdot 5LiI$. Blue and red color present low and high content of ions, respectively.

6.2. Electrochemical performances of $95MoS_6 \cdot 5LiI$

To demonstrate the electrochemical performance of MoS_6 and $95MoS_6 \cdot 5LiI$ composite, the cyclic voltammetry curves (CVs) of $Li/Li_6PS_5Cl/MoS_6$ and $Li/Li_6PS_5Cl/95MoS_6 \cdot 5LiI$ all-solid-state batteries were conducted at room temperature for the initial three cycles between 1.0 V and 3.0 V at a scan rate of 0.1 mV s^{-1} (Figure 6-8). The reduction peak at 1.75 V could be indicated that the lithiation and the following conversion process. During the anodic scanning scan, the peak at 2.25 can be attributed to the de-lithiation process and the formation of molybdenum sulfide. The CV curves of

MoS_6 and $95MoS_6{\cdot}5LiI$ composites possess similar peaks, demonstrating the similar electrochemical reaction mechanism. The redox peaks of $95MoS_6{\cdot}5LiI$ are stronger than MoS_6, indicating the improved ionic transport kinetics of the electrochemical reaction.

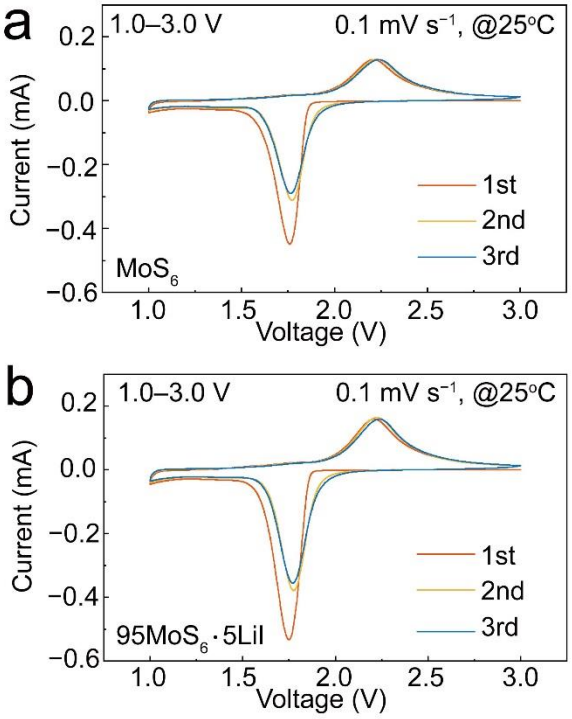

Figure 6-8 CV curves of (a) MoS_6 and (b) $95MoS_6{\cdot}5LiI$ composite.

The initial three cycles galvanostatic discharge-charge curves of $Li/Li_6PS_5Cl/MoS_6$ and $Li/Li_6PS_5Cl/95MoS_6{\cdot}5LiI$ all-solid-state batteries are presented in Figure 6-9. The MoS_6 delivers an initial and reversible discharge capacity of 916.9 mAh g^{-1} and 595.2 mAh g^{-1} at 0.1 A g^{-1} under 25 °C within 1.0–3.0 V (*vs.* Li/Li^+). By ball milling with LiI, $95MoS_6{\cdot}5LiI$ composites show an improved initial and

reversible discharge capacity of 1016.3 mAh g^{-1} and 798 mAh g^{-1}, respectively.

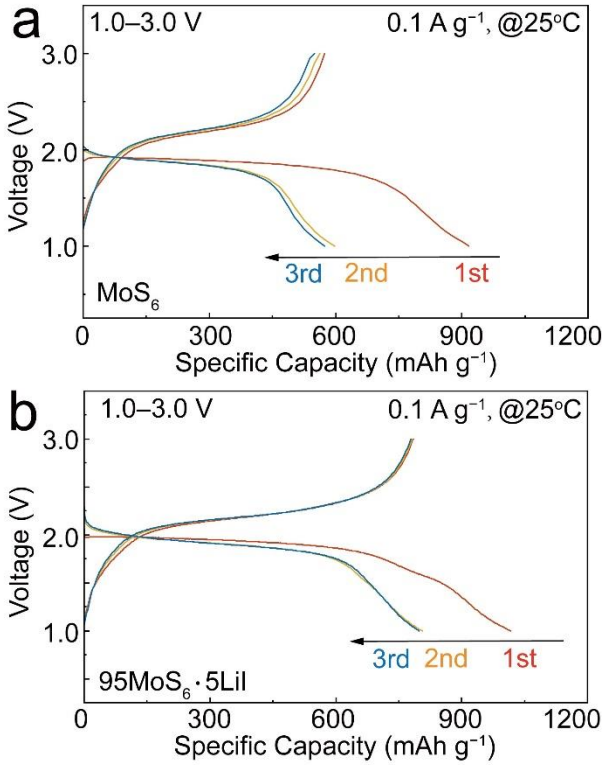

Figure 6-9 Galvanostatic discharge/charge profiles of (a) MoS_6 and (b) $95MoS_6{\cdot}5LiI$ composite over voltage range of 1.0–3.0 V under 0.1 A g^{-1}.

To guarantee the reproducibility of the electrochemical performances, the initial discharge specific capacity of $95MoS_6{\cdot}5LiI$-1, $95MoS_6{\cdot}5LiI$-2 and $95MoS_6{\cdot}5LiI$-3 under the current density of 0.1 A g^{-1} are shown in Table 6-1. All of them display the similar number, demonstrating the reproducibility of the data.

Table 6-1 The specific capacity comparison of $95MoS_6 \cdot 5LiI$-1, $95MoS_6 \cdot 5LiI$-2 and $95MoS_6 \cdot 5LiI$-3 under the current density of 0.1 A g^{-1}.

Sample No.	Current density (A g^{-1})	Specific capacity (mAh g^{-1})
$95MoS_6 \cdot 5LiI$-1	0.1	1016.3
$95MoS_6 \cdot 5LiI$-2	0.1	1023.9
$95MoS_6 \cdot 5LiI$-3	0.1	1026.1

Furthermore, $Li/Li_6PS_5Cl/95MoS_6 \cdot 5LiI$ all-solid-state batteries shows cycle life of 15 cycles with a high capacity retention of 762.8 mAh g^{-1} at 0.1 A g^{-1}, which is higher than the value of 485.4 in MoS_6 (Figure 6-10). It is expected that $95MoS_6 \cdot 5LiI$ composites were decomposed during the charge-discharge processes, which is beneficial for the LiI dispersing and consequently improve the reaction kinetics during the charge-discharge process[170].

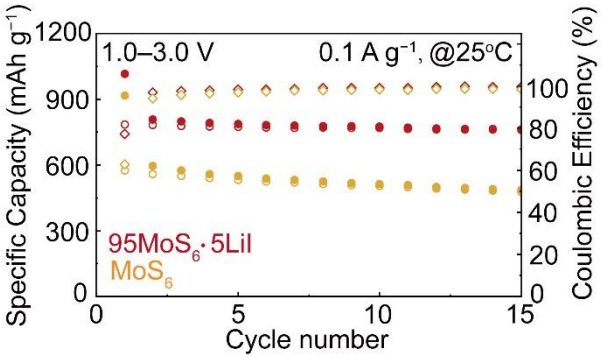

Figure 6-10 Cyclic performance of $95MoS_6 \cdot 5LiI$ composite and MoS_6 at 0.1 A g^{-1} within1.0–3.0 V.

Actually, the LiI contents significantly influence the electrochemical performances of the battery. $90MoS_6 \cdot 10LiI$ and $99MoS_6 \cdot 1LiI$ were also tested in all-solid-state batteries for comparison, only showing reversible capacities of 663 and 691.6 mAh g^{-1} after the fifteenth cycle (Fig. 6-11).

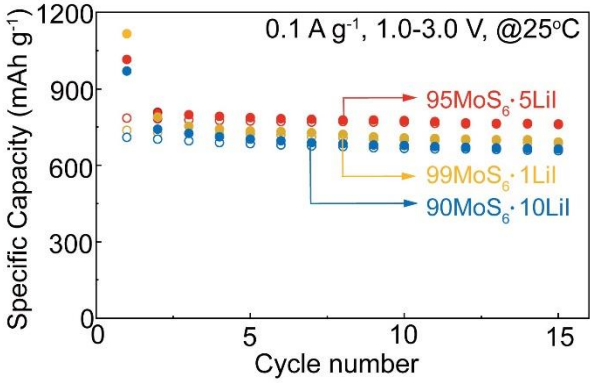

Figure 6-11 Cyclic performances of $90MoS_6 \cdot 10LiI$, $99MoS_6 \cdot 1LiI$ and $95MoS_6 \cdot 5LiI$ composite under 0.1 A g^{-1}.

The rate performance of MoS_6 and $95MoS_6 \cdot 5LiI$ composites were determined at different current densities from 0.1 A g^{-1} to 2 A g^{-1}, as shown in Figure 6-12. $95MoS_6 \cdot 5LiI$ composites display

improved reversible discharge capacities of 757.3, 610.9, 497.9, 412.7 and 328.6 mAh g^{-1} under current densities of 0.1, 0.2, 0.5, 1 and 2 A g^{-1}, respectively, while MoS_6 only exhibited 609.8, 409.8, 331.5, 273.6 and 224 mAh g^{-1}. The superior rate capability of $95MoS_6{\cdot}5LiI$ composites attributed to the enhanced electrochemical reaction kinetics.

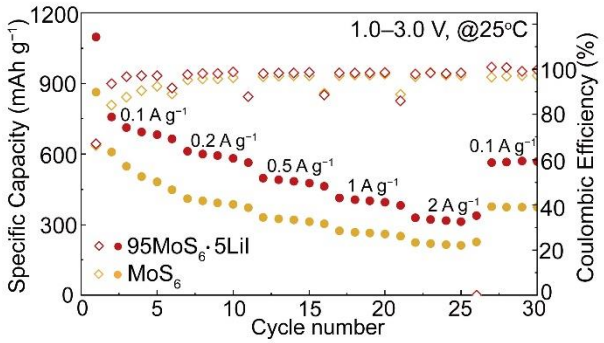

Figure 6-12 Rate performances of MoS_6 and $95MoS_6{\cdot}5LiI$ composite under different current densities.

The Ragone plot gives the relationship between the average energy density and power density (Figure 6-13). Under current density of 0.1 and 2.0 A g^{-1}, $95MoS_6{\cdot}5LiI$ composites exhibit energy and power density of 687.23 Wh kg^{-1} and 1351 W kg^{-1} based on the total cathode layer composed of $95MoS_6{\cdot}5LiI$ composites, $Li_{10}GeP_2S_{12}$ and super P, which are significantly higher than 498.7 Wh kg^{-1} and 1338.9 W kg^{-1} of MoS_6 at the same current densities, respectively.

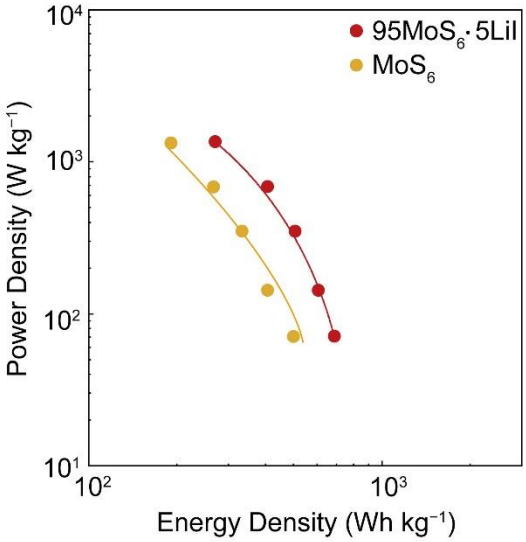

Figure 6-13 Ragone plot deduced from the rate performances in Figure 6-12.

The long-term cycling stability of MoS_6 and $95MoS_6{\cdot}5LiI$ composite under 1 A g^{-1} is further illustrated in Figure 6-14. After activation at 0.1 A g^{-1} for the first 5 cycles, the reversible capacity for MoS_6 rapidly decays for the first 100 cycles and decreases to 1.9 mAh g^{-1} after 500 cycles at 1 A g^{-1}. By sharp contrast, $95MoS_6{\cdot}5LiI$ composite shows high reversible capacity of 301.1 mAh g^{-1} after 500 cycles[261, 275].

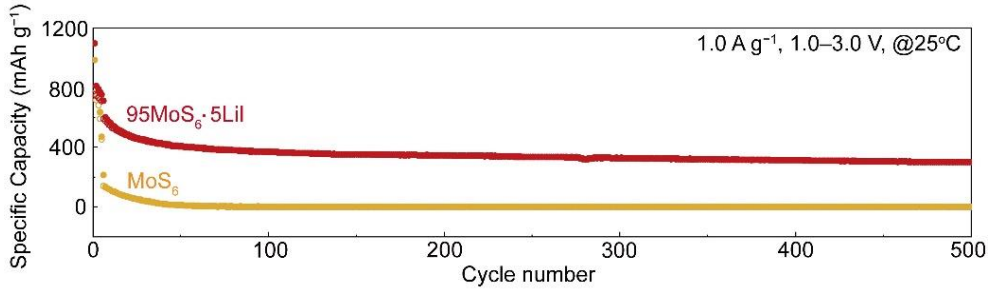

Figure 6-14 Long-term cyclic performance of MoS_6 and $95MoS_6{\cdot}5LiI$ composite under 1 A g^{-1}.

The electrochemical impedance spectroscopy (EIS) and the equivalent circuit model of MoS_6 and $95MoS_6{\cdot}5LiI$ composites were exhibited to explore the mechanism of capacity change and electrode reaction kinetics for all-solid-state batteries (Figure 6-15). The measurements were conducted in the frequency range from 1.0 MHz to 0.1 Hz with the amplitude of 10 mV. The fitted results are listed in Table 1. Where Z_w is the Warburg resistance, indicating the lithium ions diffuse into the bulk electrodes. *CPE* (constant phase element) compensate for the non-ideal behavior resulting from the rough electrode surface. R_e is the resistance of the electrolyte, and R_{ct} presents the interfacial charge transfer resistance[200, 270, 275].

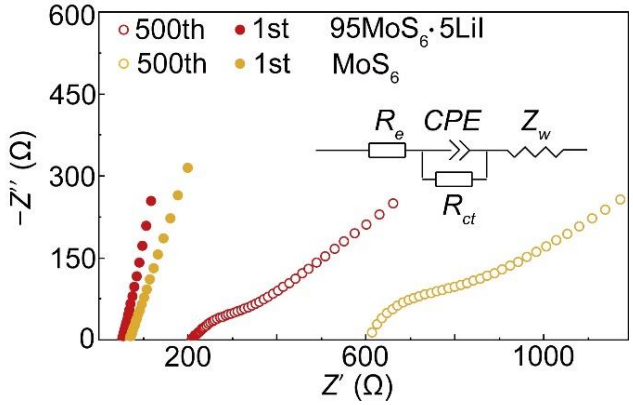

Figure 6-15 Nyquist plots and the equivalent circuit diagram of MoS_6 and $95MoS_6{\cdot}5LiI$ composite cathodes after 1st and 500th cycles at 1 A g^{-1} within1.0–3.0 V.

After the first cycle, MoS_6 and $95MoS_6{\cdot}5LiI$ composites show similar R_e values of 69.87 and 52.58 Ω. However, the MoS_6 displayed sharp increase in R_e and R_{ct} values (605.71 and 447.82 Ω) after 500

cycles, while $95MoS_6$·5LiI composites deliver 208.36 and 352.25 Ω due to the intimate interfacial contacts (Table 6-2).

Table 6-2 EIS fitting results of MoS_6 and $95MoS_6$·5LiI composites under 1 A g^{-1} after 500 cycles.

Cathode materials	1st cycle		500th cycle	
	R_e (Ω)	R_{ct} (Ω)	R_e (Ω)	R_{ct} (Ω)
MoS_6	69.87	/	605.71	447.82
$95MoS_6$·5LiI	52.58	/	208.36	352.25

In order to further analysis the electrochemical reaction kinetics of MoS_6 and $95MoS_6$·5LiI composite, CV and GITT were performed, as shown in Figure 6-16. The CV curves of MoS_6 and $95MoS_6$·5LiI exhibit similar shapes and gradually broaden with the increase of scan rates (Figure 6-16a and c). At the same scan rate, $95MoS_6$·5LiI displays higher peak intensity than that of MoS_6, indicating a faster electrochemical kinetics. The relationship between the scan rate and peak current (i) is followed by the equation of $i = av^b$. The b-value fitted from log(v)-log(i) plot gives information of surface-mediated mode (1.0) or diffusion-controlled mode (0.5). As shown in Figure 6-16b, the fitting b-values of reduction and oxidation peaks are 0.55 and 0.67 for $95MoS_6$·5LiI composite, which is similar with 0.60 and 0.69 for

MoS_6 (Figure 6-16d), indicating the electrochemical reaction kinetics of $95MoS_6{\cdot}5LiI$ and MoS_6 are dominated by diffusion-controlled process, allowing lithium ions fully intercalated[261, 279].

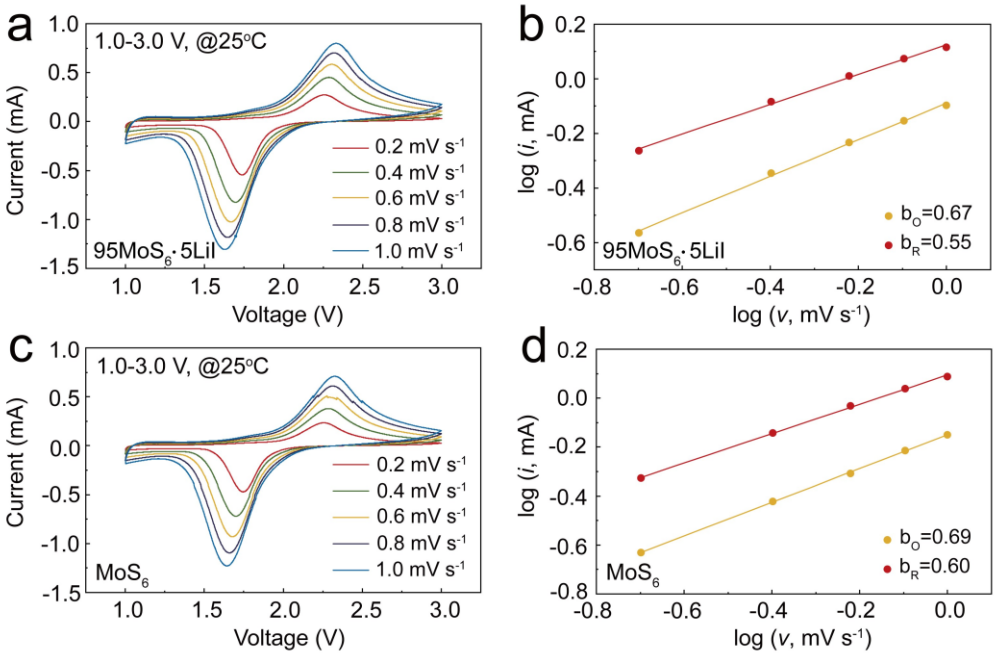

Figure 6-16 CV curves of (a) $95MoS_6{\cdot}5LiI$ composite and (c) MoS_6 with various scan rates. The log (peak current) *vs.* log (scan rate) simulation plots at reduction and oxidation peaks of (b) $95MoS_6{\cdot}5LiI$ and (d) MoS_6.

As shown in Figure 6-17a, measured diffusivities plot further illustrate the improved lithium ions diffusion coefficient at 0.1 A g^{-1}, which was calculated from the GITT results (Figure 6-17b) with the Fick's second law $D = \frac{4}{\pi\tau}\left(\frac{n_m v_m}{S}\right)^2\left(\frac{\Delta E_s}{\Delta E_t}\right)^2$, where τ is the time duration of the pulse, n_m and v_m are the molar mass (mol) and volume (cm^3/mol). S is the interfacial area of cells, ΔE_s and

ΔE_t are voltage drops of the pulse and discharge process[3]. The average ion diffusion coefficient of $95MoS_6{\cdot}5LiI$ was 1.23×10^{-10} $cm^2\ s^{-1}$, which is twice higher than that of MoS_6 with 5.03×10^{-11} $cm^2\ s^{-1}$. The enhanced ionic diffusivity of $95MoS_6{\cdot}5LiI$ indicates the diffusion-controlled process proceed smoothly, which is beneficial for the high-efficiency lithium ions transportation, as a result significantly improving the reversible capacity and cycle stability[261, 279].

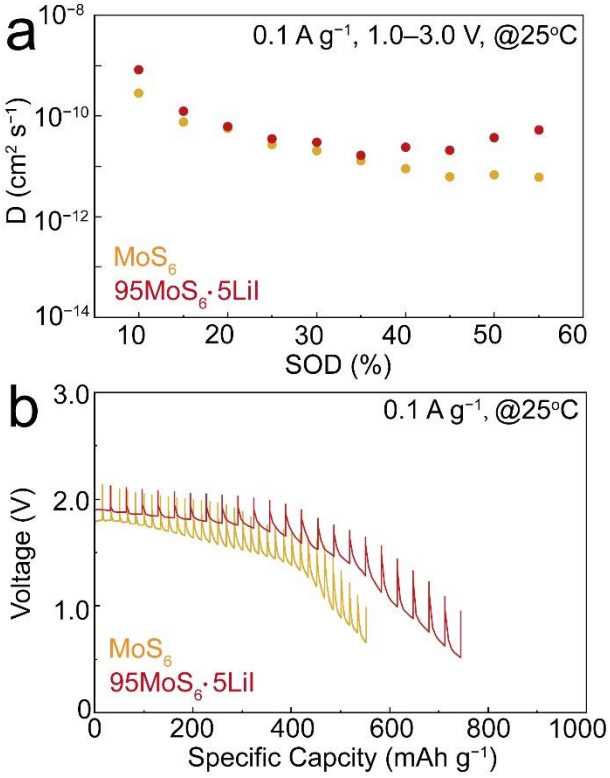

Figure 6-17 (a) Measured diffusivities plot of $Li/Li_6PS_5Cl/95MoS_6{\cdot}5LiI$ and $Li/Li_6PS_5Cl/MoS_6$ all-solid-state lithium batteries. The plot is derived from GITT measurements. (b) GITT plot of $Li/Li_6PS_5Cl/95MoS_6{\cdot}5LiI$ and $Li/Li_6PS_5Cl/MoS_6$ all-solid-state lithium batteries.

In summary, a transition metal sulfide composite $95MoS_6 \cdot 5LiI$ with superior electrochemical reaction kinetics for all-solid-state lithium batteries is proposed. After cooperated LiI with MoS_6, the average ion diffusion coefficient was improved from 5.03×10^{-11} cm^2 s^{-1} for MoS_6 to 1.23×10^{-10} cm^2 s^{-1} for $95MoS_6 \cdot 5LiI$. The all-solid-state lithium batteries with $95MoS_6 \cdot 5LiI$ exhibit high initial discharge and charge capacities of 1016.3 mAh g^{-1} and 784.4 mAh g^{-1} at 0.1 A g^{-1} within 1.0–3.0 V. Even under the current density of 1 A g^{-1}, the battery retained the capacity of 301.1 mAh g^{-1} for 500 cycles. This work demonstrates a promising active material with high specific capacity and long cycle life for all-solid-state lithium batteries.

Chapter 7. Conclusions

All-solid-state lithium batteries using inorganic solid electrolytes instead of organic electrolytes and separators can fundamentally solve the leakage problem and thermal runaway of traditional lithium-ion batteries. At the same time, lithium metal has low potential and a high theoretical specific capacity, which can be used as an anode material to improve the operate voltage and energy density of all-solid-state batteries. Therefore, all-solid-state lithium battery is the one of the most promising energy storage systems with high safety and high energy for the next generation.

Although the room-temperature lithium-ion conductivities of some sulfide solid electrolytes are close to or even higher than that of liquid electrolytes, due to the high charge transfer impedance of the solid-solid interface, all-solid-state lithium batteries still cannot achieve higher electrochemical performance. When the lithium intercalated transition metal oxide cathode comes into contact with the sulfide solid electrolyte, due to the large chemical potential difference between the transition metal sulfide cathodes and sulfide solid electrolytes, the lithium ions spontaneously migrate to the cathode materials, and a high-impedance space charge layer is formed. At the same time, sulfide solid electrolytes have a narrow electrochemical window, the side reaction would be occurred and

caused electrolyte decomposition when operate within higher voltage ranges. Moreover, the traditional lithium-intercalation based transition metal oxide cathodes have a low theoretical specific capacity, which cannot meet the requirements of high energy density.

In order to solve the above problems, the researchers attempted to apply transition metal sulfides as active materials into sulfide-based all-solid-state lithium batteries. On the one hand, the transition metal sulfide electrode has similar chemical composition and similar chemical potential with the sulfide solid electrolyte, and the contact with the sulfide solid electrolyte does not produce a serious space charge layer, showing good interfacial compatibility. Furthermore, transition metal polysulfide electrodes typically operate in a voltage range of less than 3.0 V, and lower operating voltages allow for a stable solid-solid interface. In addition, the transition metal sulfide electrode has a high theoretical specific capacity, which helps to meet the demand for high-energy-density all-solid-state lithium batteries. However, the charge transfer at the interface between the transition metal sulfide electrode and the sulfide solid electrolyte is a key factor restricting the electrochemical performance of all-solid-state lithium batteries. In addition, the transition metal sulfide electrode will undergo a large volume change during the charging and discharging process, resulting in the concentration of stress/strain at the interface,

electrode pulverization, and electrolyte cracks, which in turn causes the all-solid-state lithium battery to exhibit poor cycling stability. Therefore, through reasonable material design, a good electronic/ionic conductive network and a stable structure are constructed inside the composite electrode, which is conducive to achieving higher and more stable electrochemical performance.

MoS_6 has been considered as one of promising cathode materials for all-solid-state lithium battery because of its ultra-high theoretical specific capacity of 1117 mAh g^{-1} due to the high S_2^{2-} content as well as amorphous nature, which possess open and random transmission path to achieve cycling stability, therefore showing potential applications in high energy all-solid-state battery. The electronic structure of the S_2^{2-} group allows them to donate or receive electrons. Their ability as donors is attributed to the π^*_g orbital, which can release electrons that convert S_2^{2-} to S^{2-}. Because of the reversible reaction of $S_2^{2-} + 2e^- \rightarrow 2S^{2-}$, multi-electron reactions proceed during charge/discharge process, resulting in a high specific capacity. In addition, transition metal sulfides with anionic redox driven chemistry display a high voltage plateau of about 2 V, which is close to that of lithium-sulfur batteries.

By coating $Li_7P_3S_{11}$ solid electrolytes on the MoS_6, the resultant MoS_6@15%$Li_7P_3S_{11}$ composite can achieve an improved ion

diffusion coefficient range of 10^{-11}–10^{-10} cm^2 s^{-1}, which is higher than the value of MoS_6 with 10^{-12}–10^{-11} cm^2 s^{-1}. The $Li/Li_6PS_5Cl/MoS_6@15\%Li_7P_3S_{11}$ all-solid-sate lithium batteries show a high initial discharge capacity of 1083.8 mAh g^{-1} at 0.1 A g^{-1} and long cycle life of 1000 cycles under 1A g^{-1} at 25 °C. Besides, the $MoS_6@15\%Li_7P_3S_{11}$ composite displays a high energy density of 588 Wh kg^{-1} and power density of 1358 W kg^{-1} based on the total cathode layer. This contribution provides a new sulfide-based cathode material with high specific capacity and superior ion diffusion coefficient, showing promising application potential for all-solid-state lithium batteries.

Doping halide into active materials is an effectively strategy to improve the electrochemical performances. The redox kinetics of Li_2S/S can be enhanced by LiI-LiBr compound due to the reduced interaction between Li^+ and S^{2-}, thus improve the utilization of active materials. In addition, LiI also can improve the cycling performances of Li_2S when using in all-solid-state lithium battery. Therefore, it is anticipated that doping LiI into MoS_6 could efficiently improve the electrochemical reaction kinetics, and thus realize high specific capacity and cycle life. $95MoS_6{\cdot}5LiI$ composite is designed as the active material for all-solid-state batteries. The average ion diffusion coefficient of $95MoS_6{\cdot}5LiI$ shows the value of 1.23×10^{-10} cm^2 s^{-1},

which is twice higher than that of MoS_6 with 5.03×10^{-11} cm^2 s^{-1}. Benefitting from the impressive improved electrochemical reaction kinetics within cathode layer, the Li/Li_6PS_5Cl/95MoS_6·5LiI all-solid-state battery displays initial discharge and charge capacities of 1016.3 and 784.4 mAh g^{-1} at 0.1 A g^{-1} within 1.0–3.0 V. Besides, the all-solid-state battery with 95MoS_6·5LiI can realize superior cycle life of 500 cycles with high reversible specific capacity of 301.1 mAh g^{-1} at 1 A g^{-1}. This work demonstrates a promising active material with high specific capacity and long cycle life for all-solid-state lithium batteries.

Chapter 8. Future works

Compared with the traditional lithium-intercalation based transition metal oxide electrode, the transition metal sulfide electrode possesses better interfacial compatibility and higher theoretical specific capacity, which is expected to meet the needs of high-safety and high-energy all-solid-state lithium batteries. In order to further improve the electrochemical performance, the composite materials were synthesized with special morphology and structure through reasonable material design, and successfully applied them as active materials in all-solid-state lithium batteries. By ball milling with halides, the diffusivity of the composite electrode can be improved, and the volume change of the electrode during cycling can be mitigated. Then, the solid electrolyte nanoparticles are *in-situ* coated by the liquid-phase method, which can improve the solid-solid interface contact and increase the charge transfer kinetics at the microscopic scale. This kind of material shows good electrochemical performance in prototype batteries, and its electrochemical properties in pouch batteries need to be further explored to meet the requirements of practical applications. This work provides a possible direction for the development of high-capacity all-solid-state lithium battery cathode materials.

Of course, there are several limitations in the preparation

process and structural stability of transition metal sulfide composite cathode like MoS_6, which need to be further improved. Micro-size materials and their composites have a low specific surface area, which leads to poor interfacial contact and is difficult to obtain the performances under high charge rate. How to quickly and easily synthesize transition metal sulfide electrode materials with high-capacity, as well as improve the electronic/ionic conductivity and structural stability is an important research direction to achieve high-energy-density all-solid-state lithium batteries.

Understanding the mechanisms underlying the operation and degradation of MoS_6 in all-solid-state batteries is essential in advancing energy storage technology. The complex interplay between structural stability, ion diffusion kinetics, redox reactions, and electrochemical/electronic conductivity within MoS_6 impacts capacity, rate capability, and cycle life of the whole battery. Based on these comprehensions on MoS_6 properties, the optimized battery system would be designed, which would possess high capacity and long cycle life even in the extremely operating conditions.

Furthermore, all-solid-state lithium secondary batteries employing sulfide-based cathode materials hold great promise for future industrial applications due to their potential to address key challenges faced by conventional lithium-ion batteries, such as safety

concerns, energy density limitations, and cycle life improvements. Sulfide-based electrolytes offer high ionic conductivity and better compatibility with both lithium metal anodes and high-voltage cathodes compared with oxide cathode materials, making them particularly attractive for next-generation battery technologies.

Industrial outlook for these batteries indicates a gradual yet steady progression towards mass production and commercial viability. Research efforts have led to significant strides in optimizing the synthesis and processing of sulfide-based solid electrolytes, enhancing their mechanical properties, and ensuring stable interfaces with electrodes. Moreover, advances in scalable manufacturing processes, such as innovative casting and coating techniques, are helping to overcome the challenge of fabricating reliable and hermetic all-solid-state battery cells.

Recent breakthroughs have demonstrated improved electrochemical performance, including high capacity retention, reduced resistance, and enhanced thermal stability. Additionally, prototypes and pilot-scale production lines have been established to test the feasibility of manufacturing sulfur-based cathode-containing all-solid-state lithium-ion batteries, paving the way for larger-scale production and integration into electric vehicles, grid storage, and portable electronic devices.

However, the all-solid-state batteries still confront numerous technical problems, which limits the widespread adoption of all-solid-state batteries. These issues include achieving consistent fabrication quality across large batches, maintaining uniformity of the solid electrolyte and electrode layers, and reducing costs associated with raw materials and manufacturing processes. Despite these challenges are existing, ongoing research and development, backed by increasing investment from both academia and industry, suggests a bright future for sulfide-based all-solid-state lithium-ion batteries, positioning them as a transformative solution in the global pursuit of safer, more efficient, and sustainable energy storage solutions.

Bibliography

1. Armand, M. and J.M. Tarascon, *Building better batteries.* Nature, 2008. **451**(7179): p. 652-657.
2. Horiba, T., *Lithium-Ion Battery Systems.* Proceedings of the Ieee, 2014. **102**(6): p. 939-950.
3. Zhao, X.C., et al., *Electrochemical-thermal modeling of lithium plating/stripping of Li (Ni0.6Mn0.2Co0.2)O-2/Carbon lithium-ion batteries at subzero ambient temperatures.* Journal of Power Sources, 2019. **418**: p. 61-73.
4. Vetter, J., et al., *Ageing mechanisms in lithium-ion batteries.* Journal of Power Sources, 2005. **147**(1-2): p. 269-281.
5. Momma, T., et al., *Ac impedance analysis of lithium ion battery under temperature control.* Journal of Power Sources, 2012. **216**: p. 304-307.
6. Sagane, F., et al., *In-situ scanning electron microscopy observations of Li plating and stripping reactions at the lithium phosphorus oxynitride glass electrolyte/Cu interface.* Journal of Power Sources, 2013. **225**: p. 245-250.
7. Mu, Y.B., et al., *Highly Efficient Aligned Ion-Conducting Network and Interface Chemistries for Depolarized All-Solid-State Lithium Metal Batteries.* Nano-Micro Letters, 2024. **16**(1): p. 86.

8. Chen, Q., et al., *A study of environmental pollution and risk of heavy metals in the bottom water and sediment of the Chaohu Lake, China.* Environmental Science and Pollution Research, 2024. **31**: p. 19658-19673.

9. Adelaïde, L., et al., *Environmental and social inequities in continental France: an analysis of exposure to heat, air pollution, and lack of vegetation.* Journal of Exposure Science and Environmental Epidemiology, 2024: p. 1-11.

10. Fida, M., et al., *Review of Groundwater Nitrate Pollution from Municipal Landfill Leachates: Implications for Environmental and Human Health and Leachate Treatment Technologies.* Exposure and Health, 2024: p. 1-25.

11. Kucbel, M., et al., *Environmental impact assessment of the coal yard and ambient pollution.* Environmental Science and Pollution Research, 2024: p. 1-18.

12. Kumari, K.A., et al., *Platycladus Orientalis mediated green synthesis of crystalline palladium nanoparticles as a potential and promising nano catalyst in the degradation of dyes for mitigation of environmental pollution.* Inorganic and Nano-Metal Chemistry, 2024: p. 1-10.

13. Zhang, T. and F.Z. Zhao, *A study on the relationships among green finance, environmental pollution and economic*

development. Energy Strategy Reviews, 2024. **51**: p. 101290.

14. Nunez, Y., et al., *An environmental justice analysis of air pollution emissions in the United States from 1970 to 2010.* Nature Communications, 2024. **15**(1): p. 268.
15. Lu, C. and Q.J. Ouyang, *Environmental regulation and urban position in the inter-urban pollution transfer network: A perspective on network analysis of pollution-intensive enterprises' relocation.* Journal of Cleaner Production, 2024. **435**: p. 140418.
16. Chen, X.L., et al., *Development and evaluation of an online home energy management strategy for load coordination in smart homes with renewable energy sources.* Energy, 2024. **290**: p. 130134.
17. Fang, L., B. Hu, and F. Sher, *Renewable energy consumption - financial globalization-tourism nexus with nonlinearity and cross-sectional dependence during Asia's carbon-free transition.* Environmental Science and Pollution Research, 2024. **31**(12): p. 18435-18447.
18. Jiang, Y.Z., et al., *Do renewable energy, environmental regulations and green innovation matter for China's zero carbon transition: Evidence from green total factor productivity.* Journal of Environmental Management, 2024.

352: p. 120030.

19. Khan, K.A., et al., *Climate policy uncertainty and renewable energy consumption at crossroads: designing SDG policies for the United States.* International Journal of Sustainable Development and World Ecology, 2024. **31**(5): p. 593-610.
20. Ahmad, I. and D. Basu, *Electrochemical Treatment of Reactive Orange 16 Dye Pollutant Using Microbial Fuel Cell as Renewable Power Source.* Environmental Engineering Science, 2023. **41**(1): p. 29-38.
21. Sharlaev, A.S., et al., *Materials Based on Vanadium Oxide Nanofibers for Electrodes in Electrochemical Power Sources.* Russian Journal of Electrochemistry, 2022. **58**(5): p. 411-417.
22. Sailapu, S.K. and C. Menon, *Engineering Self-Powered Electrochemical Sensors Using Analyzed Liquid Sample as the Sole Energy Source.* Advanced Science, 2022. **9**(29): p. 2203690.
23. Rodin, V., et al., *Techno-economic evaluation of the electrochemical production of renewable ethylene oxide from fluctuating power sources and CO_2.* Journal of Co2 Utilization, 2023. **78**: p. 102554.
24. Maia, B.A., et al., *Cathodes pinpoints for the next generation of energy storage devices: the $LiFePO_4$ case study.* Journal of

Physics-Materials, 2024. **7**(2): p. 025001.

25. Zhang, Y., et al., *Surface Modification Improves Spinel $LiCoO_2$ Li-Ion Battery Cathode Materials Grown by Low Temperature Solvothermal Flow Reaction.* Journal of the Electrochemical Society, 2024. **171**(1): p. 010531.
26. He, J.Y., et al., *Enhanced high-temperature electrochemical properties of in situ carbon-coated truncated octahedral $LiMn_2O_4$ cathodes.* Chemical Communications, 2023. **59**(87): p. 13050-13053.
27. Abharana, N., et al., *Deciphering structural changes in $LiNi_xMn_yCo_zO_2$ cathodes of Li ion batteries during cycling: Experimental and theoretical investigations.* Solid State Ionics, 2023. **398**: p. 116270.
28. Zhao, W.G., et al., *Optimized Al Doping Improves Both Interphase Stability and Bulk Structural Integrity of Ni-Rich NMC Cathode Materials.* Acs Applied Energy Materials, 2020. **3**(4): p. 3369-3377.
29. Bruce, P.G., et al., *Li-O_2 and Li-S batteries with high energy storage.* Nature Materials, 2012. **11**(2): p. 19-29.
30. Kato, Y., et al., *High-power all-solid-state batteries using sulfide superionic conductors.* Nature Energy, 2016. **1**(4): p. 1-7.

31. Yi, Y.K., et al., *Progress and Prospect of Practical Lithium-Sulfur Batteries Based on Solid-Phase Conversion.* Batteries-Basel, 2023. **9**(1): p. 27.

32. Shi, C.M., et al., *All-Solid-State Garnet Type Sulfurized Polyacrylonitrile/Lithium-Metal Battery Enabled by an Inorganic Lithium Conductive Salt and a Bilayer Electrolyte Architecture.* Acs Energy Letters, 2023: p. 1803-1810.

33. Zhao, J.Y., et al., *Enabling All-Solid-State Lithium-Carbon Dioxide Battery Operation in a Wide Temperature Range.* Acs Nano, 2024. **18**(6): p. 5132-5140.

34. Choi, J., et al., *Revealing interfacial parasitic reactions of nitrile rubber binders in all-solid-state lithium batteries.* Journal of Materials Chemistry A, 2024. **12**(11): p. 6426-6437.

35. Chakraborty, T., et al., *Computational discovery of superior vanadium-niobate-based cathode materials for next-generation all-solid-state lithium-ion battery applications.* Journal of Materials Chemistry A, 2024. **12**(17): p. 10059-10071.

36. Boulineau, S., et al., *Mechanochemical synthesis of Li-argyrodite Li_6PS_5X (X= Cl, Br, I) as sulfur-based solid electrolytes for all solid state batteries application.* Solid State Ionics, 2012. **221**: p. 1-5.

37. Asano, S., et al., *Formation Processes of a Solid Electrolyte Interphase at a Silicon/Sulfide Electrolyte Interface in a Model All-Solid-State Li-Ion Battery.* Acs Applied Materials & Interfaces, 2024. **16**(6): p. 7189-7199.

38. Manthiram, A., X.W. Yu, and S.F. Wang, *Lithium battery chemistries enabled by solid-state electrolytes.* Nature Reviews Materials, 2017. **2**(4): p. 16103.

39. Acord, K.A., et al., *Manipulating ionic conductivity through chemical modifications in solid-state electrolytes prepared with binderless laser powder bed fusion processing.* Journal of Physics-Energy, 2024. **6**(2): p. 025006.

40. Bertoli, L., et al., *Unconventional PEO-PPC quasi-solid state blend polymer electrolyte for high efficiency solid-state Li-metal batteries.* Journal of Energy Storage, 2024. **81**: p. 110456.

41. Jiao, X.X., et al., *Viability of all-solid-state lithium metal battery coupled with oxide solid-state electrolyte and high-capacity cathode.* Journal of Energy Chemistry, 2024. **91**: p. 122-131.

42. Ohta, N., et al., *Enhancement of the high-rate capability of solid-state lithium batteries by nanoscale interfacial modification.* Advanced Materials, 2006. **18**(17): p. 2226-2229.

43. An, Z.G., et al., *Cooling and preheating performance of dual-active lithium-ion battery thermal management system under harsh conditions.* Applied Thermal Engineering, 2024. **242**: p. 122421.

44. Jiang, Z.Y., et al., *Experimental study on 18650 lithium-ion battery-pack cooling system composed of heat pipe and reciprocating air flow with water mist.* International Journal of Heat and Mass Transfer, 2024. **222**: p. 125171.

45. Sankar, T.K., Abhilash, and P. Meshram, *Environmental Impact Assessment in the Entire Life Cycle of Lithium-Ion Batteries.* Reviews of Environmental Contamination and Toxicology, 2024. **262**(1): p. 5.

46. Shang, Y.L., et al., *An Intelligent Preheating Approach Based on High-Gain Control for Lithium-Ion Batteries in Extremely Cold Environment.* Ieee Transactions on Industrial Electronics, 2024. **71**(5): p. 4697-4706.

47. Shen, J.W., et al., *Accurate state of temperature estimation for Lithium-Ion batteries based on square root cubature Kalman filter.* Applied Thermal Engineering, 2024. **242**: p. 122452.

48. Shi, G.C., et al., *Green regeneration and high-value utilization technology of the electrolyte from spent lithium-ion batteries.* Separation and Purification Technology, 2024. **335**: p. 126144.

49. Zhang, G.X., W. Shen, and X.Z. Wei, *Lithium-ion battery thermal safety evolution during high-temperature nonlinear aging.* Fuel, 2024. **362**: p. 130845.

50. Zhang, R.R., et al., *Unraveling the Fundamental Mechanism of Interface Conductive Network Influence on the Fast-Charging Performance of SiO-Based Anode for Lithium-Ion Batteries.* Nano-Micro Letters, 2024. **16**(1): p. 43.

51. Kato, Y., et al., *Discharge Performance of All-Solid-State Battery Using a Lithium Superionic Conductor $Li_{10}GeP_2S_{12}$.* Electrochemistry, 2012. **80**(10): p. 749-751.

52. Hennequart, B., et al., *Solid-Electrolyte-Free O3-Li_xTiS_2 Cathode for High-Energy-Density All-Solid-State Lithium-Metal Batteries.* Acs Applied Energy Materials, 2023. **6**(16): p. 8521-8531.

53. Hong, S.B., et al., *Exploring the Cathode Active Materials for Sulfide-Based All-Solid-State Lithium Batteries with High Energy Density.* Small, 2024. **20**(9): p. 2304747.

54. Jung, Y.C., et al., *On-site formation of silver decorated carbon as an anodeless electrode for high-energy density all-solid-state batteries.* Journal of Materials Chemistry A, 2023. **11**(46): p. 25275-25282.

55. Pan, W.L., et al., *An Electron/Ion Dual Conductive Integrated*

Cathode Using Cationic/Anionic Redox for High-Energy-Density All-Solid-State Lithium-Sulfur Batteries. Batteries & Supercaps, 2024. **7**(1): p. e202300427.

56. Sugimoto, R., M. Inaba, and T. Doi, *Nanostructure of Si-Sn Thick-Film Electrodes to Improve the Energy Density of Oxide-Based All-Solid-State Lithium-Ion Batteries.* Journal of the Electrochemical Society, 2023. **170**(11): p. 110504.

57. Tanibata, N., et al., *Chloride electrode composed of ubiquitous elements for high-energy-density all-solid-state sodium-ion batteries.* Scientific Reports, 2024. **14**(1): p. 2703.

58. Zheng, R. and C. Kim, *Improving the energy density of all-solid-state batteries by maximizing the contact area between the solid electrolyte and electrode, and stress issues.* Journal of Mechanical Science and Technology, 2023. **37**(8): p. 4149-4157.

59. Wang, N., et al., *A flexible PEO-based polymer electrolyte with cross-linked network for high-voltage all solid-state lithium-ion battery.* Journal of Materials Science & Technology, 2024. **183**: p. 206-214.

60. Liang, H.M., et al., *Tailoring Practically Accessible Polymer/Inorganic Composite Electrolytes for All-Solid-State Lithium Metal Batteries: A Review.* Nano-Micro Letters, 2023.

15(1): p. 42.

61. Lee, Y.J., et al., *Flexible and thin sulfide-based solid electrolyte sheet with Li plus -ion conductive polymer network for all-solid-state lithium-ion batteries.* Chemical Engineering Journal, 2023. **477**: p. 146983.

62. Du, X.Y., et al., *Self-healing polyurethane-based polymer electrolyte with high strength for all-solid-state lithium metal batteries.* Colloids and Surfaces a-Physicochemical and Engineering Aspects, 2024. **680**: p. 132703.

63. Li, C.H., et al., *Porous polyamine/PEO composite solid electrolyte for high performance solid-state lithium metal batteries.* Journal of Materials Chemistry A, 2021. **9**(43): p. 24661-24669.

64. Thackeray, M.M. and J. Coetzer, *Electrical-Conductivity of Polyamine Iodide Silver Iodide Solid Electrolytes.* Electrochimica Acta, 1979. **24**(5): p. 495-502.

65. Del Rio, C., P.J. Martin-Alvarez, and J.L. Acosta, *Conductivity studies of solid polymer electrolytes based on polyethers and polyphosphazene blends.* Journal of Applied Polymer Science, 1998. **70**(11): p. 2181-2186.

66. Liu, T.M., et al., *High ion-conducting solid polymer electrolytes based on blending hybrids derived from*

monoamine and diamine polyethers for lithium solid-state batteries. Rsc Advances, 2017. **7**(33): p. 20373-20383.

67. Cai, J.X., et al., *PVDF-HFP/LiTFSI based composite solid state electrolyte with different micromorphology of Li6.25Ga0.25La3Zr2O12 doping.* Journal of Alloys and Compounds, 2023. **968**: p. 171872.

68. Olana, B.N., et al., *Understanding the formation chemistry of native solid electrolyte interphase over lithium anode and its implications using a LiTFSI/TME-TTE electrolyte and polysulfide additive.* Journal of Materials Chemistry A, 2024. **12**(6): p. 3659-3670.

69. Liu, R., et al., *Nanocomposite polymer electrolytes for solid-state lithium-ion batteries with enhanced electrochemical properties.* Journal of Applied Polymer Science, 2023. **140**(3): p. e53337.

70. Wang, Z.Y., et al., *10 μm-Thick High-Strength Solid Polymer Electrolytes with Excellent Interface Compatibility for Flexible All-Solid-State Lithium-Metal Batteries.* Advanced Materials, 2021. **33**(25): p. 2100353.

71. Kim, S.H., et al., *Functional Sulfate Additive-Derived Interfacial Layer for Enhanced Electrochemical Stability of PEO-Based Polymer Electrolytes.* Small, 2024. **20**(23): p.

2309160.

72. Li, B.X., et al., *A promising composite room temperature solid electrolyte via incorporating LLZTO into cross-linked ETPTA/PEO/SN matrix for all solid state lithium batteries.* Ionics, 2024. **30**(4): p. 2007-2017.

73. Ma, F.R., et al., *Hybrid solid electrolyte with the combination of LATP ceramic and PEO polymer by a solvent-free procedure.* Solid State Ionics, 2024. **405**: p. 116450.

74. MacGlashan, G.S., Y.G. Andreev, and P.G. Bruce, *Structure of the polymer electrolyte poly(ethylene oxide):LiAsF.* Nature, 1999. **398**(6730): p. 792-794.

75. Zhang, H., et al., *Single lithium-ion conducting solid polymer electrolytes: advances and perspectives.* Chemical Society Reviews, 2017. **46**(3): p. 797-815.

76. Guzman-Torres, J., et al., *Solid polymer electrolyte based on PEO/PVDF/Mg(ClO$_4$)$_2$-[EMIM][ESO$_4$] system for rechargeable magnesium ion batteries.* Ionics, 2023. **29**(6): p. 2341-2349.

77. Carlsson, P., et al., *Neutron-scattering studies of a polymer electrolyte, PPO-LiClO.* Solid State Ionics, 1998. **113**: p. 139-147.

78. Kufian, M.Z., S. Ramesh, and A.K. Arof, *PMMA-LiTFSI*

based gel polymer electrolyte for lithium-oxygen cell application. Optical Materials, 2021. **120**: p. 111418.

79. Tran, H.K., et al., *Composite Polymer Electrolytes Based on PVA/PAN for All-Solid-State Lithium Metal Batteries Operated at Room Temperature.* Acs Applied Energy Materials, 2020. **3**(11): p. 11024-11035.

80. Kim, C., et al., *Polymer electrolytes prepared by polymerizing mixtures of polymerizable PEO-oligomers, copolymer of PVDC and poly(acrylonitrile), and lithium triflate.* Solid State Ionics, 1999. **123**(1-4): p. 251-257.

81. Cao, T.C., et al., *Chemomechanical Origins of the Dynamic Evolution of Isolated Li Filaments in Inorganic Solid-State Electrolytes.* Nano Letters, 2024. **24**(6): p. 1843-1850.

82. Kim, K.T., et al., *Ultrathin Superhydrophobic Coatings for Air-Stable Inorganic Solid Electrolytes: Toward Dry Room Application for All-Solid-State Batteries.* Advanced Energy Materials, 2023. **13**(43): p. 2301600.

83. Liang, X.H., et al., *Long-Cycle Stability of In Situ Ultraviolet Curable Organic/Inorganic Composite Electrolyte for Solid-State Batteries.* Polymers, 2024. **16**(1): p. 55.

84. Liu, P., et al., *Inorganic-Organic Hybrid Multifunctional Solid Electrolyte Interphase Layers for Dendrite-Free Sodium Metal*

Anodes. Angewandte Chemie-International Edition, 2023. **135**(47): p. e202312413.

85. Wang, S.H., et al., *Ultrathin All-Inorganic Halide Solid-State Electrolyte Membranes for All-Solid-State Li-Ion Batteries.* Advanced Energy Materials, 2024. **14**(6): p. 2303641.

86. Weeks, J.A., et al., *In Situ Engineering of Inorganic-Rich Solid Electrolyte Interphases via Anion Choice Enables Stable, Lithium Anodes.* Advanced Materials, 2024. **36**(9): p. 2305645.

87. Yu, Y.K., et al., *Kinetic pathways of fast lithium transport in solid electrolyte interphases with discrete inorganic components.* Energy & Environmental Science, 2023. **16**(12): p. 5904-5915.

88. Zhu, T., et al., *A Novel NASICON-Type $Na_{3.5}MnCr_{0.5}Ti_{0.5}(PO_4)_3$ Nanofiber with Multi-electron Reaction for High-Performance Sodium-Ion Batteries.* Advanced Fiber Materials, 2024. **6**(2): p. 561-569.

89. Kobayashi, T., et al., *All solid-state batteries using super ionic conductor, thio-lisicon - Electrode/electrolyte interfacial design.* Solid State Ionics-2004, 2005. **835**: p. 333-345.

90. Feng, X.Y., et al., *Garnet-type double-layer solid electrolyte for dendrite-free solid-state Li batteries.* Journal of Solid State Electrochemistry, 2023: p. 1-10.

91. Wang, P.F., et al., *Perovskite-Type $CsGeI_3$ as an Electrolyte Additive for All-Solid-State Lithium-Sulfur Batteries.* Energy & Fuels, 2023. **37**(19): p. 15198-15205.

92. Wu, M., et al., *In situ formed LiF-Li3N interface layer enables ultra-stable sulfide electrolyte-based all-solid-state lithium batteries.* Journal of Energy Chemistry, 2023. **79**: p. 272-278.

93. Busche, M.R., et al., *The Formation of the Solid/Liquid Electrolyte Interphase (SLEI) on NASICON-Type Glass Ceramics and LiPON.* Advanced Materials Interfaces, 2020. **7**(19): p. 2000380.

94. Hayashi, A. and M. Tatsumisago, *Invited Paper: Recent Development of Bulk-Type Solid-State Rechargeable Lithium Batteries with Sulfide Glass-ceramic Electrolytes.* Electronic Materials Letters, 2012. **8**(2): p. 199-207.

95. Hoinkis, N., et al., *Amorphous Phase Induced Lithium Dendrite Suppression in Glass-Ceramic Garnet-Type Solid Electrolytes.* Acs Applied Materials & Interfaces, 2023. **15**(23): p. 28692-28704.

96. Kriegler, J., et al., *Scaling up picosecond laser ablation of a LATGP-type glass-ceramic solid electrolyte for all-solid-state battery production.* Journal of Manufacturing Processes, 2023. **106**: p. 188-201.

97. Nagata, H. and J. Akimoto, *Excellent Deformable Oxide Glass Electrolytes and Oxide-Type All-Solid-State Li_2S-Si Batteries Employing These Electrolytes.* Acs Applied Materials & Interfaces, 2021. **13**(30): p. 35785-35794.

98. Patil, V., et al., *Structural and Electrical Properties of NASICON Type Solid Electrolyte Nanoscaled Glass-Ceramic Powder by Mechanical Milling for Thin Film Batteries.* Journal of Nanoscience and Nanotechnology, 2013. **13**(5): p. 3665-3668.

99. Xie, J., et al., *Li-ion transport in all-solid-state lithium batteries with $LiCoO_2$ using NASICON-type glass ceramic electrolytes.* Journal of Power Sources, 2009. **189**(1): p. 365-370.

100. Wu, J.H., et al., *Lithium/Sulfide All-Solid-State Batteries using Sulfide Electrolytes.* Advanced Materials, 2021. **33**(6): p. 2000751.

101. Bachman, J.C., et al., *Inorganic Solid-State Electrolytes for Lithium Batteries: Mechanisms and Properties Governing Ion Conduction.* Chemical Reviews, 2016. **116**(1): p. 140-162.

102. Muramatsu, H., et al., *Structural change of Li_2S-P_2S_5 sulfide solid electrolytes in the atmosphere.* Solid State Ionics, 2011. **182**(1): p. 116-119.

103. Kanno, R. and M. Maruyama, *Lithium ionic conductor thio-LISICON The Li_2S-GeS_2-P_2S_5 system.* Journal of the Electrochemical Society, 2001. **148**(7): p. A742-A746.

104. Kamaya, N., et al., *A lithium superionic conductor.* Nature Materials, 2011. **10**(9): p. 682-686.

105. Kondo, S., K. Takada, and Y. Yamamura, *New Lithium Ion Conductors Based on Li_2S-SiS_2 System.* Solid State Ionics, 1992. **53**: p. 1183-1186.

106. Hayashi, A., et al., *Preparation of Li_2S-P_2S_5 amorphous solid electrolytes by mechanical milling.* Journal of the American Ceramic Society, 2001. **84**(2): p. 477-479.

107. Zhang, Z.M. and J.H. Kennedy, *Synthesis and Characterization of the B_2S_3-Li_2S, the P_2S_5-Li_2S and the B_2S_3-P_2S_5-Li_2S Glass Systems.* Solid State Ionics, 1990. **38**(3-4): p. 217-224.

108. Tatsumisago, M., et al., *Superionic Conduction in Rapidly Quenched Li_2S-SiS_2-Li_3PO_4 Glasses.* Nippon Seramikkusu Kyokai Gakujutsu Ronbunshi-Journal of the Ceramic Society of Japan, 1993. **101**(11): p. 1315-1317.

109. Morimoto, H., et al., *Mechanochemical synthesis of the high lithium ion conductive amorphous materials in the systems Li_2S-SiS_2 and Li_2S-SiS_2-Li_4SiO.* Journal of the Ceramic Society

of Japan, 2000. **108**(2): p. 128-131.

110. Kennedy, J.H., et al., *Preparation and Conductivity Measurements of SiS_2-Li_2S Glasses Doped with LiBr and LiCl.* Solid State Ionics, 1986. **18-9**: p. 368-371.

111. Wada, H., et al., *Preparation and Ionic-Conductivity of New B_2S_3-Li_2S-LiI Glasses.* Materials Research Bulletin, 1983. **18**(2): p. 189-193.

112. Mercier, R., et al., *Superionic Conduction in Li_2S-P_2S_5-LiI-Glasses.* Solid State Ionics, 1981. **5**(Oct): p. 663-666.

113. Hayashi, A., et al., *Formation of superionic crystals from mechanically milled Li_2S-P_2S_5 glasses.* Electrochemistry Communications, 2003. **5**(2): p. 111-114.

114. Mizuno, F., et al., *New, highly ion-conductive crystals precipitated from Li_2S-P_2S_5 glasses.* Advanced Materials, 2005. **17**(7): p. 918-921.

115. Boulineau, S., et al., *Mechanochemical synthesis of Li-argyrodite Li6PS5X(X= Cl, Br, I) as sulfur-based solid electrolytes for all solid state batteries application.* Solid State Ionics, 2012. **221**: p. 1-5.

116. Han, A.G., et al., *Toward High-Quality Sulfide Solid Electrolytes: A Liquid-Phase Approach Featured with an Interparticle Coupled Unification Effect.* Small, 2024. **20**(23):

p. 2307997.

117. Li, M.L., et al., *Understanding the Stability of Copper Current Collector with Sulfide Electrolyte in All-Solid-State Batteries.* Advanced Energy Materials, 2024. **14**(7): p. 2303156.

118. Li, W.J., et al., *High-Entropy Argyrodite-Type Sulfide Electrolyte with High Conductivity and Electro-Chemo-Mechanical Stability for Fast-Charging All-Solid-State Batteries.* Advanced Functional Materials, 2024: p. 2312832.

119. Liu, F.Q., et al., *Interfacial Challenges, processing strategies, and composite applications for high voltage all-solid-state lithium batteries based on halide and sulfide solid-state electrolytes.* Energy Storage Materials, 2023: p. 13072.

120. Wu, Z., et al., *Interfaces in Sulfide Solid Electrolyte-Based All-Solid-State Lithium Batteries: Characterization, Mechanism and Strategy (vol 6, 10, 2023).* Electrochemical Energy Reviews, 2023. **6**(10): p. 1-41.

121. Yamaguchi, H., et al., *Structural analysis and ionic conduction mechanism of sulfide-based solid electrolytes doped with Br.* Scientific Reports, 2023. **13**(1): p. 16063.

122. Park, K.H., et al., *Design Strategies, Practical Considerations, and New Solution Processes of Sulfide Solid Electrolytes for All-Solid-State Batteries.* Advanced Energy Materials, 2018.

8(18): p. 1800035.

123. Xu, L., et al., *Interfaces in Solid-State Lithium Batteries.* Joule, 2018. **2**(10): p. 1991-2015.

124. Gupta, Y., et al., *Recent progress of layered structured $P^{2-}$and O^{3-}type transition metal oxides as cathode material for sodium-ion batteries.* Renewable & Sustainable Energy Reviews, 2024. **192**: p. 114167.

125. Kim, D., et al., *An oxygen-vacancy-boosted heterostructured catalyst with synergistically integrated dual transition-metal oxides for high-performance lithium-sulfur batteries.* Chemical Engineering Journal, 2024. **479**: p. 147820.

126. Kim, T., *Multifunctional Separator Enabled by a High Phosphorus Content Additive for Ni-Rich Transition Metal Oxide Batteries.* Acs Applied Energy Materials, 2023. **6**(20): p. 10487-10498.

127. Li, C.G., S. Nie, and H. Li, *Towards Efficient Polymeric Binders for Transition Metal Oxides-based Li-ion Battery Cathodes.* Chemistry-a European Journal, 2024. **30**(16): p. e202303733.

128. Li, H., et al., *Why the Synthesis Affects Performance of Layered Transition Metal Oxide Cathode Materials for Li-Ion Batteries.* Advanced Materials, 2024. **36**(16): p. 2312292.

129. Wang, H., et al., *Recent Advances on F-Doped Layered Transition Metal Oxides for Sodium Ion Batteries.* Molecules, 2023. **28**(24): p. 8065.

130. Zhang, T., et al., *Negative Lattice Expansion in an $O^{3'}$-Type Transition-Metal Oxide Cathode for Highly Stable Sodium-Ion Batteries.* Angewandte Chemie-International Edition, 2024. **63**(8): p. 202316949.

131. Kim, T., *Origin of over-cycling tolerance achieved by metal phosphate coating for transition metal oxide lithium-ion batteries.* Solid State Ionics, 2023. **389**: p. 116105.

132. Wang, Y. and F.Q. Yu, *Probing the morphology dependence, size preference and electron/ion conductance of manganese-based lithium transition-metal phosphate as cathode materials for high-performance lithium-ion battery.* Journal of Alloys and Compounds, 2021. **850**: p. 156773.

133. Zhang, D., et al., *Construction of uniform transition-metal phosphate nanoshells and their potential for improving Li-ion battery performance.* Journal of Materials Chemistry A, 2018. **6**(19): p. 8992-8999.

134. Zhang, G.H., et al., *Lithium Iron Phosphate and Layered Transition Metal Oxide Cathode for Power Batteries: Attenuation Mechanisms and Modification Strategies.*

Materials, 2023. **16**: p. 5769.

135. Maier, J., *Ionic-Conduction in-Space Charge Regions.* Progress in Solid State Chemistry, 1995. **23**(3): p. 171-263.

136. Ohta, N., et al., *$LiNbO_3$-coated $LiCoO_2$ as cathode material for all solid-state lithium secondary batteries.* Electrochemistry Communications, 2007. **9**(7): p. 1486-1490.

137. Sakuda, A., et al., *All-solid-state lithium secondary batteries with oxide-coated $LiCoO_2$ electrode and Li_2S-P_2S_5 electrolyte.* Journal of Power Sources, 2009. **189**(1): p. 527-530.

138. Sakuda, A., et al., *Modification of Interface Between $LiCoO_2$ Electrode and Li_2S-P_2S_5 Solid Electrolyte Using Li_2O-SiO_2 Glassy Layers.* Journal of the Electrochemical Society, 2009. **156**(1): p. A27-A32.

139. Woo, J.H., et al., *Nanoscale Interface Modification of $LiCoO_2$ by Al_2O_3 Atomic Layer Deposition for Solid-State Li Batteries.* Journal of the Electrochemical Society, 2012. **159**(7): p. A1120-A1124.

140. Sumita, M., et al., *Charged and Discharged States of Cathode/Sulfide Electrolyte Interfaces in All-Solid-State Lithium Ion Batteries.* Journal of Physical Chemistry C, 2016. **120**(25): p. 13332-13339.

141. Sakuda, A., et al., *All-solid-state Lithium Secondary Batteries*

Using Li_2S-P_2S_5 Solid Electrolytes and $LiFePO_4$ Electrode Particles with Amorphous Surface Layer. Chemistry Letters, 2012. **41**(3): p. 260-261.

142. Okumura, T., et al., *Depth-resolved X-ray absorption spectroscopic study on nanoscale observation of the electrode-solid electrolyte interface for all solid state lithium ion batteries.* Journal of Materials Chemistry, 2011. **21**(27): p. 10051-10060.

143. Xu, X.X., et al., *Self-Organized Core-Shell Structure for High-Power Electrode in Solid-State Lithium Batteries.* Chemistry of Materials, 2011. **23**(17): p. 3798-3804.

144. Peng, G., et al., *Insights on the fundamental lithium storage behavior of all-solid-state lithium batteries containing the $LiNi_{0.8}Co_{0.15}Al_{0.05}O_2$ cathode and sulfide electrolyte.* Journal of Power Sources, 2016. **307**: p. 724-730.

145. Yubuchi, S., et al., *5V class $LiNi_{0.5}Mn_{1.5}O_4$ positive electrode coated with Li_3PO_4 thin film for all-solid-state batteries using sulfide solid electrolyte.* Solid State Ionics, 2016. **285**: p. 79-82.

146. Oh, G., et al., *Bulk-Type All Solid-State Batteries with 5 V Class $LiNi_{0.5}Mn_{1.5}O_4$ Cathode and $Li_{10}GeP_2S_{12}$ Solid Electrolyte.* Chemistry of Materials, 2016. **28**(8): p. 2634-2640.

147. Feng, X.Q., et al., *Transition Metal Chalcogenide Cathode Materials Applied in Aluminum-Ion Batteries.* Progress in Chemistry, 2022. **34**(2): p. 319-327.

148. Liu, X., et al., *Current material design strategies on the copper chalcogenide cathodes for rechargeable magnesium batteries: a review.* Materials Chemistry Frontiers, 2023. **7**(19): p. 4400-4419.

149. Trumbore, F.A., Broadhea.J, and Putvinsk.Tm, *Transition-Metal Chalcogenide Cathode Materials for Lithium-Nonaqueous Batteries.* Journal of the Electrochemical Society, 1973. **120**(8): p. C229-C229.

150. Wang, S.X. and X.Y. Zhao, *Minireview on Metal-Chalcogenide Cathode Materials with Dual-Redox Centers for Magnesium-Metal-Anode-Based Batteries: Recent Progress and Future Directions.* Energy & Fuels, 2023. **37**(23): p. 18441-18455.

151. Zhang, H., et al., *Evidence for dual anions co-insertion in a transition metal chalcogenide cathode material NiSe for high-performance rechargeable aluminum-ion batteries.* Energy Storage Materials, 2022. **47**: p. 336-344.

152. Liu, Q., et al., *Building composite of layered yttrium hydroxide and carbon nanotube as the sulfur host for high-performance*

lithium-sulfur batteries. Journal of Energy Storage, 2024. **81**: p. 110479.

153. Liu, X.H., et al., *In situ reduction growth Sn-MoS2 on CNFs as advanced separator coating for improved-performance lithium sulfur batteries.* Journal of Alloys and Compounds, 2024. **979**: p. 173432.

154. Wu, X.P., et al., *Engineering Defect-Rich Bimetallic Telluride with Dense Heterointerfaces for High-Performance Lithium-Sulfur Batteries.* Advanced Functional Materials, 2024: p. 2315012.

155. Manthiram, A., Y.Z. Fu, and Y.S. Su, *Challenges and Prospects of Lithium-Sulfur Batteries.* Accounts of Chemical Research, 2013. **46**(5): p. 1125-1134.

156. Li, G.R., et al., *Revisiting the Role of Polysulfides in Lithium-Sulfur Batteries.* Advanced Materials, 2018. **30**(22): p. 1705590.

157. Yin, Y.X., et al., *Lithium-Sulfur Batteries: Electrochemistry, Materials, and Prospects.* Angewandte Chemie-International Edition, 2013. **52**(50): p. 13186-13200.

158. Lin, Z. and C.D. Liang, *Lithium-sulfur batteries: from liquid to solid cells.* Journal of Materials Chemistry A, 2015. **3**(3): p. 936-958.

159. Yue, J.P., et al., *Progress of the Interface Design in All-Solid-State Li-S Batteries.* Advanced Functional Materials, 2018. **28**(38): p. 1707533.

160. Yu, X.W. and A. Manthiram, *Electrode-Electrolyte Interfaces in Lithium-Sulfur Batteries with Liquid or Inorganic Solid Electrolytes.* Accounts of Chemical Research, 2017. **50**(11): p. 2653-2660.

161. Hayashi, A., et al., *All-solid-state Li/S batteries with highly conductive glass-ceramic electrolytes.* Electrochemistry Communications, 2003. **5**(8): p. 701-705.

162. Hayashi, A., et al., *All-solid-state rechargeable lithium batteries with Li_2S as a positive electrode material.* Journal of Power Sources, 2008. **183**(1): p. 422-426.

163. Kobayashi, T., et al., *All solid-state battery with sulfur electrode and thio-LISICON electrolyte.* Journal of Power Sources, 2008. **182**(2): p. 621-625.

164. Nagao, M., et al., *All-solid-state Li-sulfur batteries with mesoporous electrode and thio-LISICON solid electrolyte.* Journal of Power Sources, 2013. **222**: p. 237-242.

165. Nagao, M., A. Hayashi, and M. Tatsumisago, *Sulfur-carbon composite electrode for all-solid-state Li/S battery with Li_2S-P_2S_5 solid electrolyte.* Electrochimica Acta, 2011. **56**(17): p.

6055-6059.

166. Nagao, M., A. Hayashi, and M. Tatsumisago, *High-capacity Li_2S-nanocarbon composite electrode for all-solid-state rechargeable lithium batteries.* Journal of Materials Chemistry, 2012. **22**(19): p. 10015-10020.

167. Li, X.N., et al., *High-performance all-solid-state Li-Se batteries induced by sulfide electrolytes.* Energy & Environmental Science, 2018. **11**(10): p. 2828-2832.

168. Yao, X.Y., et al., *High-Performance All-Solid-State Lithium-Sulfur Batteries Enabled by Amorphous Sulfur-Coated Reduced Graphene Oxide Cathodes.* Advanced Energy Materials, 2017. **7**(17): p. 1602923.

169. Lin, Z., et al., *Lithium Superionic Sulfide Cathode for All-Solid Lithium-Sulfur Batteries.* Acs Nano, 2013. **7**(3): p. 2829-2833.

170. Hakari, T., A. Hayashi, and M. Tatsumisago, *Li_2S-Based Solid Solutions as Positive Electrodes with Full Utilization and Superlong Cycle Life in All-Solid-State Li/S Batteries.* Advanced Sustainable Systems, 2017. **1**(6): p. 1700017.

171. Han, F.D., et al., *High-Performance All-Solid-State Lithium-Sulfur Battery Enabled by a Mixed-Conductive Li_2S Nanocomposite.* Nano Letters, 2016. **16**(7): p. 4521-4527.

172. Grayfer, E.D., et al., *Anionic Redox Chemistry in Polysulfide*

Electrode Materials for Rechargeable Batteries. ChemSusChem, 2017. **10**(24): p. 4805-4811.

173. Sakuda, A., et al., *Amorphous Metal Polysulfides: Electrode Materials with Unique Insertion/Extraction Reactions.* Journal of the American Chemical Society, 2017. **139**(26): p. 8796-8799.

174. Wang, T.S., et al., *Nickel Disulfide-Graphene Nanosheets Composites with Improved Electrochemical Performance for Sodium Ion Battery.* Acs Applied Materials & Interfaces, 2016. **8**(12): p. 7811-7817.

175. Arsentev, M., et al., *TiS_3 Magnesium Battery Material: Atomic-Scale Study of Maximum Capacity and Structural Behavior.* Journal of Physical Chemistry C, 2017. **121**(29): p. 15509-15515.

176. Dong, S.W., et al., *Challenges and Prospects of All-Solid-State Electrodes for Solid-State Lithium Batteries.* Advanced Functional Materials, 2023: p. 2304371.

177. Chong, P.D., et al., *The Stabilizing of 1T-MoS_2 for All-Solid-State Lithium-Ion Batteries.* Batteries-Basel, 2023. **9**(1): p. 26.

178. Zhang, Y.B., et al., *High Capacity, Superior Cyclic Performances in All-Solid-State Lithium-Ion Batteries Based on $78Li_2S$-$22P_2S_5$ Glass-Ceramic Electrolytes Prepared via*

Simple Heat Treatment. Acs Applied Materials & Interfaces, 2017. **9**(34): p. 28542-28548.

179. Yersak, T.A., et al., *Solid State Enabled Reversible Four Electron Storage.* Advanced Energy Materials, 2013. **3**(1): p. 120-127.

180. Hayashi, A., et al., *Amorphous Titanium Sulfide Electrode for All-solid-state Rechargeable Lithium Batteries with High Capacity.* Chemistry Letters, 2012. **41**(9): p. 886-888.

181. Matsuyama, T., et al., *Electrochemical properties of all-solid-state lithium batteries with amorphous titanium sulfide electrodes prepared by mechanical milling.* Journal of Solid State Electrochemistry, 2013. **17**(10): p. 2697-2701.

182. Choi, W., et al., *Recent development of two-dimensional transition metal dichalcogenides and their applications.* Materials Today, 2017. **20**(3): p. 116-130.

183. Choudhary, N., et al., *Two-dimensional transition metal dichalcogenide hybrid materials for energy applications.* Nano Today, 2018. **19**: p. 16-40.

184. Chakraborty, D., M. Pandey, and P. Johari, *2D Light-Weight Transition Metal Disulfide as Model Cathode for Alkali-Ion Batteries and Beyond.* Advanced Theory and Simulations, 2024. **7**(1): p. 2300486.

185. Choi, D.S., et al., *Polyselenide Anchoring Using Transition-Metal Disulfides for Enhanced Lithium-Selenium Batteries.* Inorganic Chemistry, 2018. **57**(4): p. 2149-2156.

186. Dong, Y.L., et al., *Insights into the Crystallinity of Layer-Structured Transition Metal Dichalcogenides on Potassium Ion Battery Performance: A Case Study of Molybdenum Disulfide.* Small, 2019. **15**(15): p. 1900497.

187. Eng, A.Y.S., J.L. Cheong, and S.S. Lee, *Controlled synthesis of transition metal disulfides (MoS_2 and WS_2) on carbon fibers: Effects of phase and morphology toward lithium-sulfur battery performance.* Applied Materials Today, 2019. **16**: p. 529-537.

188. Tan, C.L., et al., *Recent Advances in Ultrathin Two-Dimensional Nanomaterials.* Chemical Reviews, 2017. **117**(9): p. 6225-6331.

189. Chen, M.H., et al., *All-solid-state MoS_2/Li_6PS_5Br/In-Li batteries as a novel type of Li/S battery.* Journal of Materials Chemistry A, 2015. **3**(20): p. 10698-10702.

190. Xu, R.C., et al., *Rational coating of $Li_7P_3S_{11}$ solid electrolyte on MoS_2 electrode for all-solid-state lithium ion batteries.* Journal of Power Sources, 2018. **374**: p. 107-112.

191. Shin, B.R., et al., *Interfacial Architecture for Extra Li^+ Storage in All-Solid-State Lithium Batteries.* Scientific Reports, 2014.

4(1): p. 5572.

192. Shin, B.R., et al., *Comparative Study of TiS_2/Li-In All-Solid-State Lithium Batteries Using Glass-Ceramic Li_3PS_4 and $Li_{10}GeP_2S_{12}$ Solid Electrolytes.* Electrochimica Acta, 2014. **146**: p. 395-402.

193. Oh, D.Y., et al., *All-solid-state lithium-ion batteries with TiS_2 nanosheets and sulphide solid electrolytes.* Journal of Materials Chemistry A, 2016. **4**(26): p. 10329-10335.

194. Cai, L.T., et al., *Highly Crystalline Layered VS_2 Nanosheets for All-Solid-State Lithium Batteries with Enhanced Electrochemical Performances.* Acs Applied Materials & Interfaces, 2018. **10**(12): p. 10053-10063.

195. Cai, L., et al., *Highly Crystalline Layered VS_2 Nanosheets for All-Solid-State Lithium Batteries with Enhanced Electrochemical Performances.* ACS Appl Mater Interfaces, 2018. **10**(12): p. 10053-10063.

196. Cui, Y.C., et al., *Binary Transition-Metal Sulfides/MXene Synergistically Promote Polysulfide Adsorption and Conversion in Lithium-Sulfur Batteries.* Acs Applied Materials & Interfaces, 2023. **15**(42): p. 49223-49232.

197. Whang, G. and W.G. Zeier, *Transition Metal Sulfide Conversion: A Promising Approach to Solid-State Batteries.*

Acs Energy Letters, 2023. **8**(12): p. 5264-5274.

198. Chen, M., R.P. Rao, and S. Adams, *The unusual role of Li_6PS_5Br in all-solid-state $CuS/Li_6PS_5Br/In$-Li batteries.* Solid State Ionics, 2014. **268**: p. 300-304.

199. Nagao, M., et al., *High Rate Performance, Wide Temperature Operation and Long Cyclability of All-Solid-State Rechargeable Lithium Batteries Using Mo-S Cheviel-Phase Compound.* Journal of the Electrochemical Society, 2013. **160**(6): p. A819-A823.

200. Yao, X., et al., *High-Energy All-Solid-State Lithium Batteries with Ultralong Cycle Life.* Nano Lett, 2016. **16**(11): p. 7148-7154.

201. Chen, K.Y., et al., *Exfoliated few-layered graphite anode with broadened delithiation voltage plateau and fast charging performance for lithium-ion batteries.* Journal of Solid State Electrochemistry, 2024: p. 1-11.

202. Hofmann, K., et al., *Effect of mechanical properties on processing behavior and electrochemical performance of aqueous processed graphite anodes for lithium-ion batteries.* Journal of Power Sources, 2024. **593**: p. 233996.

203. Jolley, M.J., et al., *Investigating the effect of the degree of cross-linking in styrene butadiene rubber on the performance*

of graphite anodes for the use in lithium-ion batteries. Journal of Applied Polymer Science, 2024. **141**(12): p. e55135.

204. Scheck, V., et al., *Improving the Fast Charging Capability of Lithium-Ion Battery Graphite Anodes by Implementing an Alternative Binder System.* Journal of the Electrochemical Society, 2023. **170**(12): p. 120514.

205. Scott, S., et al., *Improving the Conductivity of Graphite-Based Lithium-Ion Battery Anodes Using Polyaniline-Alginate Blends.* Journal of Physical Chemistry C, 2024. **128**(6): p. 2634-2644.

206. Yan, X., et al., *Fast-charging graphite anode for lithium-ion batteries: Fundamentals, strategies, and outlooks.* Applied Physics Letters, 2024. **124**(4): p. 040501.

207. Zhao, W.B., et al., *Progress, challenge and perspective of graphite-based anode materials for lithium batteries: A review.* Journal of Energy Storage, 2024. **81**: p. 110409.

208. Zhu, H.K., et al., *High-performance graphite||$Li_4Ti_5O_{12}$ dual-ion full batteries enabled by in-situ formation of LiF-rich solid electrolyte interphase on $Li_4Ti_5O_{12}$ anode.* Journal of Power Sources, 2024. **592**: p. 233953.

209. Aspinall, J., et al., *Effect of Microstructure on the Cycling Behavior of Li-In Alloy Anodes for Solid-State Batteries.* Acs

Energy Letters, 2024. **9**(2): p. 578-585.

210. Domi, Y., et al., *Anode Properties of Sb-Based Alloy Electrodes for K-Ion Batteries in an Ionic-Liquid Electrolyte.* Acs Applied Energy Materials, 2023. **6**(22): p. 11583-11591.
211. Hawari, N.H., et al., *Unveiling the effect of alloy-type coating for lithium metal plating and stripping on anode-free lithium metal batteries.* Journal of Alloys and Compounds, 2024. **975**: p. 172988.
212. Liu, Y., et al., *Highly reversible lithium metal batteries enabled by spontaneous alloying anode.* Journal of Physics and Chemistry of Solids, 2024. **187**: p. 111871.
213. Meng, A.C., et al., *Discharge performance of Al-0.1Sn-0.1In-0.05Ga alloy for Al-air battery anodes.* Journal of Energy Storage, 2024. **81**: p. 110414.
214. Salehabadi, M., J.C. Bennett, and M.N. Obrovac, *Morphology Control of Ball-Milled Si-Ti Alloy Anode Materials for Li-Ion Batteries.* Journal of the Electrochemical Society, 2023. **170**(12): p. 120531.
215. Wang, R., et al., *The interface engineering and structure design of an alloying-type metal foil anode for lithium ion batteries: a review.* Materials Horizons, 2024. **11**(4): p. 903-922.

216. Chan, C.K., et al., *High-performance lithium battery anodes using silicon nanowires.* Nature Nanotechnology, 2008. **3**(1): p. 31-35.

217. Zhang, W.J., *A review of the electrochemical performance of alloy anodes for lithium-ion batteries.* Journal of Power Sources, 2011. **196**(1): p. 13-24.

218. Winter, M. and J.O. Besenhard, *Electrochemical lithiation of tin and tin-based intermetallics and composites.* Electrochimica Acta, 1999. **45**(1-2): p. 31-50.

219. Bier, D., et al., *Long Cycle-Life Ca Batteries with Poly(anthraquinonylsulfide) Cathodes and Ca-Sn Alloy Anodes.* Chemsuschem, 2023. **16**(21): p. e202300932.

220. Daali, A., et al., *In situ microscopy and spectroscopy characterization of microsized Sn anode for sodium-ion batteries.* Nano Energy, 2023. **115**: p. 108753.

221. Lin, X.P., et al., *Sb nanoparticles encapsulated in N-doped carbon nanotubes as freestanding anodes for high-performance lithium and potassium ion batteries.* Rare Metals, 2023. **42**(2): p. 449-458.

222. Mu, Y., et al., *Fabrications of Sb@rGO@NSC composite materials as anodes with high performance for lithium ion batteries.* Electrochimica Acta, 2023. **437**: p. 141532.

223. Qi, J.Q., et al., *First-principles investigation of Boron-doped graphene/MoS_2 heterostructure as a potential anode material for Mg-ion battery.* Colloids and Surfaces a-Physicochemical and Engineering Aspects, 2024. **683**: p. 132998.

224. Wang, B., et al., *Green utilization of silicon slime: recovery of Si and synergetic preparation of porous silicon as lithium-ion battery anode materials.* Ionics, 2023. **29**(12): p. 5099-5110.

225. Kasavajjula, U., C.S. Wang, and A.J. Appleby, *Nano- and bulk-silicon-based insertion anodes for lithium-ion secondary cells.* Journal of Power Sources, 2007. **163**(2): p. 1003-1039.

226. Obrovac, M.N. and L. Christensen, *Structural changes in silicon anodes during lithium insertion/extraction.* Electrochemical and Solid State Letters, 2004. **7**(5): p. A93-A96.

227. Miyazaki, R., et al., *An amorphous Si film anode for all-solid-state lithium batteries.* Journal of Power Sources, 2014. **272**: p. 541-545.

228. Miyazaki, R., et al., *Anode properties of silicon-rich amorphous silicon suboxide films in all-solid-state lithium batteries.* Journal of Power Sources, 2016. **329**: p. 41-49.

229. Hang, B.T., et al., *Lithium silicon sulfide as an anode material in all-solid-state lithium batteries.* Journal of Power Sources,

2010. **195**(10): p. 3323-3327.

230. Cervera, R.B., et al., *High performance silicon-based anodes in solid-state lithium batteries.* Energy & Environmental Science, 2014. **7**(2): p. 662-666.

231. Trevey, J.E., et al., *Improved Performance of All-Solid-State Lithium-Ion Batteries Using Nanosilicon Active Material with Multiwalled-Carbon-Nanotubes as a Conductive Additive.* Electrochemical and Solid State Letters, 2010. **13**(11): p. A154-A157.

232. Trevey, J., et al., *Glass-ceramic Li_2S-P_2S_5 electrolytes prepared by a single step ball billing process and their application for all-solid-state lithium-ion batteries.* Electrochemistry Communications, 2009. **11**(9): p. 1830-1833.

233. Kim, K.B., et al., *Nanostructured Si/C Fibers as a Highly Reversible Anode Material for All-Solid-State Lithium-Ion Batteries.* Journal of the Electrochemical Society, 2018. **165**(9): p. A1903-A1908.

234. Dunlap, N.A., et al., *Simple and inexpensive coal-tar-pitch derived Si-C anode composite for all-solid-state Li-ion batteries.* Solid State Ionics, 2018. **324**: p. 207-217.

235. Jin, Y.M., et al., *Enhanced lithium storage performance of Si/C composite nanofiber membrane with carbon coating as*

binder-free and self-supporting anode for lithium-ion battery. Materials Research Bulletin, 2023. **167**: p. 112429.

236. Mery, A., et al., *Toward the Improvement of Silicon-Based Composite Electrodes via an In-Situ Si@C-Graphene Composite Synthesis for Li-Ion Battery Applications.* Materials, 2023. **16**(6): p. 2451.

237. Zand, A.L., et al., *Comprehensive Study of Lithium Diffusion in Si/C-Layer and Si/C_3N_4 Composites in a Faceted Crystalline Silicon Anode for Fast-Charging Lithium-Ion Batteries.* Acs Omega, 2023. **8**(47): p. 44698-44707.

238. Derrien, G., et al., *Nanostructured Sn-C composite as an advanced anode material in high-performance lithium-ion batteries.* Advanced Materials, 2007. **19**(17): p. 2336-2340.

239. Whiteley, J.M., et al., *High-Capacity and Highly Reversible Silicon-Tin Hybrid Anode for Solid-State Lithium-Ion Batteries.* Journal of the Electrochemical Society, 2016. **163**(2): p. A251-A254.

240. Whiteley, J.M., et al., *Tin Networked Electrode Providing Enhanced Volumetric Capacity and Pressureless Operation for All-Solid-State Li-Ion Batteries.* Journal of the Electrochemical Society, 2015. **162**(4): p. A711-A715.

241. Nam, D.H., et al., *Tunable Sn structures in porosity-controlled*

carbon nanofibers for all-solid-state lithium-ion battery anodes. Journal of Materials Chemistry A, 2015. **3**(20): p. 11021-11030.

242. Hayashi, A., et al., *All-solid-state lithium secondary batteries with SnS-P_2S_5 negative electrodes and Li_2S-P_2S_5 solid electrolytes.* Journal of Power Sources, 2005. **146**(1-2): p. 496-500.

243. Aso, K., A. Hayashi, and M. Tatsumisago, *Synthesis of Needle like and Platelike SnS Active Materials in High-Boiling Solvents and Their Application to All-Solid-State Lithium Secondary Batteries.* Crystal Growth & Design, 2011. **11**(9): p. 3900-3904.

244. Chen, L.P., et al., *A Review on Engineering Transition Metal Compound Catalysts to Accelerate the Redox Kinetics of Sulfur Cathodes for Lithium-Sulfur Batteries.* Nano-Micro Letters, 2024. **16**(1): p. 97.

245. Kursun, B., et al., *The effect of outer container geometry on the thermal management of lithium-ion batteries with a combination of phase change material and metal foam.* Journal of Energy Storage, 2024. **80**: p. 110227.

246. Li, Q.H., et al., *Novel design of high elastic solid polymer electrolyte for stable lithium metal batteries.* Journal of

Colloid and Interface Science, 2024. **659**: p. 533-541.

247. Mao, H.Y., et al., *Sulfur-rich MoS_3 cathode for high-performance room-temperature liquid and solid-state lithium metal batteries.* Solid State Ionics, 2024. **406**: p. 116459.

248. Tan, S., et al., *Review on Low-Temperature Electrolytes for Lithium-Ion and Lithium Metal Batteries.* Electrochemical Energy Reviews, 2024. **6**(1): p. 35.

249. Wang, Z., et al., *High-performance localized high-concentration electrolytes by diluent design for long-cycling lithium metal batteries.* Chinese Chemical Letters, 2024. **35**(4): p. 108570.

250. Zhang, Z. and W.Q. Han, *From Liquid to Solid-State Lithium Metal Batteries: Fundamental Issues and Recent Developments.* Nano-Micro Letters, 2024. **16**(1): p. 24.

251. Wenzel, S., et al., *Interphase formation on lithium solid electrolytes-An in situ approach to study interfacial reactions by photoelectron spectroscopy.* Solid State Ionics, 2015. **278**: p. 98-105.

252. Wenzel, S., et al., *Interphase formation and degradation of charge transfer kinetics between a lithium metal anode and highly crystalline $Li_7P_3S_{11}$ solid electrolyte.* Solid State Ionics, 2016. **286**: p. 24-33.

253. Wenzel, S., et al., *Interfacial reactivity and interphase growth of argyrodite solid electrolytes at lithium metal electrodes.* Solid State Ionics, 2018. **318**: p. 102-112.

254. Wenzel, S., et al., *Direct Observation of the Interfacial Instability of the Fast Ionic Conductor $Li_{10}GeP_2S_{12}$ at the Lithium Metal Anode.* Chemistry of Materials, 2016. **28**(7): p. 2400-2407.

255. Nolan, A.M., et al., *Computation-Accelerated Design of Materials and Interfaces for All-Solid-State Lithium-Ion Batteries.* Joule, 2018. **2**(10): p. 2016-2046.

256. Zhu, Y.Z., X.F. He, and Y.F. Mo, *Origin of Outstanding Stability in the Lithium Solid Electrolyte Materials: Insights from Thermodynamic Analyses Based on First-Principles Calculations.* Acs Applied Materials & Interfaces, 2015. **7**(42): p. 23685-23693.

257. Ong, S.P., et al., *Phase stability, electrochemical stability and ionic conductivity of the $Li_{10+/-1}MP_2X_{12}$ (M = Ge, Si, Sn, Al or P, and X = O, S or Se) family of superionic conductors.* Energy & Environmental Science, 2013. **6**(1): p. 148-156.

258. Zhu, Y.Z., X.F. He, and Y.F. Mo, *First principles study on electrochemical and chemical stability of solid electrolyte-electrode interfaces in all-solid-state Li-ion batteries.* Journal

of Materials Chemistry A, 2016. **4**(9): p. 3253-3266.

259. Han, F.D., et al., *Electrochemical Stability of $Li_{10}GeP_2S_{12}$ and $Li_7La_3Zr_2O_{12}$ Solid Electrolytes.* Advanced Energy Materials, 2016. **6**(8): p. 1501590.

260. Wu, F.X. and G. Yushin, *Conversion cathodes for rechargeable lithium and lithium-ion batteries.* Energy & Environmental Science, 2017. **10**(2): p. 435-459.

261. Zhang, Q., et al., *Molybdenum trisulfide based anionic redox driven chemistry enabling high-performance all-solid-state lithium metal batteries.* Energy Storage Materials, 2019. **23**: p. 168-180.

262. Ye, H.L., et al., *Amorphous MoS_3 Infiltrated with Carbon Nanotubes as an Advanced Anode Material of Sodium-Ion Batteries with Large Gravimetric, Areal, and Volumetric Capacities.* Advanced Energy Materials, 2017. **7**(5): p. 160102.

263. Wan, H.L., et al., *Understanding Lil-LiBr Catalyst Activity for Solid State Li_2S/S Reactions in an All-Solid-State Lithium Battery.* Nano Letters, 2021. **21**(19): p. 8488-8494.

264. Zhao, W.J., et al., *Heat Generation in NMC622 Coin Cells during Electrochemical Cycling: Separation of Reversible and Irreversible Heat Effects.* Batteries-Basel, 2020. **6**(4): p. 55.

265. Horner, J.S., et al., *Electrochemical Modeling of GITT*

Measurements for Improved Solid-State Diffusion Coefficient Evaluation. Acs Applied Energy Materials, 2021. **4**(10): p. 11460-11469.

266. Kosova, N.V. and D.Z. Tsydypylov, *Effect of Mechanical Activation and Carbon Coating on Electrochemistry of $TiNb_2O_7$ Anodes for Lithium-Ion Batteries.* Batteries-Basel, 2022. **8**(6): p. 52.
267. Jiang, M., et al., *Ultrasmall Li_2S-Carbon Nanotube Nanocomposites for High-Rate All-Solid-State Lithium-Sulfur Batteries.* Acs Applied Materials & Interfaces, 2021. **13**(16): p. 18666-18672.
268. Shen, Z., et al., *Least Squares Galvanostatic Intermittent Titration Technique (LS-GITT) for Accurate Solid Phase Diffusivity Measurement.* Journal of the Electrochemical Society, 2013. **160**(10): p. A1842-A1846.
269. Wang, X., et al., *Unique Reversible Conversion-Type Mechanism Enhanced Cathode Performance in Amorphous Molybdenum Polysulfide.* ACS Appl Mater Interfaces, 2017. **9**(44): p. 38606-38611.
270. Huang, J., *Diffusion impedance of electroactive materials, electrolytic solutions and porous electrodes: Warburg impedance and beyond.* Electrochimica Acta, 2018. **281**: p.

170-188.

271. Chen, X.F., et al., *Separator engineering toward suppressed shuttle effect and homogenized lithium deposition in lithium-sulfur batteries.* Journal of Alloys and Compounds, 2024. **978**: p. 173482.

272. Li, J.Y., et al., *Engineering Strategies for Suppressing the Shuttle Effect in Lithium-Sulfur Batteries.* Nano-Micro Letters, 2024. **16**(1): p. 12.

273. Wang, X.F., et al., *Fast redox conversion and low shuttle effect enabled by functionalized zeolite for high-performance lithium-sulfur batteries.* Chemical Engineering Journal, 2023. **478**: p. 147315.

274. Zhang, Z.J., et al., *Chemical and physical synergism between PAF-54 and SFPEEKK for effective shuttle effect inhibition of lithium-sulfur battery.* Materials Today Energy, 2023. **38**: p. 101455.

275. Zhang, Q., et al., *Rational design of multi-channel continuous electronic/ionic conductive networks for room temperature vanadium tetrasulfide-based all-solid-state lithium-sulfur batteries.* Nano Energy, 2019. **57**: p. 771-782.

276. Mabayoje, O., et al., *Sulfur-Rich MoS_6 as an Electrocatalyst for the Hydrogen Evolution Reaction.* Acs Applied Energy

Materials, 2018. **1**(9): p. 4453-4458.

277. Tran, P.D., et al., *Coordination polymer structure and revisited hydrogen evolution catalytic mechanism for amorphous molybdenum sulfide.* Nat Mater, 2016. **15**(6): p. 640-646.

278. Shi, J., et al., *Co_3S_4@$Li_7P_3S_{11}$Hexagonal Platelets as Cathodes with Superior Interfacial Contact for All-Solid-State Lithium Batteries.* ACS Appl Mater Interfaces, 2020. **12**(12): p. 14079-14086.

279. Li, W.B., et al., *Controlled construction of 3D self-assembled VS_4 nanoarchitectures as high-performance anodes for sodium-ion batteries.* Electrochimica Acta, 2018. **274**: p. 334-342.